Titre: Title:	Hydrogen Production from Microwave Heating-Assisted Thermal Pyrolysis of Methane
Auteur: Author:	Abdelrahman Hussain
Date:	2025
Type:	Mémoire ou thèse / Dissertation or Thesis
Référence: Citation:	Hussain, A. (2025). Hydrogen Production from Microwave Heating-Assisted Thermal Pyrolysis of Methane [Ph.D. thesis, Polytechnique Montréal]. PolyPublie. https://publications.polymtl.ca/68721/

POLYTECHNIQUE MONTRÉAL

affiliée à l'Université de Montréal

Hydrogen production from microwave heating-assisted thermal pyrolysis of methane

ABDELRAHMAN HUSSAIN

Département de génie chimique

Thèse présentée en vue de l'obtention du diplôme de *Philosophiæ Doctor*

Génie chimique

Août 2025

POLYTECHNIQUE MONTRÉAL

affiliée à l'Université de Montréal

Cette thèse intitulée :

Hydrogen production from microwave heating-assisted thermal pyrolysis of methane

présentée par **Abdelrahman HUSSAIN**

en vue de l'obtention du diplôme de *Philosophiæ Doctor*

a été dûment acceptée par le jury d'examen constitué de :

Louis FRADETTE, président
Gregory PATIENCE, membre et directeur de recherche
Jamal CHAOUKI, membre et codirecteur de recherche
Oumarou SAVADOGO, membre
Nimir O. ELBASHIR, membre externe

DEDICATION

To my first teachers, my beloved parents, Izzeldin & Safwa

To my sister and brothers

To my family and loved ones

ACKNOWLEDGEMENTS

First and foremost, I am deeply grateful to Professor Jamal Chaouki for his invaluable mentorship, guidance, and unwavering support throughout my Ph.D. journey. His wisdom, encouragement, and belief in me have been instrumental in shaping my research and professional growth. I am profoundly appreciative of his patience, insightful discussions, and the endless opportunities he provided for me.

I would also like to express my sincere gratitude to Dr. Mohamad Latifi and Dr. Jaber Shabanian for their continuous support, invaluable advice, and technical guidance. Their expertise and constructive feedback have greatly enriched my research and contributed to the successful completion of this work. Additionally, I extend my heartfelt thanks to Dr. Rouzbeh Jaffari and Dr. Sharif Farag for their insightful discussions, encouragement, and generous support throughout this journey. Their technical expertise and willingness to share their knowledge have been invaluable in overcoming challenges and refining my research.

I am also deeply thankful to my thesis committee members for their time, effort, and valuable feedback throughout this process. Their insightful comments and guidance have played a crucial role in strengthening my research and ensuring the quality of this dissertation.

A heartfelt thank you to my friends and colleagues at the Process Engineering Advanced Research Lab (PEARL) for their friendship, knowledge-sharing, and support. The stimulating discussions, collaborative spirit, and countless moments of encouragement have made this journey both productive and enjoyable.

I would also like to extend my sincere appreciation to the team of technicians at Polytechnique Montréal for their invaluable technical assistance. Their expertise and dedication played a crucial role in the smooth execution of my experiments and the development of my research.

Lastly, I am deeply thankful to my family and loved ones for their unconditional support, patience, and encouragement. Their belief in me has been a constant source of motivation throughout this journey.

RÉSUMÉ

L'hydrogène (H_2) est reconnu comme un vecteur énergétique essentiel dans la transition vers une économie à faible émission de carbone. Il possède une densité énergétique élevée et ne produit que de la vapeur d'eau lors de sa combustion. Le H_2 joue un rôle clé dans la décarbonation des secteurs difficiles à électrifier tels que le transport lourd, les procédés industriels et la production chimique. Avec l'essor des systèmes énergétiques durables à l'échelle mondiale, les technologies de production d' H_2 doivent évoluer afin de minimiser leur impact environnemental tout en répondant à une demande croissante.

Les méthodes conventionnelles de production d' H_2, notamment le reformage à la vapeur du méthane (SMR), sont associées à d'importantes émissions de dioxyde de carbone (CO_2). Leur forte dépendance aux combustibles fossiles compromet leur compatibilité avec des systèmes énergétiques neutres en carbone. Parmi les alternatives émergentes, la pyrolyse thermique du méthane (CH_4) offre une voie de production d'H_2 sans émission de CO_2, en générant de l'hydrogène et du carbone solide sans oxydant ni gaz à effet de serre au niveau du réacteur. Toutefois, le déploiement industriel de cette technologie est freiné par des défis liés à l'apport de chaleur, à l'encrassement des réacteurs et à la gestion du sous-produit solide. Ces limitations peuvent être surmontées grâce à des configurations de réacteurs innovantes et à des stratégies de chauffage alternatives.

Cette étude explore une méthode innovante et durable de production continue d'H_2 par pyrolyse thermique de CH_4 dans un réacteur à lit fluidisé assisté par chauffage micro-ondes (MW-FBR). L'objectif est de remédier aux inconvénients environnementaux des méthodes conventionnelles, notamment leur dépendance aux énergies fossiles et leurs émissions de CO_2. L'énergie micro-ondes, lorsqu'elle est produite à partir de sources renouvelables, permet d'éliminer les émissions directes de carbone liées au chauffage. Le procédé utilise des particules diélectriques inertes dans le lit fluidisé, évitant ainsi la désactivation catalytique fréquente dans les voies catalytiques. Le lit fluidisé offre également une flexibilité opérationnelle pour la gestion du carbone pyrolytique, lorsque les conditions de réaction favorisent son dépôt sélectif et sa rétention sur la surface des particules.

Des expériences ont été menées dans un réacteur MW-FBR à l'échelle du laboratoire pour évaluer ses performances en fonction de divers paramètres tels que la température de réaction, la

concentration d'entrée de CH_4 et le temps de séjour moyen. Les indicateurs de performance notamment la conversion de CH_4, la sélectivité en H_2 et l'efficacité de capture du carbone solide ont été analysés. Les résultats ont démontré une opération stable avec des conversions de CH_4 atteignant 70 % et une sélectivité en H_2 approchant 95 %. L'efficacité de capture du carbone sur les particules fluidisées a été évaluée à l'aide d'expériences en régime transitoire (TOS), en comparant les taux de dépôt de carbone sur les particules au taux total de formation de carbone. Ces mesures ont montré qu'environ 90 % du carbone pyrolytique formé était capturé de manière sélective sur les particules. Par ailleurs, des expériences prolongées de 18 heures ont confirmé la stabilité du MW-FBR en termes de conversion de CH_4 et de sélectivité en H_2.

Pour évaluer l'impact des effets thermiques spécifiques aux micro-ondes, une comparaison directe a été effectuée entre le MW-FBR et un réacteur à lit fluidisé chauffé de manière conventionnelle (CH-FBR), dans des conditions identiques. Le chauffage par micro-ondes a montré de meilleures performances en termes de conversion de CH_4, d'efficacité de capture du carbone et de qualité du carbone pyrolytique. Ces améliorations ont été attribuées aux effets thermiques spécifiques aux micro-ondes, notamment les gradients de température gaz–solide et la formation de points chauds localisés aux contacts entre particules.

Les énergies d'activation apparentes ont été déterminées expérimentalement et se sont révélées plus faibles dans le MW-FBR (288 kJ/mol) que dans le CH-FBR (310 kJ/mol). Des simulations numériques ont été réalisées pour estimer la température des points chauds induits par les contacts entre particules. Ces simulations ont montré que la température des points chauds était environ 180 °C supérieure à celle des particules en vrac dans les conditions expérimentales étudiées. En conséquence, la température effective du lit dans le MW-FBR est supérieure d'environ 5 % à la température mesurée.

ABSTRACT

Hydrogen (H_2) is recognized as a critical energy carrier in the transition to a low-carbon economy. It has high energy content and clean combustion byproduct. H_2 is important in decarbonizing hard-to-electrify sectors such as heavy-duty transportation, industrial processing, and chemical manufacturing. With the global momentum shifting toward sustainable energy systems, H_2 production technologies must evolve to ensure minimal environmental impact while meeting rising demand.

Conventional H_2 production methods, particularly steam methane reforming (SMR), are associated with significant carbon dioxide (CO_2) emissions. Conventional methods heavy reliance on fossil fuels undermines their suitability for climate-neutral energy systems. Among emerging alternatives, methane (CH_4) thermal pyrolysis presents a CO_2-free pathway, producing H_2 and solid carbon without involving oxidants or generating greenhouse gases at the reactor level. However, scaling this route faces challenges related to heat delivery, reactor clogging, and effective carbon byproduct handling. Theses barriers can be addressed through innovative reactor configurations and heating strategies.

This study investigates a novel and sustainable method for continuous H_2 production through CH_4 thermal pyrolysis using microwave (MW) heating-assisted fluidized bed reactor (MW-FBR). The motivation for this work lies in addressing the environmental drawbacks of conventional H_2 production methods, particularly their reliance on fossil fuels and substantial CO_2 emissions. MW energy, when generated from renewable sources, offers an environmentally friendly alternative by eliminating direct carbon emissions associated with heat generation. The process employs inert dielectric particles within the fluidized bed, effectively avoiding catalyst deactivation problems typically encountered in catalytic pathways. The fluidized bed provides operational flexibility for managing the pyrolytic carbon product when the reaction conditions promote its selective deposition and retention on the surface of the fluidized particles.

Experimental work was conducted in a lab-scale MW-FBR to evaluate its operational performance under various parameters such as reaction temperature, CH_4 inlet concentration, and mean residence time. Key performance metrics, including CH_4 conversion, H_2 selectivity, and solid carbon capture efficiency were assessed. Results demonstrated stable operation with a high CH_4

conversions of up to 70% and H_2 selectivity approaching 95%. The carbon capture efficiency on fluidized particles was assessed by conducting time-on-stream (TOS) experiments, during which we monitored and compared the rate of carbon deposition on the particle surfaces to the total rate of carbon formation from CH_4 pyrolysis. These measurements revealed that up to 90% of the pyrolytic carbon formed was selectively deposited onto the fluidized particles. Furthermore, extended TOS experiments performed over a duration of 18 hours confirmed the stable performance of the MW-FBR in terms CH_4 conversion and H_2 selectivity.

To highlight the impact of MW specific heating effects, we conducted a direct comparison between the MW-FBR and a conventionally heated fluidized bed reactor (CH-FBR) under identical conditions. MW heating demonstrated superior performance in CH_4 conversion, carbon capture efficiency, and pyrolytic carbon quality. These improvements were attributed to MW-specific thermal effects, including gas–solid temperature gradients and the formation of localized hotspots at particle contacts.

The apparent activation energies were determined experimentally and found to be lower in the MW-FBR (288 kJ/mol) compared to the CH-FBR (310 kJ/mol). Numerical simulation was carried out to estimate the hotspots temperature which are caused by particle-particles contact. The hotspot temperatures were approximately 180 °C higher than the bulk particle temperatures under the studied experimental conditions. Due to the presence of hotspots in MW-FBR, the effective bed temperature in MW-FBR is higher by 5% compared to the measured temperature.

TABLE OF CONTENTS

DEDICATION iii

ACKNOWLEDGEMENTS iv

RÉSUMÉ v

ABSTRACT vii

TABLE OF CONTENTS ix

LIST OF TABLES xii

LIST OF FIGURES xiii

LISTE OF SYMBOLS AND ABBREVIATIONS xvii

LIST OF APPENDICES xviii

CHAPTER 1 INTRODUCTION 1

1.1 The role of hydrogen in energy transition 1

1.1.1 Market demand for hydrogen and applications 1

1.1.2 Hydrogen production methods 3

1.2 Electrification of the chemical industry 4

CHAPTER 2 LITERATURE REVIEW 6

2.1 Introduction to MW 6

2.1.1 Dipolar polarization 7

2.1.2 Ionic conduction 7

2.1.3 Interfacial polarization 8

2.1.4 Joule heating 8

2.2 Factors affecting MW heating 9

2.2.1 Frequency of MW radiation 9

2.2.2 Power of MW radiation 9

2.2.3 Material properties 10
2.2.4 Complex permittivity 10
2.2.5 Penetration depth 11
2.3 MW heating Vs conventional heating 12
2.4 MW heating in chemical processing 14
2.4.1 Temperature gradient within the solid phase 16
2.4.2 Temperature gradient between gas/solid phases 19
2.5 Methane Thermal Pyrolysis 21
2.5.1 Gaseous product distribution 22
2.5.2 Reaction mechanism 23
2.5.3 Gas phase pyrolytic carbon formation mechanism 24
2.5.4 Pyrolytic carbon forms 26
2.5.5 Reactors configuration for CH_4 pyrolysis 27
CHAPTER 3 RESEARCH OBJECTIVES 30
3.1 Problem identification 30
3.2 Objectives 31
CHAPTER 4 ARTICLE 1 - HYDROGEN PRODUCTION FROM METHANE THERMAL PYROLYSIS IN A MICROWAVE HEATING-ASSISTED FLUIDIZED BED REACTOR 33
4.1 Abstract 33
4.2 Introduction 34
4.3 Experimental 37
4.3.1 Material 37
4.3.2 Experimental setups 38
4.3.3 Carbon characterization 42
4.3.4 Estimation of CH_4 conversion, H_2 selectivity, and mean residence time 43

4.4 Results and discussions 44
4.4.1 Temperature distribution 44
4.4.2 CH_4 conversion and H_2 selectivity 46
4.4.3 Pyrolytic carbon capture efficiency 49
4.4.4 Carbon characterization 54
4.4.5 Process transient behavior 62
4.5 Conclusions 64
CHAPTER 5 ARTICLE 2 – KINETIC INVESTIGATION OF MICROWAVE HEATING-ASSISTED METHANE PYROLYSIS 69
5.1 Abstract 69
5.2 Introduction 70
5.3 Methods 72
5.3.1 Experimental 72
5.3.2 Model formulation 73
5.4 Results 77
5.4.1 Experimental results 77
5.4.2 Kinetic parameters estimation 80
5.4.3 Hotspots origin and thermal contribution in MW-FBR 84
5.4.4 CH_4 pyrolysis in MW-FBR 90
5.5 Conclusion 90
CHAPTER 6 GENERAL DISCUSSION 96
CHAPTER 7 CONCLUSION AND RECOMMENDATIONS 106
REFERENCES 109
APPENDICES 125

LIST OF TABLES

Table 2.1 Comparison of different material properties under MW irradiation [16] 11

Table 2.2 Comparing the aspects of MW heating and conventional heating mechanisms [28] ... 13

Table 2.3 Applications of MW heating-assisted processes in the literature 15

Table 4.1 Properties of SiC particles..... 38

Table 4.2 Experimental conditions for CH4 thermal pyrolysis in MW-FBR and CH-FBR..... 44

Table 4.3 Raman spectra of C-SiC produced at different temperatures from MW-FBR and CH-FBR 60

Table 4.4 Carbon mass balance after 18 hr TOS..... 64

Table 5.1 Experimental conditions for CH4 thermal pyrolysis in MW-FBR and CH-FBR..... 72

Table 5.2 Experimental conditions for CH4 thermal pyrolysis in MW-FBR and CH-FBR..... 81

Table A.1 Summary of carbon deposition experiments..... 127

Table A.2 Elements identification and quantification from the XPS Survey scan 128

Table A.3 Elements identification, quantification and peak fitting parameters from a high-resolution XPS scan 129

Table A.4 Spectrum analysis of EDX data according to Figure A.5 acquisition..... 130

Table A.5 Dielectric properties of solid particles 136

Table B.1 Fitting parameters for axial temperature distribution in CH-FBR in Eq. (5.19) 143

Table B.2 Properties of SiC particles in MW heating numerical simulation..... 146

LIST OF FIGURES

Figure 1.1 H_2 end-use applications in a decarbonized economy [5] 2

Figure 1.2 Production pathways of H_2 4

Figure 2.1 Electromagnetic spectrum overview [14] 6

Figure 2.2 Comparison of MW heating mechanism of Dipolar Rotation and Ionic Conduction [19] 8

Figure 2.3 Different kinds of material interaction under MW irradiation. 10

Figure 2.4 Schematic design of temperature gradient direction under (A) MW heating and (B) conventional heating (CH) 13

Figure 2.5 DRM catalyst stability at 800 ºC for (a) conventional reaction mode (CRM) and (b) MW catalytic reaction mode (MCRM). [41]. 18

Figure 2.6 MW heating-assisted fluidized bed reactor in DRM; a) gas/solid temperature distribution; b) H_2 selectivity; c) CO selectivity. [33] 20

Figure 2.7 Axial gas/solid temperature profile in MW heating-assisted structured reactor during methane non-oxidative conversion (MNOC). [35] 21

Figure 2.8 C1-C3 gas phase reaction mechanism of CH_4 thermal pyrolysis [51,52] 24

Figure 2.9 Mechanistic progression of carbon nucleation and growth in the gas phase [54] 25

Figure 3.1 Schematic of CH4 thermal pyrolysis in MW-FBR 31

Figure 4.1 a) Schematic representation of MW-FBR experimental setup and b) reactor unit of CH-FBR showing temperature measurement points at different bed heights (z). 41

Figure 4.2 Temperature distribution of solid, gas, and reactor wall in MW-FBR, and corresponding MW power consumption at various input MW power levels. 45

Figure 4.3 Axial temperature distribution in the CH-FBR, illustrating both the dense bed and freeboard regions, at a set dense bed temperature of 1050 °C. 46

Figure 4.4 CH4 conversion in MW-FBR and CH-FBR at different a) temperature, b) τ, and c) $yCH4o$. 47

Figure 4.5 Variation of H2 selectivity in MW-FBR and CH-FBR with a) temperature and b) CH4 conversion. 49

Figure 4.6 Variation of rd/rp in MW-FBR and CH-FBR with a) rp , b) temperature, c) ug, and d) $yCH4o$. 52

Figure 4.7 Visual observations of carbon accumulation on the reactor wall in the MW-FBR unit after TOS of a) 0 hours, b) 10 hours, and c) 23 hours. 53

Figure 4.8 SEM images at different magnifications of a) SiC, b) MW-1050, and c) CH-1050. .. 55

Figure 4.9 Raman spectra of a) SiC, b) C-SiC produced in MW-FBR and CH-FBR at different temperatures; and peak deconvolutions of c) MW-1050, d) MW-950, e) CH-1050, and f) CH-950. 57

Figure 4.10 Deconvolution of C1s of XPS spectra for a) SiC and b) MW-1050. 61

Figure 4.11 Transient performance in MW-FBR for 18 hr TOS showing a) variation of solid temperature and CH4 conversion with TOS, b) variation of carbon content with TOS, c) variation of H2 selectivity with TOS, and d) variation of H2 selectivity with the transient. 63

Figure 5.1 Temperature distribution around single particle in MW-FBR. 74

Figure 5.2 Experimental (symbols) and estimated (lines) gas temperature and bulk temperature versus measured solid temperature in MW-FBR 78

Figure 5.3 variation of CH4 conversion in MW-FBR with a) solid temperature and b) mean residence time; and in CH-FBR with c) temperature and d) mean residence time 79

Figure 5.4 Variation of the rate of CH_4 pyrolysis in relation to the change in inlet CH_4 concentration 80

Figure 5.5 Parity plots for experimental and predicted CH_4 conversion in a) MW-FBR, and b) CH-FBR 82

Figure 5.6 Effect of temperature on estimated activation energy in MW-FBR with reference CH-FBR 83

Figure 5.7 Effect of particle contact in MW-FBR on a) power dissipation, b) temperature; and c) surface hotspot formation at the contact of 2 mm particles. 87

Figure 5.8 Radial profiles of a) current density distribution for two contacting particles, b) power dissipation density distribution for two contacting particles, c) current density distribution for a single particle, and d) power dissipation density distribution for a single particle. 88

Figure 5.9 Temperature variation from numerical simulation of MW-FBR; a) variation of Ths and $Teff$ at different Ts, b) variation of β at different αhs 90

Figure 5.10 Predicted CH_4 conversion in MW-FBR as a function of temperature at different residence times from 1.0 s to 20 s 90

Figure A.1 Equilibrium diagram for 1 mole of CH4 calculated by Gibbs energy minimization module in FactSage 7.2 at a total pressure of 1 atm and the temperature range of 25–1300 °C showing CH_4, H_2, and solid carbon. 125

Figure A.2 Variation in C_2 hydrocarbons selectivity with temperatures in MW-FBR. 125

Figure A.3 Representative TGA analysis of C-SiC sample. 126

Figure A.4 Representative net carbon gain variation with TOS at different temperatures and 4 cm/s in MW-FBR 126

Figure A.5 Sample retrieved from the gas filter in MW-FBR. 130

Figure A.6 Carbon restored from CH-FBR wall showing a) photo of carbon sheets from the dense bed; and SEM-EDX of b) carbon retrieved from the dense bed facing the wall; c) and d) carbon from dense bed facing the dense bed at different magnifications; e) and f) carbon from the freeboard wall at different magnifications. 133

Figure A.7 TGA of carbon restored from CH-FBR wall. 133

Figure A.8 SEM-EDX performed on a piece of the reactor wall from MW-FBR after 23 hr TOS. The carbon layer deposited on the wall was thin and could not be mechanically collected for analysis. Therefore, the SEM was performed on a piece of the reactor comprising the the inner wall of the reactor. EDX result shows the surface consists of Si at 42 At.%, O at 33 At.%, and C at 25 At.%. The signal from Si and O belongs to quartz observed due to the thin layer of carbon. 134

Figure A.9 Effect of carbon content on electrical conductivity (σ) and loss tangent (tan δ) (at 2.45 GHz and 20 °C). 135

Figure A.10 Effect of carbon content on particles heating rate and maximum temperature for SiC (0.0 wt.%) and C-SiC with carbon content of 0.7 wt.% and 4.0 wt.%..... 136

Figure B.1 Temperature measurement in the dense bed and the freeboard in CH-FBR..... 143

Figure B.2 Temperature measurement in the dense bed and the freeboard in CH-FBR..... 145

Figure B.3 Mesh independence evaluation 148

Figure B.4 Comparison of experimental and simulated temperature profiles for model validation 148

Figure B.5 Bed pressure drop and voidage profiles at different superficial gas velocities..... 150

LISTE OF SYMBOLS AND ABBREVIATIONS

C-SiC	Carbon-coated silicon carbide particles
CH-1050	C-SiC produced in CH-FBR at 1050 ^{o}C
CH-950	C-SiC produced in CH-FBR at 950 ^{o}C
CH-FBR	Conventional heating-assisted fluidized bed reactor
CN	Coordination number
MW	MW
MW-1050	C-SiC produced in MW-FBR at 1050 ^{o}C
MW-950	C-SiC produced in MW-FBR at 950 ^{o}C
MW-FBR	MW heating-assisted fluidized bed reactor
MFC	Mass flow controller
SiC	Silicon carbide
TOS	Time-on-stream (min)

LIST OF APPENDICES

APPENDIX A Supporting information to chapter 4 125

APPENDIX B Supporting information to chapter 5 141

CHAPTER 1 INTRODUCTION

1.1 The role of hydrogen in energy transition

Hydrogen (H_2) has emerged as a crucial element in the global energy transition, offering a versatile and clean energy carrier with the potential to significantly reduce greenhouse gas emissions and mitigate climate change [1]. H_2 plays a vital role in decarbonization efforts by serving as a clean energy carrier that produces zero emissions at the point of use. For sectors that are problematic to electrify such as aviation, heavy industries, and long-haul transportation, H_2 can replace fossil fuels. It can be produced from renewable electricity, making it a key enabler for large-scale, efficient renewable energy integration. By 2050, H_2 and H_2-based fuels are projected to meet a significant share of final energy demand, contributing to the overall reduction of emissions [1,2].

Compared to electricity and fossil fuels, H_2 offers several distinct advantages. First, it enables long-term, carbon-free seasonal energy storage, which is essential for addressing the intermittency challenges associated with renewable energy sources such as solar and wind. In contrast to electricity, whose storage is constrained by battery capacity and grid limitations, H_2 provides a scalable solution for energy buffering over extended periods.

Second, H_2 offers significant flexibility in energy systems. It can be utilized in both centralized and decentralized power generation, serving as a reliable source of backup power and enhancing overall grid stability. This makes H_2 particularly valuable during periods when renewable electricity generation is low or inconsistent.

Third, H_2 is a highly versatile energy carrier. It can be deployed across a wide range of applications, including industrial processes, transportation, and power generation. Its compatibility with hard-to-electrify sectors such as heavy industry and long-haul transportation further underscores its potential to complement and extend the reach of electrification efforts.

1.1.1 Market demand for hydrogen and applications

The market demand for H_2 has evolved over the years, with its applications expanding across various sectors. Historically, H_2 demand was primarily concentrated in traditional industrial

applications. The largest consumers were ammonia production, oil refining, and methanol production. Global H_2 demand reached 97 million tons (Mt) in 2023, growing 2.5% compared to 2022 [1,3]. Demand is projected to increase significantly, potentially reaching 150 Mt by 2030 [3]. Currently, H_2 use remains concentrated in traditional industrial applications, with limited penetration in new sectors.

New sectors for H_2 use may include energy and power, where H_2 fuel cells can provide clean electricity, especially useful in remote or off-grid locations. Figure 1.1 shows H_2 utilization across key economic sectors. Boilers powered by H_2 offer a low-carbon alternative for residential, commercial, and industrial heating, and H_2 can be used for long-duration energy storage and transportation of renewable power. In the transportation sector, H_2 fuel cells are powering buses, trucks, and trains as a zero-emission alternative to diesel engines with some other applications in maritime transport and aviation. Other emerging applications include the production of synthetic fuels by combining H_2 with captured CO_2 neutral alternative fuels [4].

Figure 1.1 H_2 end-use applications in a decarbonized economy [5]

1.1.2 Hydrogen production methods

H_2 can be produced from fossil fuels, water, and biomass using diverse energy sources such as fossil fuels, nuclear energy, and renewable resources. Depending on the source of energy and the process used, H_2 is classified into color-coded categories that reflect its environmental impact and production method. Figure 1.2 illustrates four of the most commonly referenced types; gray, blue, green, and turquoise.

Gray H_2, which dominates global H_2 production (~99%), is produced from fossil fuels such as natural gas and coal using steam methane reforming (SMR), partial oxidation, or gasification. While these methods offer high conversion efficiency and relatively low production costs (as low as \$1–2/kg H_2), they are associated with significant CO_2 emissions, making them environmentally unsustainable [6]. SMR and coal gasification remain the most economically favorable options for large-scale H_2 supply, but their heavy carbon footprint represents a major challenge in the transition to cleaner energy.

Blue H_2 emerges as a transitional solution that builds upon gray H_2 pathways by integrating carbon capture and storage (CCS) technologies to mitigate CO_2 emissions. This method reduces the carbon intensity of H_2 production but, it increases the overall cost by roughly 50%, due to the capital and operational expenses associated with CCS [6,7]. Blue H_2 helps decarbonize the process but does not entirely eliminate emissions, and its scalability is constrained by the availability of CO_2 storage infrastructure.

Green H_2 is a sustainable and CO_2-free option, produced via water electrolysis powered by renewable electricity (solar, wind, hydro). Green H_2 faces economic and technical limitations. The production cost is high, ranging from \$4–15/kg H_2, largely due to the capital-intensive nature of electrolyzer technology [7]. Electrolysis systems face technical challenges such as limited efficiency, high capital costs, and durability concerns, which currently hinder their widespread deployment. Additionally, the reliance on high-purity freshwater makes them potentially unsuitable in regions facing water scarcity. As renewable energy and electrolyzer technologies improve, green H_2 may become more cost-competitive, nonetheless, currently it accounts for a small share (~0.1%) of global H_2 production [8,9].

Turquoise H_2, an emerging and less commercially mature pathway, is produced via methane pyrolysis. This process decomposes methane thermally to yield H_2 and solid carbon instead of CO_2,

potentially enabling a low-emission alternative without requiring CCS. Turquoise H_2 shows promise in terms of reducing greenhouse gas emissions but, it is still at a developmental stage. Challenges include reactor design for continuous carbon removal, maintaining high conversion efficiencies, and managing the solid carbon by-product [8].

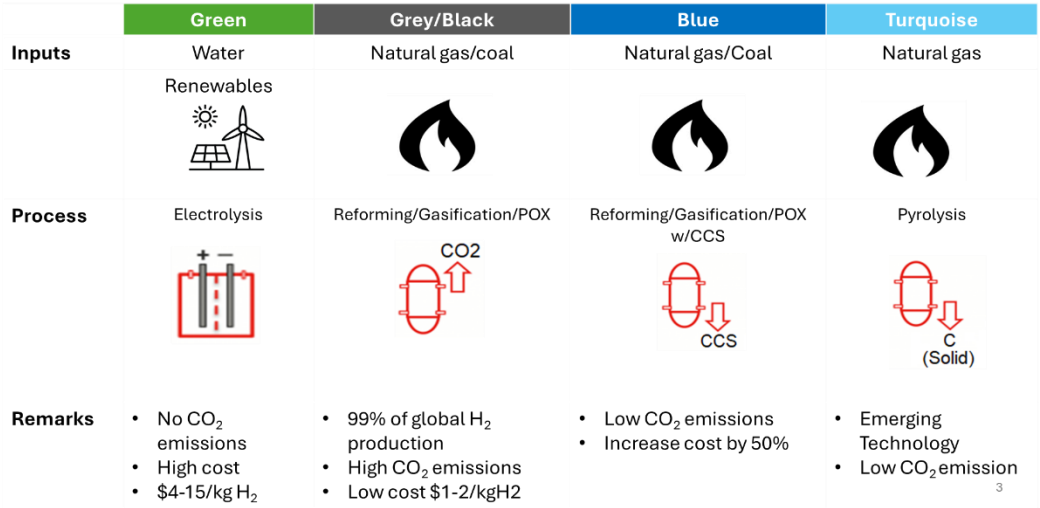

Figure 1.2 Production pathways of H_2

1.2 Electrification of the chemical industry

Electrifying chemical manufacturing is a pathway to decarbonize one of the most energy-intensive industrial sectors. Current efforts focus on replacing fossil fuel-driven processes with electricity-powered alternatives [10]. The chemical industry's reliance on fossil fuels presents challenges that limit decarbonization efforts. The sector contributes 7% of global greenhouse gas emissions at 3.3 gigatons annually [11]. High emissions are driven by energy-intensive processes like steam cracking and methane reforming. Electrifying chemical production is a pivotal strategy for reducing the sector's 7% share of global greenhouse gas emissions. By replacing fossil fuel-driven heat supply with renewable electricity, the industry can achieve high emissions reductions [10,12].

There are different approaches to electrify chemical processes. These approaches vary in complexity, readiness, and suitability depending on the application. One route is indirect electrification where electricity is used to generate an intermediate energy carrier such as H_2 or

synthetic fuels. The energy carrier is then used to supply heat or act as a feedstock. For instance, H_2 produced via electrolysis can be combusted to replace fossil-derived heat in high-temperature operations. This pathway suffers from conversion losses, for example, the overall efficiency from electricity to usable heat through H_2 can drop below 40% [11]. However, H_2 offers valuable flexibility as it can be stored, transported, and used both as a heat source and a chemical feedstock which make it suitable for retrofitting existing infrastructure and supporting intermittent renewable energy sources [11].

Another route involves electrochemical and photochemical approaches which are being developed to drive chemical reactions through electricity or light rather than heat. These systems operate under milder conditions and may enable decentralized or modular production [10]. An example of this route is the electrochemical reduction of CO_2 to produce value-added chemicals such as ethylene or formic acid [12]. This approach has the potential to both reduce emissions and create circular carbon pathways. Electrochemical and photochemical approaches offer the potential for high selectivity and lower operating temperatures, but many remain in early stages of development, with challenges related to scalability, material durability, and integration into existing process infrastructures.

Direct electrification involves using electricity to provide heat or drive chemical reactions without intermediate steps. Technologies such as resistive heating, MW, and induction systems can achieve thermal efficiencies exceeding 80% and reach temperatures above 1000 °C [10]. These methods allow rapid and localized heating which make them suitable for energy-intensive applications like steam cracking and methane reforming. Direct electrification offers the most straightforward route to displace fossil fuel combustion and decarbonize thermal processes in the chemical industry.

CHAPTER 2 LITERATURE REVIEW

2.1 Introduction to MW

Electromagnetic waves cover a vast spectrum of wavelengths, ranging from 10^{-10} cm for gamma rays to 10^{5} cm for radio waves, Figure 2.1. Within this spectrum, microwave (MW) radiation operates at frequencies between 0.3 and 300 GHz. This specific frequency range prevents interference with other applications. A standardized frequency of 2.45 GHz for controlled MW are permitted to use in laboratory scale works [13].

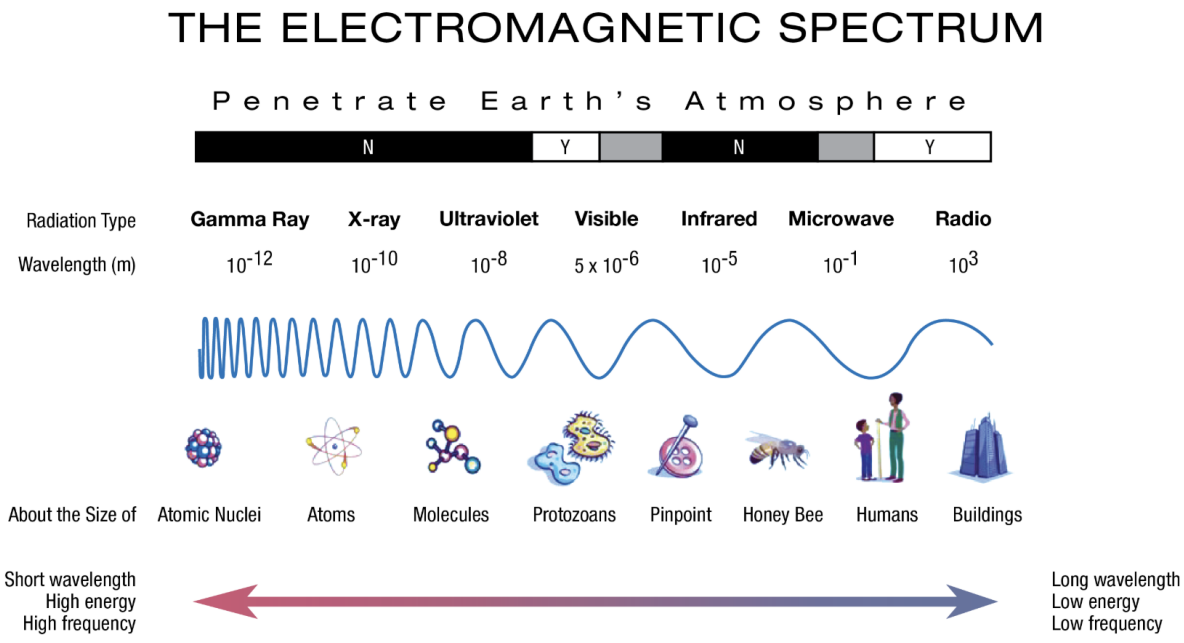

Figure 2.1 Electromagnetic spectrum overview [14]

MW heating is a process in which electromagnetic energy is converted into thermal energy through interactions with the molecular structure of materials. One of the key applications of MW radiation is in heating processes, where electromagnetic waves are converted into thermal energy. This process is governed by the interaction of MW with the molecular structure of the target material.

Specifically, MW heating works by inducing movement and agitation of molecules, particularly dipole molecules, which attempt to realign themselves with the rapidly oscillating electromagnetic field. This form of heating is widely used in industrial processing, food preparation, and scientific research due to its efficiency, selectivity, and ability to provide rapid heating. The mechanism of MW heating is governed by four primary processes namely dipolar polarization, ionic conduction, interfacial polarization, and Joule heating**.** Each mechanism contributes differently depending on the properties of the material being heated [15].

2.1.1 Dipolar polarization

Dipolar polarization, or dipole rotation, is effective for materials containing polar molecules, such as water, ethanol, and liquid ammonia, Figure 2.2. When exposed to an alternating electromagnetic field, dipole molecules attempt to align with the field's direction [16]. Since the MW field oscillates at high frequencies (e.g., 2.45 GHz), the dipole molecules continuously reorient themselves to match the changing field direction. This rapid reorientation causes molecular friction and collisions, generating heat within the material [17].

2.1.2 Ionic conduction

Ionic conduction, or resistive heating, is effective in ionic solutions, electrolytes, and certain conductive materials, Figure 2.2. Free ions in the material oscillates to the applied MW field which leads to collisions with surrounding molecules [3]. These collisions generate heat, effectively converting electromagnetic energy into thermal energy. The heating intensity depends on the ion concentration and mobility where the more mobile the ions, the greater the heating effect [5].

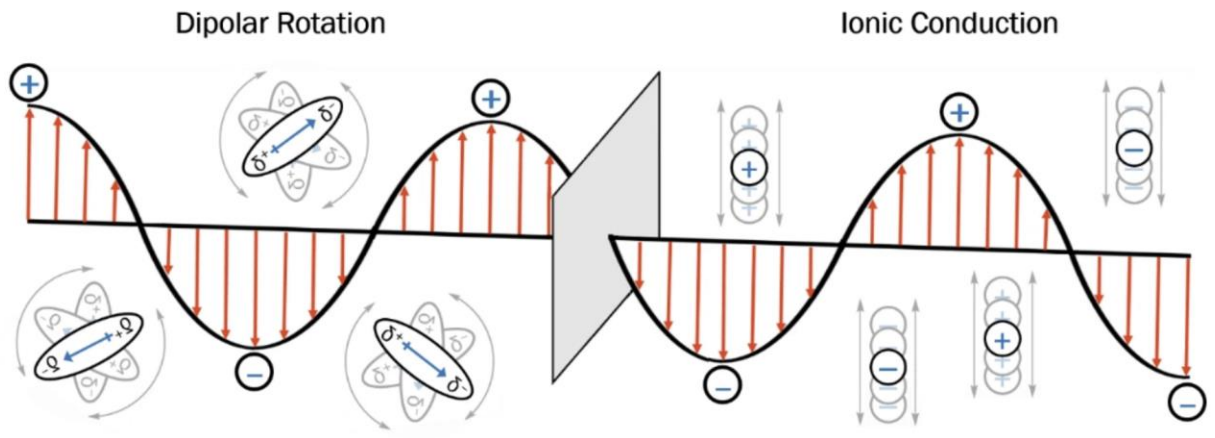

Figure 2.2 Comparison of MW heating mechanism of Dipolar Rotation and Ionic Conduction [19]

2.1.3 Interfacial polarization

Interfacial polarization, also known as the Maxwell-Wagner-Sillars effect, occurs in heterogeneous materials where regions with different electrical conductivities are present (composite and porous materials). When the heterogeneous material is exposed to a MW field, charge carriers (electrons and ions) accumulate at the interfaces of these regions, leading to local electric field distortions [17]. The continuous reorganization of charge carriers results in heat generation [20].

2.1.4 Joule heating

Joule heating, also known as resistive heating or Ohmic heating, occurs in conductive materials where electrical energy is dissipated as heat due to resistance to the flow of the electric current. When a material with electrical conductivity is subjected to an electromagnetic field, free electrons or ions move through it [21]. The resistance of the material opposes this motion, causing energy dissipation in the form of heat [22]. The power dissipated as heat due to Joule's heating follows Joule's law, $P = I^2R$, where I is the current and R is the electrical resistance. Joule heating plays an important role in high-frequency MW-assisted systems, where small resistive losses can result in substantial local heating and, may dominates over dielectric heating. In conductive solids, Joule's heating becomes particularly relevant at inter-particle contact points or in the presence of conductive networks.

2.2 Factors affecting MW heating

MW heating is influenced by several factors that determine how efficiently a material absorbs and dissipates MW energy as heat. The three primary factors that govern MW-material interactions and power dissipation are frequency, MW power, and material properties. These factors are crucial for optimizing MW heating applications in lab scale studies or large-scale applications.

2.2.1 Frequency of MW radiation

MW frequency impacts how materials absorb electromagnetic energy and convert it into heat. In practical applications, specific frequency bands are allocated to avoid interference with communication systems and to ensure efficient energy transfer. 2.45 GHz is the widely used frequency in domestic and industrial MW heating applications, including food processing and laboratory research. 915 MHz is applied for large-scale industrial heating due to its greater penetration depth, making it suitable for bulk materials. 5.8 GHz and higher is used in specialized applications requiring surface heating or precise energy control. MW penetration depth and MW frequencies have a reverse relation; lower frequencies have deeper penetration depth. In this regard, the size of the material would be restricted by the MW frequency.

2.2.2 Power of MW radiation

MW power, typically measured in watts (W), determines the rate at which energy is delivered to a material. Higher power levels increase the heating rate, but excessive power can lead to overheating, non-uniform heating, or thermal runaway effects. However, the relationship between MW power and heating efficiency depends on how well the material absorbs MW energy [23]. Higher power levels increase the heating rate, but if a material has poor MW absorption, energy is wasted. For instance, in ceramic sintering, controlled MW power is necessary to avoid thermal stress and cracking while ensuring uniform heating. Therefore, the MW power should be optimized based on the material properties, specifically for each application [24].

2.2.3 Material properties

Materials interaction with MW is classified into three primary types of interactions [25], as depicted in Figure 2.3.

- Absorbative Materials: This category of materials, such as silicon carbide and carbon, efficiently absorbs MW energy and converts it into heat at different conversion rates.
- Transparent Materials: Substances such as air, quartz, and glass allow MW to pass through with non or minimal absorption, making them nearly transparent to MW radiation. As a result, it is impossible to directly heat this type of material with MW.
- Reflective Materials: Metals reflect MW, preventing penetration and absorption, which can lead to shielding effects (MW oven walls).

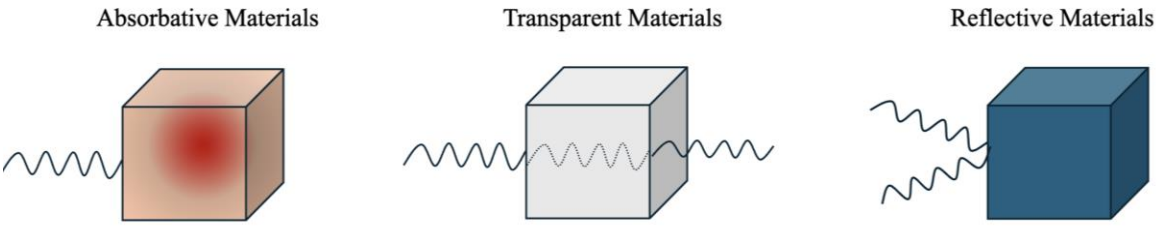

Figure 2.3 Different kinds of material interaction under MW irradiation.

2.2.4 Complex permittivity

The complex permittivity (ε^*) quantifies MW-material interactions. As such, it is possible to compare different materials based on their ability to generate thermal energy from MW irradiation [26]. Complex permittivity encompasses both the dielectric constant (ε'), which determines a material's ability to store electrical energy, and the dielectric loss factor (ε''), which quantifies the efficiency of energy dissipation as heat, Equation 2.1.

$$\varepsilon^* = \varepsilon' - j\varepsilon'' \tag{2.1}$$

A more precise comparison of how different materials interact with MW radiation is possible by comparing the loss tangent ($\tan(\delta)$). The loss tangent is defined as the ratio of the dielectric loss

factor (ε'') to the dielectric constant (ε'), Equation 2.2. This parameter quantifies a material's ability to convert MW energy into thermal energy, making it a crucial factor in assessing MW heating efficiency. The loss tangent is influenced by both temperature and frequency, with an inverse relationship to frequency, meaning that as MW frequency increases, the efficiency of energy conversion generally decreases [27].

$$\tan(\delta) = \frac{\varepsilon''}{\varepsilon'} \tag{2.2}$$

For efficient conversion of MW into thermal energy, the loss tangent (tan(δ)) should be as high as possible, as it directly influences the material's ability to absorb and dissipate MW energy as heat.

2.2.5 Penetration depth

Penetration depth (D_p) quantifies the extent to which MW penetrate a given material. The penetration depth is primarily influenced by the MW wavelength (λ) and the dielectric properties of the target material [27]. Penetration depth is determined using Equation 2.3.

$$D_p = (4\pi f.\sqrt{\frac{[\mu'\mu_0\varepsilon'\varepsilon_0]\left[\sqrt{\left(1+\left(\frac{\varepsilon''_{eff}}{\varepsilon'}\right)^2\right)}-1\right]}{2}})^{-1} \tag{2.3}$$

An increase in ε' and λ of the electromagnetic waves leads to a greater penetration depth. Understanding this relationship is crucial for optimizing MW-assisted processes, particularly in applications requiring uniform heating and energy absorption control. Table 2.1 presents a comparative analysis of some materials, highlighting their ε', ε'', $\tan(\delta)$, and D_p. [15].

Table 2.1 Comparison of different material properties under MW irradiation [16]

Material	$\boldsymbol{\varepsilon'}$	$\boldsymbol{\varepsilon''}$	**tan(δ)**	**Dp (cm)**	**Type of material**
Water (distilled)	78	12	0.153	1.44	Absorbative

Table 2.1 Comparison of different material properties under MW irradiation [16] (cont'd)

Material	ε'	ε''	tan(δ)	Dp (cm)	Type of material
Polyethylene	2.3	0.001	0.0004	2953.5	Transparent
Alumina ceramic	8.9	0.009	0.001	632.6	Transparent
Silicon carbide	30	11	0.366	0.97	Absorbative
Skin – Dry	38.01	10.74	0.282	1.13	Absorbative

2.3 MW heating Vs conventional heating

Conventional heating has superficial modes of heat transfer: convection, conduction, and radiation. Thermal energy is first transferred from an external heat source to the outer surface of the material, then the heat propagates inward through the material via thermal conduction; thus, the temperature gradient is from the surface toward the inside of the material, Figure 2.4B. A limitation of conventional heating is that the bulk material must be heated up, which causes waste of energy and time [15].

In contrast, MW energy enters directly into the material (depending on D_p), generating thermal energy within the core itself, Figure 2.4A. As a result, the temperature gradient is reversed compared to conventional heating, heat transfers from the inside toward the surface. This volumetric heating effect enhances energy efficiency and heating rate, making MW heating a superior alternative in diverse thermal applications [15].

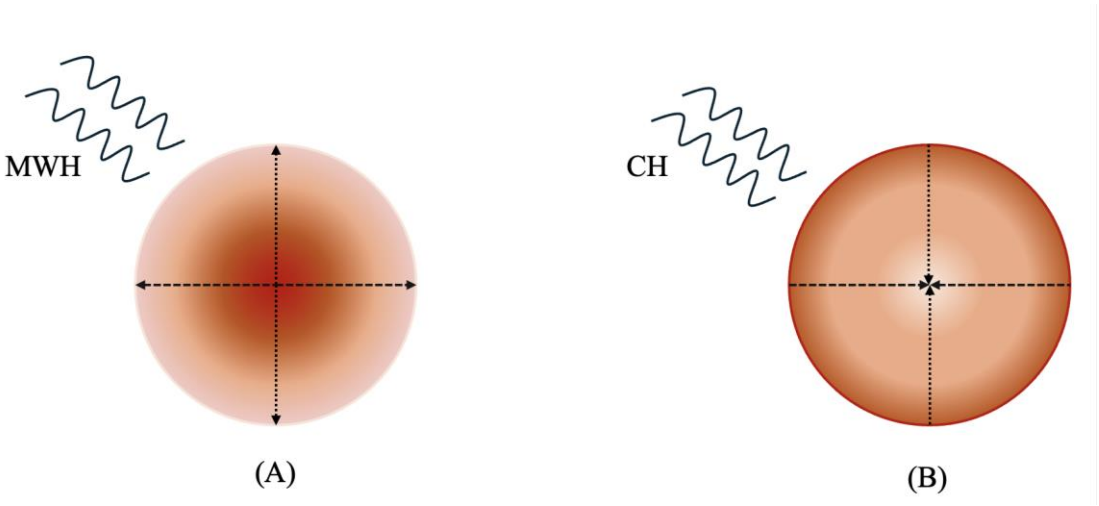

Figure 2.4 Schematic design of temperature gradient direction under (A) MW heating and (B) conventional heating (CH)

Since the interaction between electromagnetic waves and materials is governed by their dielectric properties, MW heating is a selective heating technique. This selectivity allows different materials to heat at varying rates based on their ability to absorb MW energy. One of the key advantages of MW heating is its energy efficiency, as it requires heating only a targeted reaction site, i.e. catalyst particle, instead of the bulk material. This reduction in energy consumption might translate to lower operational costs compared to conventional heating in various applications. Table 2.2 shows aspects of comparison between MW and conventional heating.

Table 2.2 Comparing the aspects of MW heating and conventional heating mechanisms [28]

Aspect	**MW heating**	**Conventional heating**
Heating Mechanism	Volumetric heating (Converting MW to thermal energy)	Surface heating (heat is transferred from the surface to the core)

Table 2.2 Comparing the aspects of MW heating and conventional heating mechanisms [28] (cont'd)

Aspect	MW heating	Conventional heating
Energy Efficiency	Higher (direct energy absorption reduces heat loss)	Lower (heat loss due to conduction and convection)
Material Compatibility	Selective heating (generating hotspots)	No selectivity (uniform heating)
Temperature Gradient	From inside to outside	From inside to outside
Scalability	Challenging (requires optimization for uniform heating at larger scales)	Easier (widely used and well-optimized for scaling)

2.4 MW heating in chemical processing

MW heating has been widely applied in chemical processes due to its unique advantages. In particular, it can create selective and localized heating for enhancing reaction control. Experimental studies have compared MW and conventional heating, highlighting the impact of heating methods on chemical processes. MW heating is especially beneficial in processes where both heterogeneous and homogeneous reactions occur, and selectivity is challenging. Conventional systems have a uniform temperature across the reactor. As a result, both selective and non-selective reactions may proceed simultaneously. In contrast, MW systems have multiple localized temperature zones within the reactor. This makes it possible for a control to enable selective reactions to proceed preferentially while suppressing undesired pathways. Table 2.3 shows relevant experimental findings from literature for applications of MW heating in chemical processes. In multiphase systems, temperature gradients can form within solid phases (with different dielectric properties) or between fluid and solid phases.

Table 2.3 Applications of MW heating-assisted processes in the literature

Process	Catalyst	Temperature, ºC	Reactor configuration/frequency (GHz) / power (W)	MW heating compared to conventional heating	
				MW advantage	Justification
DRM [29]	Pt/Al_2O_3	450-800	Packed bed 2.45/200	• Higher CH_4 and CO_2 conversion • Higher selectivity to syngas	• Hotspots formation
DRM [30]	Char	800	Packed bed/-/-	• Higher CH_4 and CO_2 conversion • Higher catalyst stability	• Hotspots formation • Enhanced coke gasification
DRM [31]	Ni/Al_2O_3	700	Packed bed 2.45/1000	• In-situ catalyst regeneration	• Enhanced coke gasification
Steam dry reforming (SDR) [32]	Char	600-1000	Packed bed/2.45/3000	• Higher CH_4 and CO_2 conversion	• Hotspots formation
DRM [33]	C-SiO_2+ Ni/Al_2O_3	650-900	Fluidized bed/2.45/2500	• Higher CH_4 and CO_2 conversion • Simultaneous enhancement of selectivity and conversion	• Temperature gradient between the solid phase and the gas phase
DRM [34]	Ni/AC	570-800	Packed bed	• Higher conversion • Higher H_2 selectivity • Enhanced energy efficiency	• Temperature gradient between the solid phase and gas phase, lower outlet gas temperature

Table 2.3 Applications of MW heating-assisted processes in literature (cont'd)

Process	Catalyst	Temperature, ºC	Reactor configuration/frequency (GHz) / power (W)	MW heating compared to conventional heating	
				MW advantage	Justification
MDA [35]	Mo/ZSM5@SiC	700	Structured/100 /110	• Control of product selectivity • Less coke formation	• Temperature gradient between the gas phase and the solid phase • The temperature gradient between the active metal and the zeolite support
OCM [36]	Li/MgO	500-800	Packed bed 2.45/2500	• Higher selectivity to C_2 selectivity	• Rapid product quenching, lower gas temperature

2.4.1 Temperature gradient within the solid phase

Under MW irradiation, temperature gradients can develop within the same solid phase due to non-uniform energy absorption, localized electromagnetic field intensification, and induced current concentration at contact points between particles. These effects lead to microscale thermal heterogeneities that play a role in altering reaction environments.

Hotspots refer to microscale regions where the local temperature rises significantly above the surroundings. They can form due to uneven distribution and dissipation of MW energy within the irradiated material. Hotspots may also originate at contact points between touching particles, where the electromagnetic field intensifies, and induced currents concentrate locally. Horikoshi et al. have shown the occurrence of the phenomenon by optical microscope images of hotspot formation between activated carbon particles [37]. Menéndez et al. have also provided photographic evidence of microplasma formation in MW heating of carbon materials [38].

Hotspots accelerate the conversion of reactants due to high local temperatures. In the application of MW DRM, superior CH_4 and CO_2 conversion as compared to conventional heating is observed. Zhang et al. compared the two heating methods for DRM over platinum catalyst supported on Al_2O_3 at 800 ºC [29]. Conversion under MW heating surpassed both conventional heating and the calculated equilibrium conversion at the reaction temperature, which was ascribed to hotspot formation. Similar results are found for DRM over carbonaceous catalyst. Fidalgo et al. postulated the MW heating and creation of micro-hotspots to compensate for the loss of activity in DRM resulting from mixing a more active catalyst (Ni/Al_2O_3) with less active activated carbon as a MW receptor [39].

Strong interactions between MW and coke deposition substantially increase the temperature locally, i.e., catalyst deactivated sites. In DRM, such coke depositions are removed by gasification to CO via the Boudouard reaction ($C + CO_2 \leftrightarrow 2CO, \Delta H_{298\,K} = +172.4\ kJ/mol$) [40]. Local high temperature in the catalyst deactivated sites further accelerates the gasification rate. Therefore, higher catalyst stability in MW-assisted DRM is observed as compared to conventional heating [29–31].

Realizing this advantage, Li et al. synthesized a novel coke-resistant DRM catalyst, Ni-Co/ZrO_2-CaO [41]. At 800 ºC, the conversion of CH_4 and CO_2 was 97.1 % and 99.2 %, respectively, higher than the conversion under conventional heating at 75.7% and 82% for CH_4 and CO_2, respectively. Furthermore, catalyst stability was maintained for 30 h time-on-stream; in contrast, CH_4 conversion dropped from 75.7% to 64.1 % under conventional heating after 10 h time-on-stream, Figure 2.5. Thermogravimetric and Raman characterization of the spent catalyst has shown that less coke remained on the catalyst after the MW tests as compared to conventional heating, despite higher methane conversion for the former. In addition, the coke retrieved from MW tests contained less γ-type coke, which is more difficult to gasify and causes much of the catalyst deactivation. Therefore, MW selective heating profoundly enhanced coke gasification and improved catalyst stability.

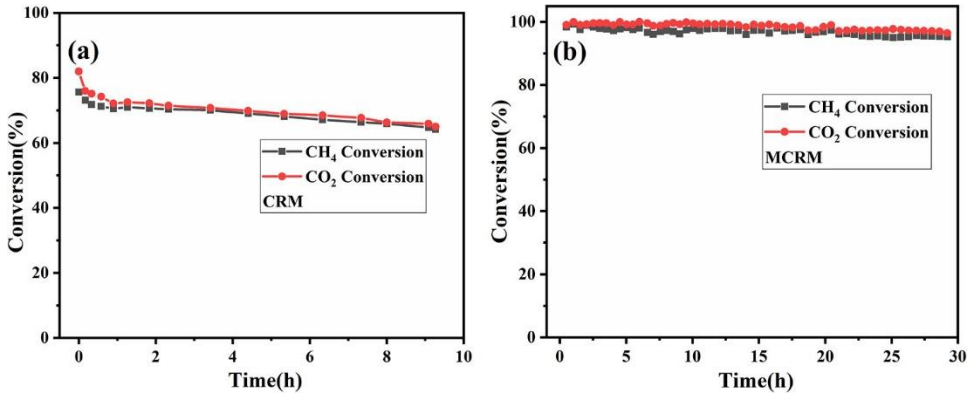

Figure 2.5 DRM catalyst stability at 800 ºC for (a) conventional reaction mode (CRM) and (b) MW catalytic reaction mode (MCRM). [41].

In metal-support catalyst systems, differences in dielectric properties between the active metal phase and the support can lead to localized temperature gradients under MW irradiation. This effect has been studied in methane dehydroaromatization (MDA) reactions. Metal-zeolite catalysts are excellent candidates for methane dehydroaromatization (MDA) to C_2 hydrocarbons and aromatics [42]. Mechanistic studies propose two main steps for MDA: CH_4 activation on the metal site to produce C_2 hydrocarbons, and a subsequent oligomerization to aromatics on the zeolite's Bronsted acid sites [43,44]. Y. Deng et al. directly heated metal-zeolite catalyst, namely H-(Fe)ZSM-5, under MW radiation for direct methane conversion [45]. A high methane conversion at 40 % is attained at a measured bulk temperature of 550 ºC in comparison to 3.5 % methane conversion at 700 ºC under conventional heating. This suggests a temperature gradient of more than 150 ºC between the active metal sites (responsible for CH_4 activation) and zeolite support. As a result, product selectivity shifts toward C_2 hydrocarbons in MW heating while it shifts to aromatics under conventional heating, which further suggests a lower temperature of zeolite support. In addition, a shorter induction period is observed in MW heating compared to conventional heating. Therefore, the induced temperature gradient between catalyst components due to MW selective heating alters catalytic pathways within the same catalyst particle to adjust the productivity of certain products and suppress others.

2.4.2 Temperature gradient between gas/solid phases

In a heterogeneous gas/solid system under MW radiation, the MW energy selectively heats up the dielectric solid while thermal energy is transferred to the transparent-to-MW gas phase conventionally from the solid phase. Reactor configuration with a wide flow passage for the gas phase slows the approach to thermal equilibrium between the two phases. Hence, a steady state temperature profile is established between the solid phase and the gas phase. Such a temperature profile is experimentally confirmed for MW heating-assisted fluidized bed reactors and MW heating-assisted structured reactors. On the other hand, pulsing techniques in packed beds also create a temperature gradient between the solid phase and the gas phase [46–49].

Hamzehlouia et. al. studied the thermal distribution of gas/solid phases in a MW heating-assisted fluidized bed reactor [33]. A combination of thermometry and radiometry in-situ temperature measurement showed a 300 ^{o}C temperature gradient between solid and gas, Figure 2.6. This temperature distribution accounted for substantial improvements in DRM over a mixture of dielectric C-coated silica sand and non-dielectric HiFUEL R110 reformer catalyst. Simultaneous enhancement in methane conversion and syngas (H_2 and CO) selectivity was attained by increasing the operating temperature, Figure 2.6. This is the opposite trend for DRM under conventional heating, where the selectivity drops at high methane conversion. The remarkable results of MW heating-assisted DRM are associated with the suppression of unselective secondary gas-phase reactions due to lower gas temperatures.

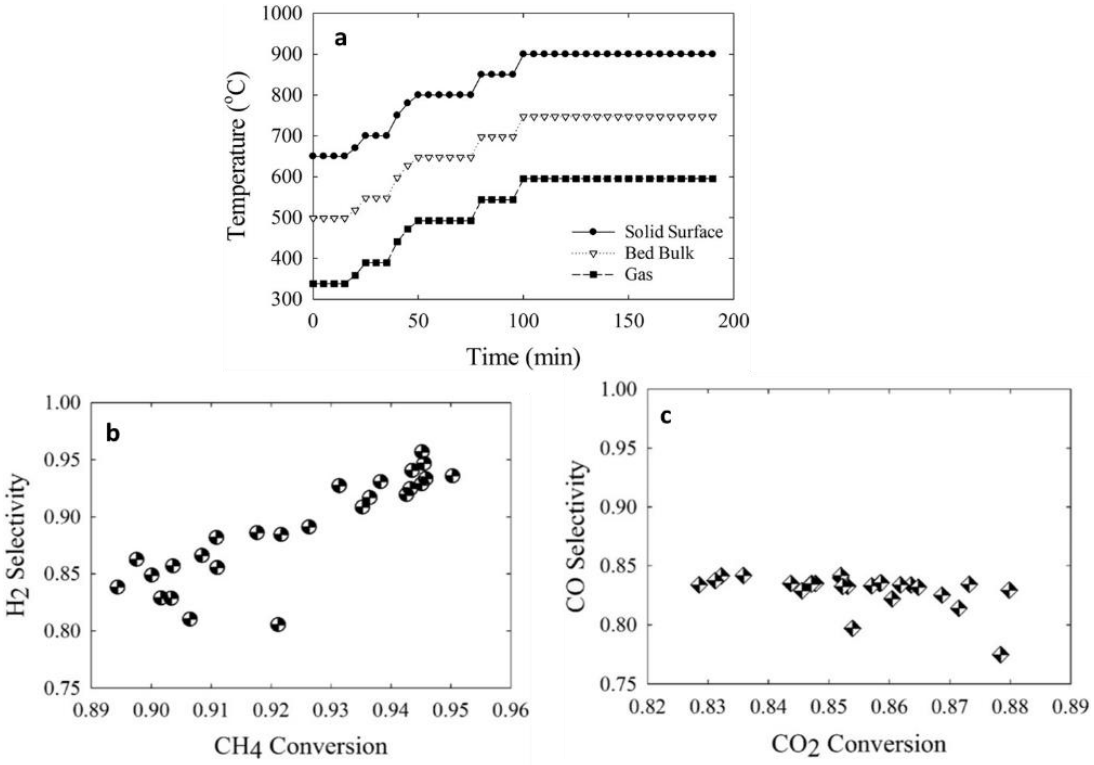

Figure 2.6 MW heating-assisted fluidized bed reactor in DRM; a) gas/solid temperature distribution; b) H_2 selectivity; c) CO selectivity. [33]

A. Ramirez et al. studied gas/solid temperature gradient in a structured (SiC monolith) MW reactor by a combination of an infrared camera, pyrometer, and thermocouple [35]. A temperature gradient between the gas phase and solid monolith in the range of 19-50 ºC is estimated. Gas temperature downstream of the monolith was substantially lower than in the case of conventional heating, Figure 2.7. The SiC monolith was coated with Mo/ZSM-5 catalyst and studied for methane direct conversion at 700 ºC. MW heating altered the product distribution for more C_2-hydrocarbons and benzene as compared to conventional heating. In addition, the formation of polyaromatic hydrocarbons (PAHs) was negligible, which are precursors for coke formation via homogeneous gas-phase reactions. As a result, limited unselective gas phase reactions minimized coke productivity by ~60%.

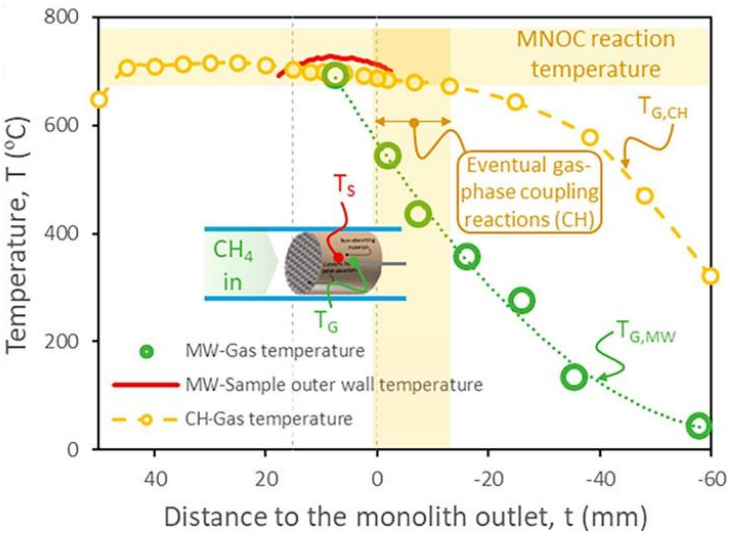

Figure 2.7 Axial gas/solid temperature profile in MW heating-assisted structured reactor during methane non-oxidative conversion (MNOC). [35]

2.5 Methane Thermal Pyrolysis

Methane pyrolysis is the thermal decomposition of CH_4 into H2 and solid carbon according to the reaction:

$$CH_4 \rightarrow C + 2H_2 \ (\Delta H^o = 75.6\, kJ/mol\ CH_4) \tag{4.1}$$

In theoretical energy demand, methane pyrolysis is less energy-intensive per unit hydrogen than SMR and water electrolysis. Methane pyrolysis requires 37.5 kJ per mole of H_2 produced [6], whereas for SMR it is ~63 kJ/mol H2 and 286 kJ. Mol H2 for water electrolysis [6]. In practice, SMR is still more energy efficient and operates at ~75% efficiency (lower heating value basis), and SMR with CCS, the efficiency drops to ~60%. Nevertheless, technoeconomic studies have estimated that the overall energy efficiency of methane pyrolysis is at 58% in converting methane to hydrogen [6]. This puts methane pyrolysis in a similar efficiency class as SMR/CCS [6].

Thermodynamically, high reaction temperatures strongly favor methane conversion because breaking the C–H bonds (~439 kJ/mol) in methane's stable tetrahedral structure requires high energy. CH4 decomposition starts at 550 °C at atmospheric pressure. In practice, significant

decomposition of CH_4 requires a temperature above 1000 °C [50]. Lower pressures are thermodynamically favorable for CH_4 conversion due to the increase in the total number of moles during the reaction (1 mole of CH_4 yielding 2 moles of H_2 and 1 mole of C (s)). According to Le Chatelier's principle, a reduction in pressure shifts the equilibrium toward product formation. In contrast, increasing pressure suppresses the extent of CH_4 decomposition, raising the temperature required to achieve a given conversion level.

2.5.1 Gaseous product distribution

The primary gaseous product of CH_4 pyrolysis is hydrogen (H_2), produced in a 2:1 molar ratio to the CH_4 consumed. Non-catalytic pyrolysis yields a hydrogen-rich gas typically requiring minimal purification, since no CO or CO_2 is generated in this CO_2-free process [50]. In an ideal CH_4 pyrolysis, the only products are H_2 and solid C. Nevertheless, variety of minor hydrocarbon byproducts can appear. These are generally light hydrocarbons (C_2–C_6) formed as intermediate steps in CH_4 decomposition. Key intermediate species identified in high-temperature pyrolysis include ethane (C_2H_6), ethylene (C_2H_4), acetylene (C_2H_2), and even traces of benzene (C_6H_6) or other aromatics. Mechanistically, CH_4 molecules can couple to form C_2 hydrocarbons before completely dehydrogenating. For example, two CH_4 may first form C_2H_6, which then loses H_2 to become C_2H_4, then C_2H_2, and finally breaks into 2C + H_2. At very high temperatures, C_2H_2 is a notable equilibrium byproduct if the gas is rapidly cooled. In one experimental study (1200–1600 °C in an open tubular reactor), the main gaseous byproducts observed (aside from H_2) were C_2H_2, C_2H_4, and trace C_6H_6, which were identified as precursors that eventually lead to carbon deposition. These byproducts tend to be formed in small amounts if the residence time is sufficient for complete cracking; extending residence time helps to consume these intermediates into additional H_2 and carbon. If CH_4 conversion is not complete, some CH_4 will remain in the effluent and would typically be recycled or burned. Importantly, no oxygenated compounds (CO, CO_2) are produced in an oxygen-free pyrolysis environment, which is a key advantage of this route. All carbon ends up in solid form rather than as CO_2 [50].

2.5.2 Reaction mechanism

The gas-phase kinetics of CH_4 thermal pyrolysis proceeds by free-radical mechanism. Literature proposes the chain mechanism $CH_4 \rightarrow C_2 \rightarrow C_6 \rightarrow pyrene$. The series of reactions begin with the cleavage of CH_4 strong carbon-hydrogen bonds. At pyrolysis temperatures below 1400 °C, CH_4 decomposes into a methyl radical (CH_3•) and a hydrogen atom (H•), Figure 2.8. This step is considered as the initial, rate-limiting step of the reaction. This methyl radical is highly reactive and rapidly engages in subsequent radical reactions to form higher hydrocarbons [51]. At pyrolysis temperatures exceeding 1400 °C, an alternative pathway has been proposed, where CH_4 dissociates directly into methylene radicals (CH_2•) and hydrogen molecules (H_2).

Methane reacts with methyl radicals to initially yield C_2H_6. At higher temperatures (above 1000 ^oC), the direct formation of C_2H_4 becomes more favorable due to the instability of C_2H_6 at these conditions. C_2H_4 then undergoes further radical-chain dehydrogenation reactions to yield C_2H_2.

C_6H_6 formation occurs predominantly via the cyclization of C_2H_2 molecules, although C_2H_4 can also contribute to C_6H_6 synthesis. The formation of aromatic species plays a significant role in the carbon deposition process. Once C_6H_6 and other condensed aromatics form, these molecules serve as nuclei for carbon growth leading to solid carbon deposition.

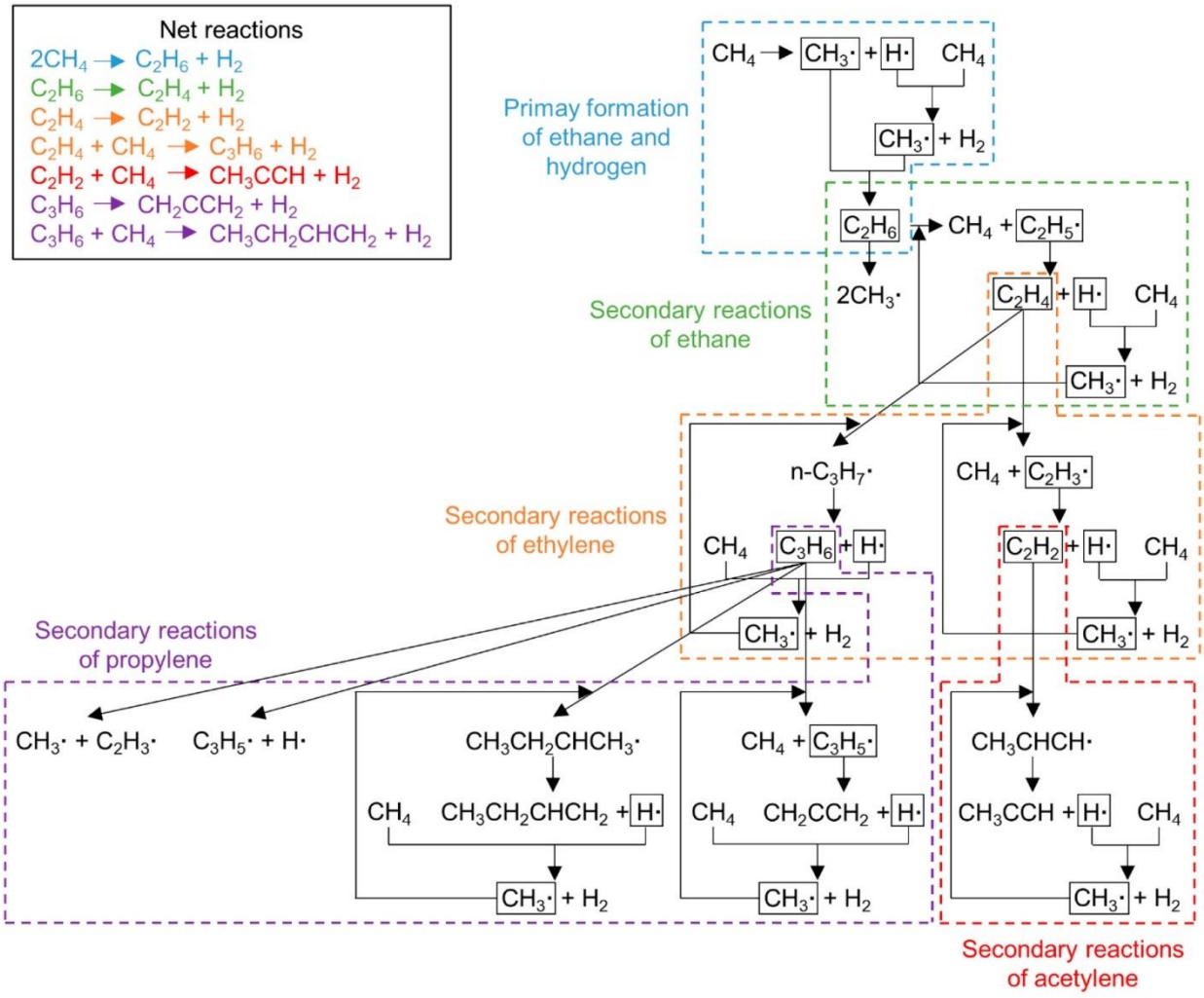

Figure 2.8 C1-C3 gas phase reaction mechanism of CH_4 thermal pyrolysis [51,52]

2.5.3 Gas phase pyrolytic carbon formation mechanism

The formation of pyrolytic carbon proceeds through a sequence initiated by the growth of polycyclic aromatic hydrocarbons (PAHs), Figure 2.9. Small PAHs emerge from molecular-level reactions involving hydrogen abstraction and C_2H_2 addition, a commonly referred to as the H-Abstraction-C_2H_2-Addition (HACA) mechanism. The growth of PAHs via the HACA mechanism continues for 10 to 18 cycles as PAHs become larger, the kinetic rate of growth through the HACA pathway diminishes due to increased thermodynamic energy barriers [53].

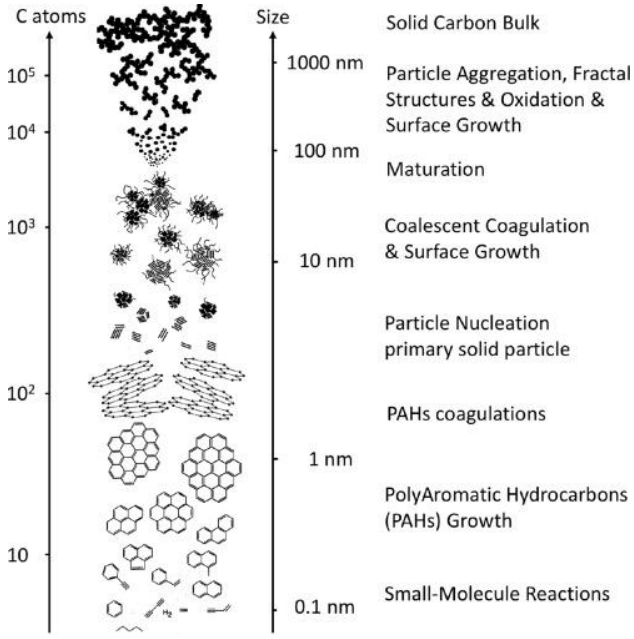

Figure 2.9 Mechanistic progression of carbon nucleation and growth in the gas phase [54]

Further growth transitions from HACA reactions to physical aggregation processes due to collisions between large PAH molecules. These initial collisions, known as nucleation events, involve intermolecular interactions predominantly attributed to van der Waals forces.

Following nucleation, PAH aggregates progressively coalesce into viscous nanodroplets of carbonaceous tar, which subsequently undergo a maturation step involving the internal rearrangement of PAH molecules. During maturation, these PAHs organize into structured graphitic layers, transforming the droplets into solid carbon nanoparticles. In parallel to maturation, surface-driven chemical reactions continue to deposit additional carbon, further enlarging and structurally refining the nanoparticles.

As growth continues, primary nanoparticles aggregate into fractal-like structures through strong interparticle bonds, creating aggregates highly resistant to mechanical stress. The morphology of these aggregates is influenced by the competition between particle maturation rates and surface growth rates, slower surface growth or advanced maturation results in more fragile fractal agglomerates. The size, structure, and mechanical properties of the final pyrolytic carbon agglomerates depend on reaction conditions including temperature, pressure, residence time, and

the concentration of carbon precursors. When solid surface is present in the reaction zone (reactor wall or particles), nucleation and growth can take place on the surface [55].

2.5.4 Pyrolytic carbon forms

Pyrolytic carbon takes several forms depending on the reaction conditions. Broadly, pyrolytic carbon is classified into three categories: amorphous carbon (carbon black) and graphite-like carbon. Pyrolytic carbon from catalytic pyrolysis produces other types of carbon such as carbon nanotubes or nanofibers [6]

Carbon Black consists of nano-sized (10–100 nm) primary particles that form fluffy aggregates. Carbon black is characterized by high surface area and turbostratic structure; randomly oriented graphene-like layers. Its purity is typically high (mostly elemental carbon) but structurally it is mostly amorphous, lacking long-range crystalline order. Carbon black is produced industrially via methane pyrolysis/plasma processes for its useful properties [6]. Nonetheless, carbon black is the lowest-value carbon form (averaging $0.75–$1.00 per kg) but is produced in bulk (>14 million tonnes/year) for uses like tire filler, pigments, and polymer additives [6] . In CH_4 pyrolysis reactors, carbon black tends to form at the highest temperatures (approx. 1400–2000 K) as soot-like particles formed by polycyclic aromatic hydrocarbon (PAH) precursors [6] .

Pyrolytic carbon can also have graphitic structure; the carbon atoms are arranged in stacked planar sheets (graphene layers). High temperatures and prolonged vapor-phase residence allow carbon atoms to arrange into more crystalline structures approaching a graphitic arrangement. For instance, in a solar-thermal pyrolysis experiment with intense heating (~1300 K), CH_4 was converted at ~70% and over half of the carbon deposited in a highly graphitic form on a hot substrate irradiated by the solar beam [56]. This illustrates that extremely rapid and localized heating can produce graphite-like carbon even without metal catalysts.

Graphite has a higher electrical conductivity as compared to carbon black. Therefore, graphitic pyrolytic carbon is suitable for applications like lithium-ion battery anodes [6] . Natural graphite (used for battery anodes) commands prices above $8 per kg, and synthetic battery-grade graphite can reach $20 per kg [6] . Thus, if CH_4 pyrolysis is tuned to produce a graphite-like material (or if the carbon black can be post-treated into crystalline graphite), the co-product’s value and utility

increase substantially. However, achieving truly high-purity graphite often requires either catalytic assistance or post-pyrolysis heat treatment to order the carbon structure .

Thus, non-catalytic CH_4 pyrolysis predominantly produces carbon black unless special measures are taken to influence carbon morphology. By adjusting temperature, residence time, or using novel reactor designs (such as molten metal baths or concentrated solar heating), the process can be steered toward more graphitic carbon forms. The balance between operating conditions and carbon output is a key theme in recent research, as the form of carbon co-product will dictate both the economic payoff and the environmental handling strategy in CH_4 pyrolysis processes [57]. Generally, CH_4 pyrolysis aims to produce a readily removable carbon (avoiding tar or sludge), and many reactor designs (fluidized beds, moving particle reactors, molten media) are tailored to continuously remove carbon to prevent clogging. Solid carbon co-products from CH_4 pyrolysis have been the subject of recent research, including their morphology and potential uses [6,50]

2.5.5 Reactors configuration for CH_4 pyrolysis

2.5.5.1 Hold-wall reactors

In hot-wall designs, CH_4 flows through a heated chamber (often a tubular reactor) where heat is supplied indirectly via external gas burners or electric furnaces. The reactor wall is thus heated externally, and the heat is transferred conventionally to the gas inside the chamber. This design is the simplest one, but it suffers from drawbacks. Significant carbon deposition on the hot walls, eventually causes fouling or channel blockage [6]. The high temperatures at the wall aggravate solid carbon formation and deposition on surfaces. The accumulation of solid carbon hinders heat transfer and creates flow obstructions which reduces overall efficiency. Moreover, frequent shutdowns would be required to remove carbon if no mitigation is in place [6] .

Researchers have explored methods to alleviate wall coking in hot-wall reactors. For example, internally coating the reactor wall with calcium oxide has been shown to make carbon less adherent, thus easing mechanical removal [58]. In one study, a simple scraping plunger was used to periodically dislodge carbon from coated walls, preventing complete blockage [58]. Such measures highlight the inherent challenge: although hot-wall reactors achieve the needed high temperatures,

carbon fouling remains a major operational issue. In practice, hot-wall systems may be limited to batch or short-run operations unless effective carbon removal (mechanical or periodic burn-off) is implemented [6]. Burn-off of carbon deposits is not suitable if free-CO_2 operation is desired.

2.5.5.2 Cold-wall reactors

Cold-wall reactors supply heat within the reactor volume while keeping the reactor walls relatively cool. Cold-wall reactors use internal heating elements (resistively heated filaments, rods, or screens) or contact-free heating (induction and MW) placed inside [59,60]. The walls of the chamber may be cooled externally by a fluid to minimize solid carbon from accumulating on the wall [61]. As a result, the formation and deposition of carbon on the walls is minimized to address a major process challenge. Experimental cold-wall reactor setups have demonstrated significantly longer run times without clogging, since the solid carbon either remains on the heated element (from which it can be periodically removed) or exits with the gas. Moreover, contact-free heating can rapidly achieve the high temperatures needed right in the gas stream [61]. This results in a simpler product removal scenario and can improve the consistency of hydrogen output.

Despite these advantages, designing a reliable cold-wall reactor is complex. The internal heating elements must withstand extreme temperatures and continuous carbon exposure. Materials like tungsten or graphite can serve as heating filaments, but they may suffer from corrosion or gradual carbon buildup that changes their heating characteristics over time. Ensuring the longevity and durability of these heaters or screens is a challenge. Additionally, thermal management and preventing overheating the element is non-trivial [60]. In addition, the removal of carbon from heating elements might be as challenging as removing it from the reactor wall.

2.5.5.3 Moving bed reactors

Moving carbon bed reactors operate by passing CH_4 counter-currently through a descending bed of hot carbon granules. The solids, typically carbon granules, are both a reaction medium and the heat carrier. As CH_4 flows upward, it decomposes on contact with the hot carbon surfaces. The carbon granules grow in size during operation and are continuously withdrawn from the bottom of

the reactor, while fresh or recycled carbon particles are fed at the top. Heat is supplied via induction or resistive heating of the reactor walls.

Moving bed reactors enables continuous removal of the carbon product and avoids carbon accumulation that would otherwise lead to deactivation in fixed-bed systems. The counter-current flow allows for efficient heat recovery, as the hot outgoing carbon bed preheats the incoming CH_4 stream. In addition, the reactor operates at near-atmospheric pressure with relatively low gas velocities, resulting in low pressure drops and stable gas–solid contact.

The most advanced implementation of this design is BASF's electrically heated moving bed reactor, operated at pilot scale in Ludwigshafen, Germany. Following earlier laboratory tests using diluted CH_4 streams at 1000–1400 °C, the pilot plant demonstrates continuous operation with undiluted natural gas at temperatures exceeding 1200 °C. The process has shown sustained hydrogen production with stable solids flow and material integrity at high temperature [62].

2.5.5.4 Fluidized bed reactors

Fluidized bed reactors are commonly applied with the application of catalyst particles [6]. A key benefit in fluidized beds is that pyrolytic carbon deposits on or agglomerate with the fluidized catalyst particles instead of accumulating on reactor walls. Thus, fluidized beds are more robust against wall coking and plugging compared to fixed beds and tubular reactors [6]. Fluidized beds can enable continuous operation: as carbon accumulates on particles, they can collide and undergo attrition, releasing fine carbon particulates that are carried out with the product gas. Carbon fines can then be separated downstream by cyclones or filters and collected continuously. Continuous removal of carbon by entrainment allows the process to avoid shutdowns due to clogging. Another option is to take advantage of the change in particles density due to carbon accumulation. If the density increases, carbon covered particles can be removed at the bottom of the reactor. If the density decreases, carbon covered particles can be carried out of the reactor and collected downstream [62].

CHAPTER 3 RESEARCH OBJECTIVES

3.1 Problem identification

The increasing global demand for sustainable energy carriers highlights the importance of H_2 as a clean fuel to mitigate greenhouse gas emissions. Conventional H_2 production methods, particularly SMR, significantly contribute to CO_2 emissions due to their dependence on fossil fuels. Therefore, developing innovative H_2 production techniques with minimal environmental impact is critical.

Despite its potential as a CO_2-free route for H_2 production, CH_4 pyrolysis presents several challenges that need to be addressed to realize industrial adoption. Catalytic pyrolysis, while effective at lower temperatures, suffers from rapid catalyst deactivation due to coke formation, requiring frequent regeneration or replacement. As a result, the thermal (non-catalytic) pathway offers a more realistic and durable approach for sustained operation. Current CH_4 pyrolysis processes largely remain at relatively low technology readiness levels, primarily constrained by limitations in reactor design, heat supply management, and handling the solid carbon byproduct.

Conventionally heated fixed-bed and tubular reactors, which rely on heat transfer through the reactor walls, face significant challenges in CH_4 pyrolysis applications. Heating through the reactor walls creates steep temperature gradients that promote localized carbon deposition near the heated surfaces. This uneven accumulation accelerates blockage, especially in narrow tubular configurations, leading to increased pressure drop and operational instability. As a result, such systems often require frequent shutdowns for maintenance and carbon removal, limiting their suitability for continuous H_2 production.

Heat supply in CH_4 pyrolysis is another critical area demanding innovation. Conventional heating methods, such as combustion-based heating, generate CO_2 emissions. This undermines the primary objective of CH_4 pyrolysis for clean H_2 production.

These limitations in reactor design, heating strategy, and carbon handling represent major barriers to the industrial implementation of CH_4 thermal pyrolysis. Advancing the process beyond its

current limitations requires innovative solutions that enable continuous operation, clean and efficient heat delivery, and reliable carbon separation and management.

We propose a method that leverages MW heating to address key limitations in CH_4 thermal pyrolysis, as shown in Figure 3.1. When powered by renewable electricity, MW heating enables a CO_2-free route for H_2 production. It delivers rapid and efficient heating when using particles with suitable dielectric properties that reach high temperatures required for CH_4 pyrolysis. The use of chemically inert particles avoids the loss of activity experienced in catalytic pathway. We aim to take advantage of the unique thermal profile of MW heating to obtain local high temperatures within fluidized particles while the bulk gas is at a lower temperature. In addition, the shift in heat delivery from the reactor walls to the particles accelerates CH_4 conversion around the particle and enhance solid carbon capture on the particles without the need for active catalysts.

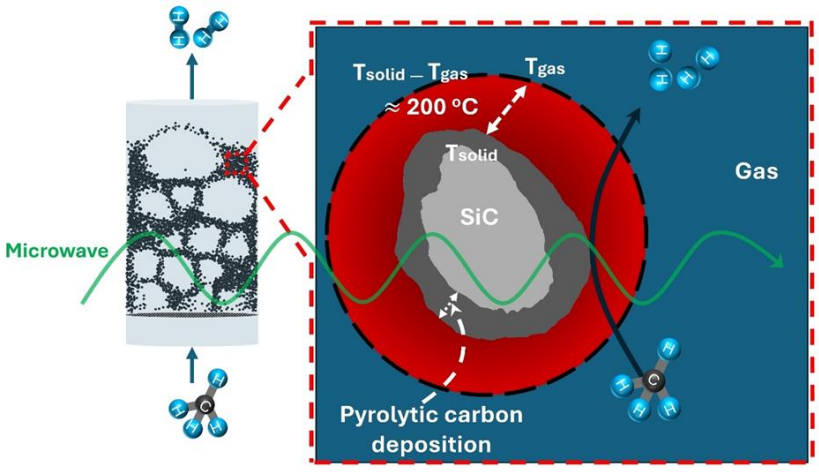

Figure 3.1 Schematic of CH4 thermal pyrolysis in MW-FBR

3.2 Objectives

The main objective of this thesis is to introduce a novel approach for H_2 production from CH_4 thermal pyrolysis in a MW-heating-assisted fluidized bed reactor (MW-FBR) as a potential alternative to conventional methods.

The specific objectives of this thesis are:

1. Demonstrate the feasibility of H_2 production from CH_4 thermal pyrolysis in a MW-FBR by investigating the effects of operating conditions on key performance indicators including CH_4 conversion, H_2 selectivity, and carbon capture efficiency.
2. Investigate the specific thermal effects associated with MW heating by conducting a direct comparison with a conventionally heated fluidized bed reactor.
3. Determine the kinetic parameters for CH_4 thermal pyrolysis

Chapter 4 presents the experimental investigation of CH_4 thermal pyrolysis in MW-FBR. It covers the experimental setup, temperature measurement techniques, and analysis of CH_4 conversion and H_2 selectivity under various operating conditions. The chapter also examines the location and extent of carbon deposition, the efficiency of carbon capture by fluidized particles, and the structural characterization of the pyrolytic carbon. Additionally, the transient behavior of the process during extended operation is evaluated.

Chapter 5 focuses on the determination of kinetic parameters for CH_4 pyrolysis. It also investigates the role of microscale hotspots in the MW-FBR and their influence on CH_4 conversion and estimated activation energy. Throughout Chapters 4 and 5, results from both heating methods are presented and discussed collectively to provide a clearer evaluation of MW-FBR.

CHAPTER 4 ARTICLE 1 - HYDROGEN PRODUCTION FROM METHANE THERMAL PYROLYSIS IN A MICROWAVE HEATING-ASSISTED FLUIDIZED BED REACTOR

Process Engineering Advanced Research Lab, Department of Chemical Engineering, Polytechnique Montreal, C.P. 6079, succ. Centre-Ville, Montreal, QC, Canada H3C 3A7

* Corresponding author: Tel.: +1-514-340-4711 X 4034; Fax: +1-514-340-4159.

E-mail addresses: hussain.abdelrahman@polymtl.ca (A.I. Hussain), jaber.shabanian@polymtl.ca (J. Shabanian), mohammad.latifi@polymtl.ca (M. Latifi), jamal.chaouki@polymtl.ca (J. Chaouki)

(Published in Energy & Fuels on October 25, 2024, DOI : https://doi.org/10.1021/acs.energyfuels.4c03428)

4.1 Abstract

Methane (CH_4) thermal pyrolysis is a promising, carbon dioxide (CO_2)-free method for hydrogen (H_2) production, decomposing CH_4 into H_2 and solid carbon. This highly endothermic and energy-intensive process can sustainably be powered by microwave (MW) heating supported by renewable electricity. In this study, we investigated the efficacy of H_2 production and simultaneous carbon capture through CH_4 thermal pyrolysis in a lab-scale MW heating-assisted fluidized bed reactor (MW-FBR). We identified the effects of the thermal gradient between the solid and gas phases in MW-FBR on the process through direct comparison with a conventional heating-assisted fluidized bed reactor (CH-FBR) under identical operating conditions. Solid dielectric particles in the MW-FBR reach high temperatures, creating favorable conditions for CH_4 thermal decomposition. We examined the influences of temperature (900–1065 °C), mean residence time (0.5–1.5 s), and inlet CH_4 molar fraction (0.2–0.5) on CH_4 conversion and H_2 selectivity. We obtained the highest CH_4 conversion of 23% and H_2 selectivity of up to 98% within the applied experimental conditions. Monitoring pyrolytic carbon byproducts showed that 90% of the produced pyrolytic carbon remained in the bed and captured by fluidized particles. Comparative analysis between MW-FBR and CH-FBR at the same experimental conditions revealed that MW heating substantially outperformed conventional heating due to MW thermal effect, thermal gradient between solid and gas phases, and hotspots formation. On average, CH_4 conversion increased by 150%. Carbon capture efficiency improved by 70%. In addition, MW heating produced more graphitic carbon.

Keywords: Methane thermal pyrolysis, Hydrogen production, MW heating-assisted reactor, Pyrolytic carbon.

4.2 Introduction

The global energy sector is transforming to low and zero-emission fuels. This shift aims at minimizing greenhouse gas (GHG) emissions to combat the pressing challenge of climate change. Hydrogen (H_2) and electricity are key energy carriers for advancing sustainable development. In this regard, H_2 economy has gained momentum and, thus has made a significant evolution in recent years.

Global H_2 demand reached a record high at 95 million tons (Mt) in 2022, about a 3% increase year-on-year [3]. Demand is concentrated in traditional sectors, e.g., industry and refining. Only 0.7% is sourced from low-emission H_2 production sources. Accordingly, over 900 Mt of annual carbon dioxide (CO_2) emissions are linked to H_2 production and application [3,63].

The endeavors to achieve CO_2-free H_2 production encounter significant obstacles. More than 90% of global H_2 is produced from high CO_2-emitting processes, such as steam methane reforming (SMR), coal gasification, and oil and naphtha reforming [3,64]. Half of the global H_2 production capacity comes from SMR at a CO_2 footprint of 9–12 t CO_2/t H_2. The production cost of H_2 via SMR varies depending on natural gas prices but generally averaged around USD 0.94–2.00/kg H_2 in 2021 corresponding to natural gas prices of USD 4.7–14.2/GJ [3,7,65]. CO_2-free H_2 production is possible through water electrolysis coupled with electricity produced from renewable resources. Nonetheless, the cost is high at USD 4–15/kg H_2 [64,65]. Alternatively, methane (CH_4) pyrolysis, as an emerging technology, produces H_2 at a carbon footprint similar to water electrolysis if powered by renewable energy. Techno-economic analyses suggest that CH_4 pyrolysis could become competitive with SMR under specific conditions, such as the implementation of a carbon tax or a solid carbon byproduct market [51,65]. However, these projections are based on reactors that are yet to be built on a commercial scale.

CH_4 pyrolysis produces H_2 and solid carbon according to Eq. (4.1). Various forms of solid carbon byproducts can emerge in CH_4 pyrolysis, spanning from amorphous carbon black and structured graphitic materials to specialized carbon nanotubes and fibers.

$$CH_4 \rightarrow C + 2H_2 \ (\Delta H^o = 75.6\, kJ/mol\ CH_4) \quad (4.1)$$

Thermodynamically, at atmospheric pressure, CH_4 starts to dissociate at 545 ºC [66]. The activation energy of the first-order endothermic gas phase dissociation of CH_4 is estimated at 350–420 kJ/mol [66]. An appreciable CH_4 pyrolysis conversion requires operation at 1000–1200 °C for a few seconds of residence time, while shorter residence times under 1 second require operation at 1600–2200 °C. Metallic and carbonaceous catalysts help lower the CH_4 pyrolysis temperature to 700–800 °C and 850–1000 °C, respectively [67]. Despite continued research in catalysts for CH_4 pyrolysis, rapid catalyst deactivation in a few hours of operation due to excessive coking remains a major barrier to CH_4 catalytic pyrolysis implementation [68–71].

CH_4 thermal pyrolysis avoids the activity loss experienced in the catalytic pathway. Current research in CH_4 thermal pyrolysis prioritizes tackling heat supply challenges and managing carbon buildup while creating effective strategies to remove and utilize the carbon product. Consequently, researchers have proposed various reactor configurations. Tubular reactors represent the simplest configuration for CH_4 thermal pyrolysis. Researchers/engineers adopted small reactor diameters (3–20 mm) to reach a high temperature for high CH_4 conversion [72,73]. Fast carbon deposition at the reactor wall occurs as the rate of carbon formation is higher at the location of the highest temperature. Carbon deposition on the reactor wall impairs the heat transfer to the gas stream and a complete reactor clogging happens within a few hours of operation [73]. Some researchers proposed strategies, e.g., passing a sweeping/carrier gas through a porous reactor tube to manage carbon deposition on the reactor wall [73]. Other researchers proposed coating the tubular reactor wall with calcium hydroxide or sodium chloride with subsequent mechanical carbon removal [58]. Other studies have applied bubble column reactors and fluidized bed reactors [74–78]. In bubble column reactors, CH_4 passes through a molten media (salts or metals), where the formed carbon floats on the surface due to density difference for subsequent collection. CH_4 pyrolysis in bubble columns is performed at 900–1200 ºC with a CH_4 conversion of up to 95% in systems employing catalytic molten metals [79]. Fluidized bed reactors are promising for industrial implementation of CH_4 pyrolysis as they offer flexibility in developing strategies for continuous carbon product removal. The application of fluidized catalyst particles allows the capture of the carbon product. Due to carbon accumulation on the surface of the fluidized particles, the particles grow in size

which affects their fluidization behavior. Larger particles are removed when settling at the bottom of the reactor by gravity [80]. Alternatively, fluidized particles can undergo attrition within the bed releasing accumulated carbon as fine particles that are carried by the gas stream and subsequently elutriated out of the reactor [81]. Catalysts when implemented as the medium to capture the carbon product need to be stored after deactivation since catalyst regeneration would result in undesirable CO_2 emissions [82].

CH_4 thermal pyrolysis requires high energy input, Eq. (4.1). Industrial high-temperature reactors rely on gas burners to heat the reactor tubes. This practice generates CO_2 emissions, which eliminates the advantage of CH_4 pyrolysis as a low-emission H_2 production method. Moreover, gas burners must operate at higher temperatures than the reaction temperature to create a sufficient temperature gradient for heat flow toward reactor sites, resulting in increased heat losses [59]. Therefore, the utilization of a clean source of energy is essential for CO_2-free H_2 production. microwave (MW) heating-assisted reactors coupled with electricity generated from renewable sources offer such an advantage [18]. In MW reactors, MW energy dissipates directly within the volume of dielectric materials inside the reaction zone. This targeted heat generation potentially increases energy efficiency [83]. In addition, MW heating is selective due to the dependency on the material dielectric properties. In MW heating-assisted fluidized bed reactor (MW-FBR), the MW energy selectively heats the dielectric solid particles, while thermal energy is transferred to the gas phase conventionally from the solid phase. As a result, a steady-state temperature profile is established, where the solid phase maintains a significantly higher temperature, several hundred degrees above the bulk gas phase temperature [15].

Previous studies on MW heating-assisted CH_4 pyrolysis utilized activated carbon as the primary material. In the study by Domínguez et al. [84], the authors explored CH_4 pyrolysis in a MW-heated fixed bed reactor, operating at 900 °C, and achieved a CH_4 conversion of 30% with a high H_2 selectivity of 100% during 2 hours of continuous operation. The strong MW absorption properties of activated carbon were key to advancing both CH_4 conversion and H_2 yield in their system. In the study by Dadsetan et al. [80], the authors reported MW heating-assisted CH_4 pyrolysis in a fluidized bed reactor, where the CH_4 conversion dropped from 100% to 5% after a prolonged operation at 800 °C due to catalyst deactivation. However, by increasing the bulk temperature to 1200 °C, they achieved a CH_4 conversion of 90%. While these studies provided valuable insights, the literature still lacks research on temperature distribution in MW heating-

assisted fluidized bed reactors for CH_4 pyrolysis and does not explore the specific role of MW-induced thermal effects on the process.

In this study, we investigated H_2 production from CH_4 thermal pyrolysis in a MW-FBR of chemically inert dielectric particles, addressing the gap in investigating the temperature distribution and MW-induced thermal effects in fluidized bed reactors. The application of chemically inert particles overcomes challenges of rapid catalyst deactivation commonly encountered in CH_4 catalytic pyrolysis. By leveraging the unique temperature profile of MW heating, we achieved localized high temperatures within the fluidized particles, enhancing CH_4 conversion and carbon capture without the need for active catalysts. We employed different techniques to measure these temperature profiles and to evaluate CH_4 conversion and H_2 selectivity under different operating conditions. We also assessed the location and efficiency of carbon deposition on fluidized particles and characterized the pyrolytic carbon deposits. We further analyzed the transient performance of the process. We conducted CH_4 thermal pyrolysis using a conventional heating-assisted fluidized bed reactor (CH-FBR) under identical operating conditions to establish a benchmark, highlighting MW-induced thermal effects (i.e., the thermal gradient between solid and gas phases and the formation of hotspots) and their role in enhancing process performance. We presented results from both heating methods and discussed them collectively.

4.3 Experimental

4.3.1 Material

CH_4 (99.9% purity, Canadian Air liquid) and nitrogen (N_2) (99.99% purity, Canadian Air liquid) were adopted as feed gases in the experiments. We employed silicon carbide (SiC) particles, as effective MW absorbers, from Thermo Fisher Scientific. They were used without further treatment. The main properties of SiC particles are listed in Table 4.1. The adopted SiC particles showed typical Geldard group B behavior at ambient conditions [85,86]. The experimentally measured minimum fluidization velocity (u_{mf}) with N_2 as the fluidizing gas was 4.3 cm/s at ambient conditions.

Table 4.1 Properties of SiC particles

Property	**Value**
Dielectric constant ε' at 20 ºC and 2.45 GHz	8.4
Dielectric loss factor ε'' at 20 ºC and 2.45 GHz	1.1
Electrical conductivity σ, (S/m)	1.8
Density ρ_p, (g/cm^3)	3.2
Heat capacity C_p, (J/kg K)	700
Mean particle size d_p, (μm)	100
Melting point, (ºC)	2700
Minimum fluidization velocity u_{mf}, (cm/s)	4.3
Geldart behavior	Group B

4.3.2 Experimental setups

We adopted laboratory-scale MW-FBR and CH-FBR in our experiments. Both experimental assemblies for MW-FBR and CH-FBR share common process units except the reactor unit. We fed CH_4 and N_2 to the reactor from two pressurized cylinders, passing through solenoid valves controlled by a LabView program, Figure 4.1a. The inlet gas streams were mixed before entering the reactor. We adjusted gas flow rates by calibrated mass flow controllers (MFCs), model Bronkhorst F-201CV. To obtain a gas velocity aligned with the targeted mean residence time specified for each experiment, we set the gas flow rates in relation to the reaction zone's temperature. We employed a Varian CP-4900 Micro Gas Chromatograph (GC) (Agilent Technologies) for analysis of N_2, CH_4, H_2, and C_2 hydrocarbons (i.e. C_2H_6, C_2H_4, and C_2H_2). The GC had a 10-meter MolSieve 5Å column channel (column temperature: 80 ºC, carrier gas: helium,

21 psi) and a 10-meter PPU column (column temperature: 90 ºC, carrier gas: helium, 25 psi). The sampling time was 30 s, the injector temperature was 110 ºC, and the injection time was 30 ms.

3.3.2.1 MW heating setup

We constructed the MW-FBR unit in-house, which consisted of a modified domestic MW oven with a multimode cavity (351 mm × 249 mm × 386 mm), as shown in Figure 4.1a. A 1.1 kW magnetron (model Witol 2M219J), operating at 2.45 GHz, and cooled by a compressed air system generated MW. We modified the cavity to include a fused quartz reactor and temperature measurement devices. We installed hollow stainless-steel cylinders and removable stainless-steel caps at the drilled openings to ensure the cavity remained sealed against MW leakage. We tested the unit for MW leakage with a calibrated radio frequency monitor (Model: Radman 2LT), certified under Safety Code 6, Health Canada. During all tests, MW leakage remained below the accepted safety standard of 5 mW/cm² at 2 inches from the oven.

The quartz tube was 38 cm in length and 2.54 cm in internal diameter. The fused quartz has negligible dielectric properties and thus is not directly heated by MW radiation. The fused quartz is suitable for high-temperature operation up to 1200 ºC. A fritted disc made of quartz with 40 µm porosity was fused inside the tube to act as a gas distributor. Loading/unloading of solid material was achieved by a removable stainless-steel compression cap at the top of the reactor. We varied the solid temperature by changing the input MW power.

A combination of contact (thermocouple) and non-contact (pyrometers) temperature measurement techniques were employed, Figure 4.1a. We measured the solid particles' temperature by pyrometer #1, model optris OPTCT3MH2, which works at the wavelength of 2.3 µm and has a temperature measurement range of 200–1600 ºC, Figure 4.1b. We measured the reactor wall temperature by pyrometer #2, model optris OPTCSLT15SF with a detection window of 8–14 µm and a temperature measurement range of -50 ºC to 1350 ºC. The spot sizes of pyrometers #1 and #2 at the distance from the reactor are 0.9 cm and 1.1 cm, respectively. Quartz has 90% transmittance of infrared radiation in the wavelength range of 0.2–3 µm and is opaque to infrared beyond 5.0 µm. Therefore, pyrometer #1 at 2.3 µm detects the radiation emitted from inside the reactor, i.e. solid particles, whereas pyrometer #2 detects thermal radiation from the reactor wall. We measured the gas temperature with a grounded thermocouple placed at 1.0 cm above the fluidized bed, Figure 4.1a.

3.3.2.2 Conventional (induction) heating setup

An induction heating-assisted fluidized bed reactor was employed for testing CH_4 thermal pyrolysis via conventional heating. However, it is noteworthy that CH-FBR was originally designed to heat internal heating elements (rods) inside a fluid bed where the reactor body was made of a non-conductive material such as quartz or alumina so an inside-out heating mechanism could be obtained [87]. Herein, the reactor body was made of Inconel, which was electrically conductive, so an outside-to-inside heating mechanism was maintained. Electric current passing through induction coils generates a magnetic field around the reactor, inducing currents in the Inconel reactor itself, thereby generating heat through electrical resistance. The heat generated in the reactor wall is transferred conventionally via conduction, convection, and radiation to the bed material (solid and gas). Therefore, the reactor wall is unconventionally heated via the induction heating mechanism, while the bed material, which is targeted for the reaction study, is conventionally heated.

The 10 kW induction heating power supply was manufactured by Norax Canada and consisted of a PID controller, matching box, and water-cooled copper induction coil (10 cm in height). The reactor was made of an Inconel tube (40 cm in height and 2.54 cm in ID) with an installed Inconel gas distributor. The maximum operating temperature of the reactor was 1200 ^{o}C. Loading/unloading of the samples was achieved via removable stainless steel caps. Thermocouples measure the temperature at multiple points inside the fluidized bed, above the fluidized bed, and on the reactor's external wall, Figure 4.1b.

a)

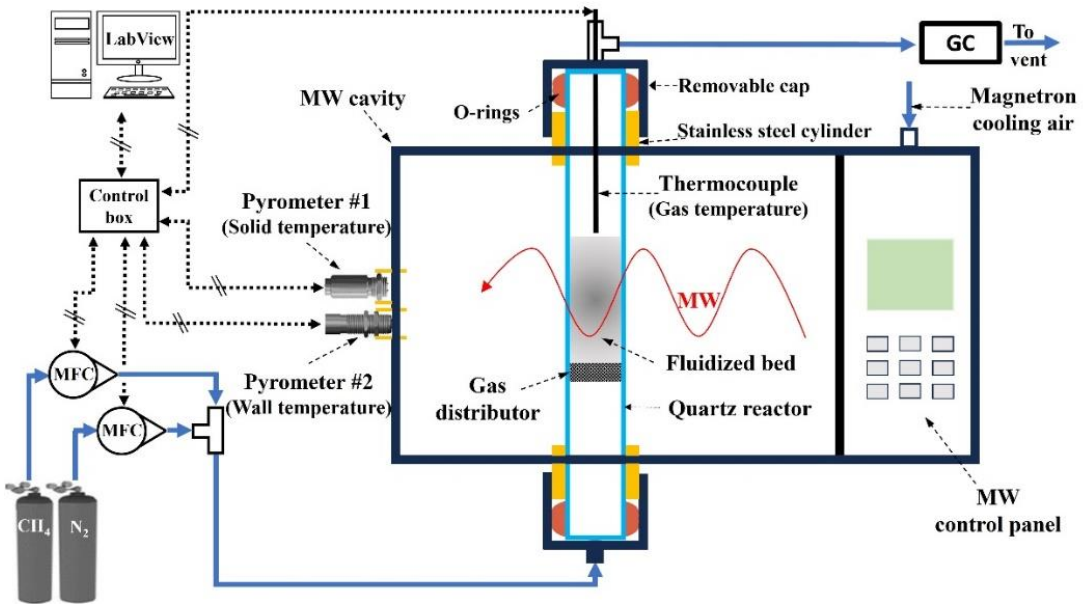

b)

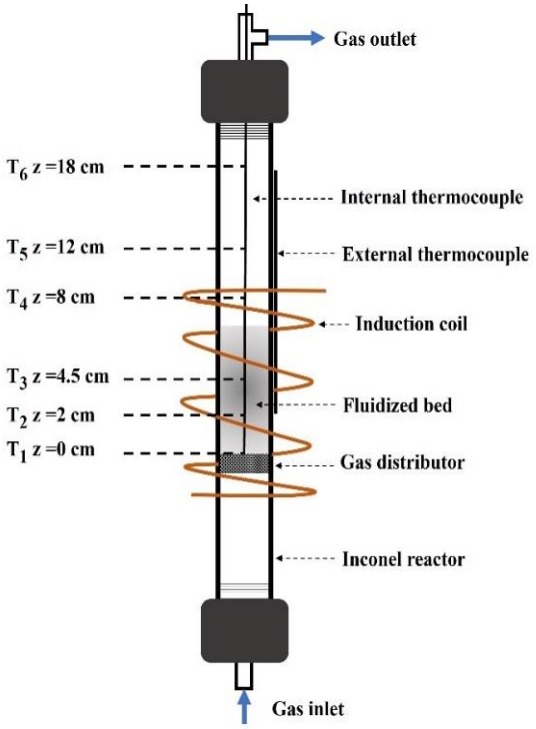

Figure 4.1 a) Schematic representation of MW-FBR experimental setup and b) reactor unit of CH-FBR showing temperature measurement points at different bed heights (z).

4.3.3 Carbon characterization

We measured the amount of carbon deposited on the solid particles with a thermogravimetric analysis (TGA), model TGA 550, TA instruments. We heated the sample to 110 ºC at 10 ºC/min, kept it in isothermal conditions for 15 minutes, and followed up by the same heating rate to 900 ºC and 60 minutes of isothermal hold before cooling the sample to room temperature. The airflow rate was 20 mL/min and the purge gas was N_2 at a flow rate of 20 mL/min.

We performed surface characterization of SiC particles and carbon-coated SiC particles (C-SiC) by scanning electron microscopy (SEM), model JSM-7600 TFE, JEOL, Japan, and energy-dispersive X-ray (EDX) spectroscopy. We operated SEM in lower secondary electron (LEI) mode and at 10.0 kV.

We conducted X-ray photoelectron spectroscopy (XPS) by VG ESCALAB 250Xi apparatus with a monochromatic AlKα X-ray source (1486.68 eV). We collected photoelectron data at a take-off angle of 0°. The detection limit for the analysis was approximately 0.1% atomic. We performed survey scans within a range of binding energies of 0–1350 eV with an energy step size of 1.0 eV and a pass energy of 150 eV. We conducted high-resolution scans with an energy step size of 0.1 eV and a pass energy of 20 eV. We maintained the analysis chamber pressure at 1.0 x 10–8 Torr. We corrected for charge effect by C1s peak at 285.0 eV. We applied a Shirley background to subtract the inelastic background of core-level peaks. We employed Avantage v6.5 from Thermo Fisher Scientific to determine the peak model parameters such as peak positions, widths, and peak intensities. The model peak to describe XPS core-level lines for curve fitting was a product of Gaussian and Lorentzian functions.

We assessed the Raman spectra by employing a WITec Raman spectrometer that featured a motorized stage alpha 300 access microscope. Data acquisition was performed with a 532 nm excitation UHTS300S_GREEN_- NIR laser source, delivering 14 mW of power, along with a 50× Zeiss Epiplan objective. We considered 25 accumulations during the integration period.

We measured the electrical conductivity of particles by the 4-point method [88]. We poured the particles inside an electrically insulated cylinder and pressurized it with air to form a compressed network of the material to minimize the void fraction. We measured dielectric properties, including the dielectric constant (ε') and dielectric loss factor (ε'') by the coaxial prob method employing a vector network analyzer model (Keysight N5247B).

4.3.4 Estimation of CH_4 conversion, H_2 selectivity, and mean residence time

We employed Eq. (4.2) to estimate CH_4 conversion (x_{CH_4}) considering the change in the volumetric flow rate due to the increased number of moles produced per moles of CH_4 converted.

$$x_{CH_4} = \frac{C_{CH_{4,0}} - C_{CH_4}}{C_{CH_{4,0}} + \varepsilon_v \, C_{CH_4}} \tag{4.2}$$

where $C_{CH_{4,0}}$ is the inlet CH_4 concentration, C_{CH_4} is the outlet CH_4 concentration, and ε_v is the volumetric expansion factor. For CH_4 pyrolysis represented by Eq. (4.1), ε_v equals CH_4 inlet molar fraction.

We calculated the H_2 selectivity (S_{H_2}) by Eq. (4.3).

$$S_{H_2} = \frac{n_{H_2}}{2(n_{CH_{4,o}} - n_{CH_4})} \times 100 \tag{4.3}$$

where $n_{i,_o}$ and n_i are the inlet and outlet molar flow rates of gas specie i, respectively. We employed Eq. (4.4) to calculate the individual gases' molar flow rates and Eq. (4.5) to calculate the total molar flow rate (n_T).

$$n_i = y_i \, n_T \tag{4.4}$$

$$n_T = \frac{n_{N_2}}{y_{N_2}} \tag{4.5}$$

where y_i is the molar fraction of gas specie i measured by GC.

Mean residence time (τ) was calculated by Eq. (4.6).

$$\tau = \frac{A_t \, H}{v_0(\frac{T_g}{T_0})} \tag{4.6}$$

where A_t is the reactor cross-sectional area, H is the dense bed height, v_0 is the inlet volumetric flow rate, T_g is the gas temperature, and T_0 is the ambient temperature (298.15 K). The mean residence time was set by changing H and/or v_0. We bounded v_0 by a minimum to obtain bubbling fluidization and a maximum to obtain measurable CH_4 conversion.

The range of the applied experimental conditions is reported in Table 4.2. Multiple measurements were taken for each temperature-flow rate data point, with each data point being measured three times or more, depending on the agreement of the measured molar fractions.

Table 4.2 Experimental conditions for CH4 thermal pyrolysis in MW-FBR and CH-FBR

Property	**Value**
Temperature, (°C)	900–1065
Total pressure, (atm)	1.0
Mean residence time τ, (s)	0.5–2.0
Inlet CH_4 concentration, (mol %)	20–50
Solid particles loading W_S, (g)	30–50
Dense bed height H, (cm)	4.0–8.0
Superficial gas velocity u_g, (cm/s)	4.0–12
u_g/u_{mf} (-)	2.0–6.0

4.4 Results and discussions

4.4.1 Temperature distribution

In MW-FBR, solid particles are heated directly via the MW heating mechanism, while the gas and quartz tube are heated conventionally through contact with the solid particles, as they are transparent to MW. A temperature gradient was identified between the solid, gas, and wall, with solid temperature > gas temperature > wall temperature, as shown in Figure 4.2. On average, the solid temperature was higher than the gas temperature by approximately 200 °C, and the gas temperature exceeded the wall temperature by about 50 °C. The consumed MW power, as

determined from the energy balance calculations (see Section A.4 of the Appendix A), is also presented in Figure 4.2. Approximately 60% of the input MW power is consumed inside the bed.

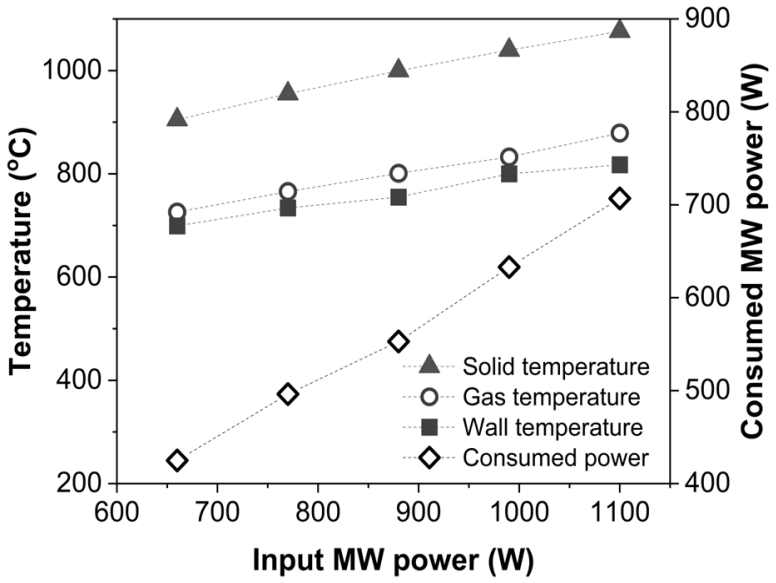

Figure 4.2 Temperature distribution of solid, gas, and reactor wall in MW-FBR, and corresponding MW power consumption at various input MW power levels.

CH-FBR had a different temperature profile compared to MW-FBR. Gas and solid temperatures were similar in the dense bed, and uniform as accepted for conventional heating fluidized beds. The axial temperature distribution inside the reactor chamber and the reactor wall for a set process temperature of 1050 ºC are shown in Figure 4.3. The dense bed temperature was slightly lower at the distributor level (1041 ºC) and reached the set temperature at the measurement point of 2 cm above the distributor and stayed constant for the remaining dense bed height. Above the dense bed (freeboard zone), the temperature decreased gradually due to heat loss to the reactor wall and accordingly to the ambiance. The wall temperature in the bed area was higher than the process temperature. We had a higher wall temperature as the temperature control was from the signal of the thermocouple inside the dense bed (T_2, Figure 4.2b), the wall temperature was higher to achieve the set point temperature.

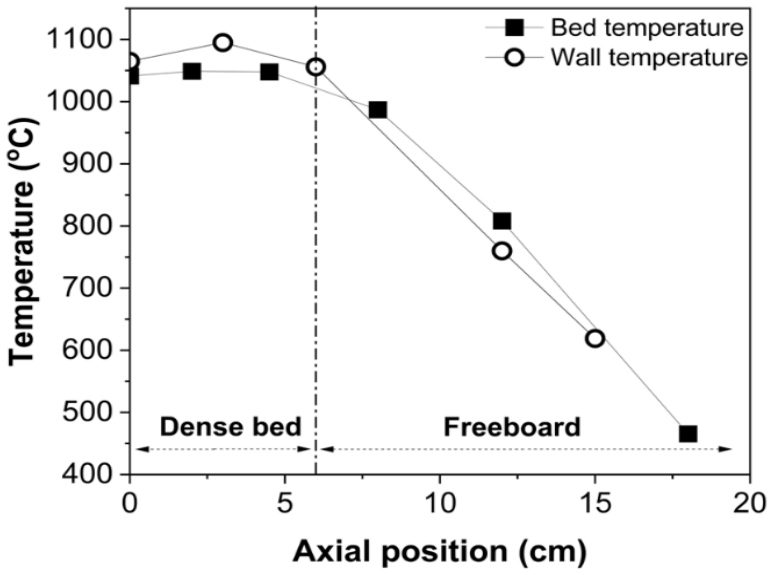

Figure 4.3 Axial temperature distribution in the CH-FBR, illustrating both the dense bed and freeboard regions, at a set dense bed temperature of 1050 °C.

4.4.2 CH_4 conversion and H_2 selectivity

The gaseous product stream consisted of unreacted CH_4, N_2, H_2, and a minor fraction of C_2 hydrocarbons. Impacts of experimental conditions, including temperature, mean residence time, and inlet molar fraction, on CH_4 conversion for both heating methods are presented in Figure 4.4. The temperature in the case of MW heating represents the solid temperature measured by pyrometer #1, Figure 4.1a, while for conventional heating, it is the dense bed temperature measured at 2.0 cm above the gas distributor, Figure 4.1b.

a)

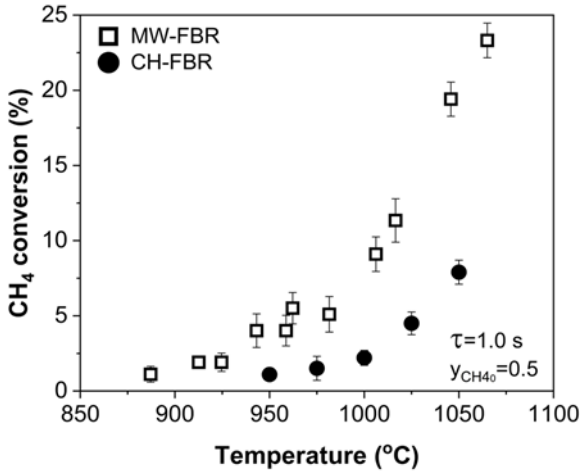

b)

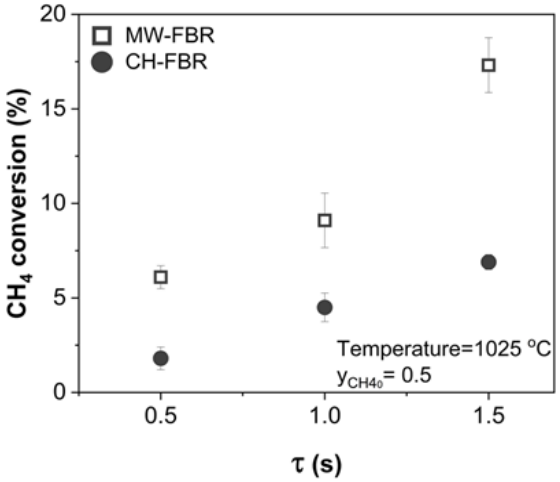

c)

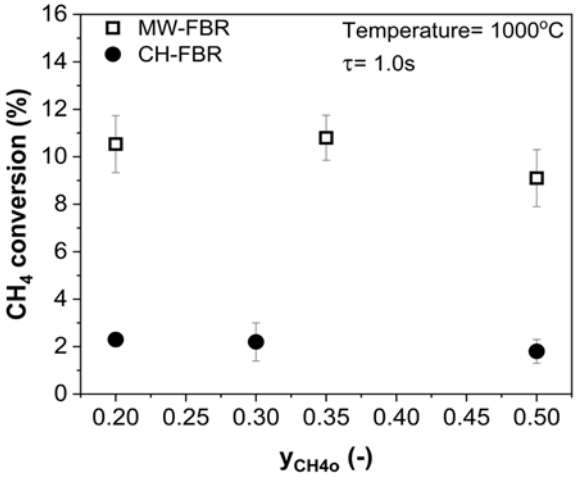

Figure 4.4 CH4 conversion in MW-FBR and CH-FBR at different a) temperature, b) τ, and c) $y_{CH_{4_o}}$.

Higher reaction temperatures favored CH_4 conversion. In MW-FBR, at a mean residence time of 1.0 second, CH_4 conversion increased from 2% at 920 °C to 23% at 1065 °C, Figure 4.4a. The endothermic nature of the reaction favors the conversion at a higher reaction temperature. CH_4 conversion also increased from 6% to 17% upon increasing the mean residence time from 0.5 s to 1.5 s at 1025 °C, Figure 4.4b. A higher residence time favors CH_4 conversion as the experimental

conversion is far from the equilibrium conversion, which approaches 99% at 1000 ºC, Figure A.1. CH_4 inlet molar fraction had a minor effect on CH_4 conversion, Figure 4.4c.

MW heating significantly enhanced CH_4 conversion compared to conventional heating, Figure 4.4. This enhancement in CH_4 conversion might be attributed to the MW thermal effect and formation of hotspots. Hotspots are microscale points where the local temperature considerably exceeds that of their surroundings. Inhomogeneous distribution and dissipation of MW energy cause hotspots, occurring due to intensified electromagnetic fields in narrow gaps between dielectric particles, uneven particle surfaces, and local differences in dielectric properties [89]. Microscale hotspots are difficult to capture experimentally, as the pyrometer's spot size is orders of magnitude larger than the hotspots. By comparing the baseline CH_4 conversion from the CH-FBR to CH_4 conversion from MW-FBR in the temperature range of 950–1050 °C, Figure 4.4a, hotspots contribute approximately 50% to 70% of the CH_4 conversion observed in the MW-FBR. A similar observation was made in a comparative study by Domínguez et al. [84] on CH_4 catalytic pyrolysis over activated carbon in a fixed bed under MW and conventional heating. MW heating achieved higher CH_4 conversion, with hotspots contributing about 40% to 60% of the total CH_4 conversion.

Results of H_2 selectivity at different temperatures and CH_4 conversion levels are shown in Figure 4.5a and b. The highest H_2 selectivity of 98% was obtained at the highest temperature of 1065 ºC, Figure 4.5a. H_2 selectivity increased with CH_4 conversion, Figure 4.5b. CH_4 pyrolysis follows a stepwise dehydrogenation: $2CH_4 \xrightarrow{-H_2} C_2H_6 \xrightarrow{-H_2} C_2H_4 \xrightarrow{-H_2} C_2H_2 \xrightarrow{-H_2} H_2 + 2C$. Therefore, increasing the temperature or the residence time favors H_2 productivity at the expense of C_2 hydrocarbons, Figure A.2. H_2 selectivity was higher under MW heating as compared to the conventional heating at the same temperature, Figure 4.5a. Nonetheless, the difference in H_2 selectivity between the two heating methods decreased at higher temperatures (above 1000 °C). At 1050 °C, both methods achieved H_2 selectivity above 90%. This is due to the higher CH_4 conversion in MW-FBR compared to CH-FBR at the same measured temperature. H_2 selectivity is influenced by the degree of CH_4 conversion, as shown in Figure 4.5b. At the same CH_4 conversion level, both heating methods produced comparable H_2 selectivity. When CH_4 conversion reached 10% and above, H_2 selectivity exceeded 90%, as depicted in Figure 4.5b.

CH_4 conversion in MW-FBR exceeds that of molten salt bubble columns reported in the literature under comparable conditions, while the conversion in CH-FBR closely matches that of the molten

salt bubble columns [90,91]. For instance, Palmer et al. reported a CH_4 conversion of 10–15% and an H_2 selectivity of 95% at 1050 °C and a residence time of 0.75 s in a lab-scale molten salts reactor, which closely aligns with our results for the CH-FBR system. This highlights the enhanced performance of MW-FBR in terms of CH_4 conversion while demonstrating the comparable efficiency of CH-FBR to molten salt bubble columns.

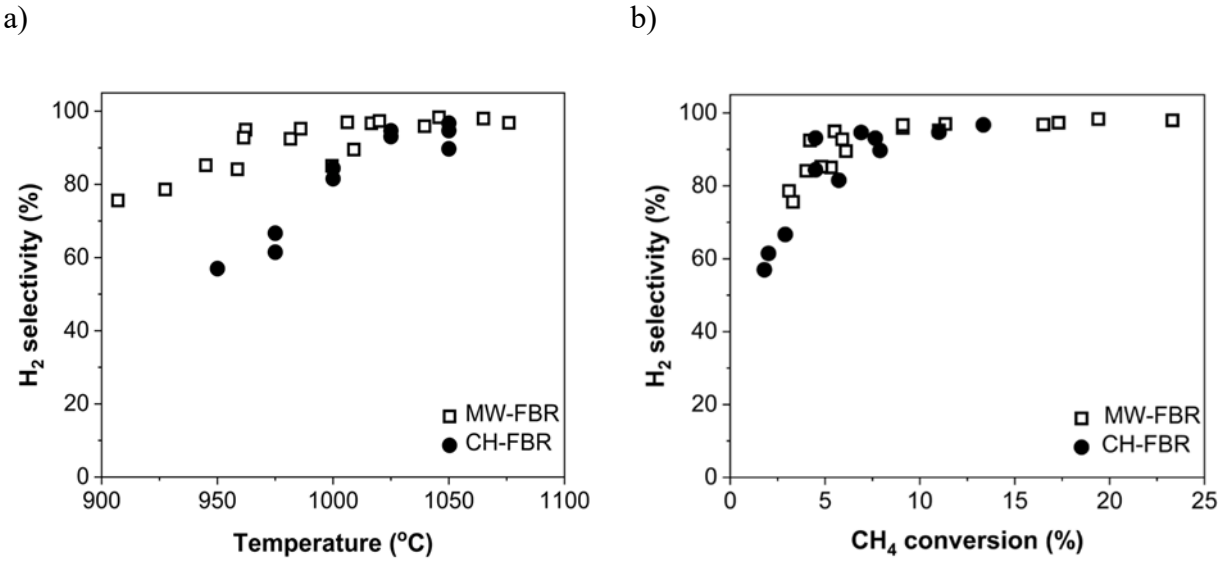

Figure 4.5 Variation of H2 selectivity in MW-FBR and CH-FBR with a) temperature and b) CH4 conversion.

4.4.3 Pyrolytic carbon capture efficiency

In CH_4 thermal pyrolysis, identifying the location of the formed carbon is crucial for optimizing recovery, preventing reactor clogging, and ensuring efficient separation and utilization of carbon co-products. Capturing carbon on the fluidized particles is desirable for effective carbon management and commercial pyrolytic carbon production. To estimate the efficiency of carbon capture, the selective carbon deposition on the fluidized particles, we compared the rate of carbon deposition (r_d) on the particles to the rate of carbon production (r_p). We estimated the ratio (r_d/r_p) to quantify the experimental carbon capture efficiency. The highest theoretical value of (r_d/r_p) at

100% means that all pyrolytic carbon produced from CH_4 pyrolysis is captured on the fluidized particles. We determined r_p from the mass balance on the carbon atom according to Eq. (4.7).

$$r_p = \left[n_{CH_{4,0}} - \left(n_{CH_4} + 2\sum n_{C_2}\right)\right] MW_c/W_S \tag{4.7}$$

r_d was calculated from the slope observed across three points of carbon content increases over time-on-stream (TOS). Total TOS was 180 minutes, and we measured the carbon content every 60 minutes, Figure A.4. A summary of adopted conditions and collected results is provided in Table A.1. We determined the amount of deposited carbon on the fluidized particles from MW-FBR and CH-FBR by TGA as highlighted in Section 4.3.3. The release of carbon from the sample started at ~650 ºC and completed at ~850 ºC, e.g., typical weight loss data is shown in Figure A.3. Carbon accumulation on the particles for MW heating was higher than that for the conventional heating at all identical tested conditions. For instance, at 1050 °C, the particles accumulated 5.7 wt.% of carbon in MW-FBR, whereas under the same conditions, CH-FBR resulted in 1.4 wt.% of carbon accumulation, Table A.1. This is attributed, in part, to the higher productivity of carbon in MW heating due to higher CH_4 conversion as compared to conventional heating as discussed in Section 4.4.2.

Variations of r_d/r_p with the heating method, r_p at different operating conditions, namely; temperature, superficial velocity, and CH_4 inlet molar fraction, are shown in Figure 4.6a-d. Reported points in this figure are an average of three measurements each 60 minutes and the error bars are the standard error of the mean. r_d/r_p for MW heating ranged between 61–89%, Figure 4.6a. For conventional heating, r_d/r_p ranged between 35–55%, Figure 4.6a. Therefore, MW heating increased pyrolytic carbon capture by fluidized particles by an average of 70% as compared to conventional heating. The non-isothermal conditions between the gas and the solid within the reaction zone in MW-FBR favored the capture of pyrolytic carbon by the particles. Due to high solid temperature and low gas temperature, the high rate of carbon formation is limited to the surface of the solid particles and within the narrow thermal boundary layer around the solid particles. Bubbles in the dense bed and the gas in the freeboard are at a lower temperature than solids in the emulsion phase of the dense bed, thus less contributing to CH_4 conversion and carbon formation. This condition limits CH_4 decomposition and carbon deposition outside of the dense bed, leaving most of the carbon product on the hot fluidized particles. Accordingly, a high r_d/r_p

ratio was obtained in MW-FBR as compared to CH-FBR with isothermal conditions between the gas and the solid. In CH-FBR, the gas bubbles and the freeboard area are at a high temperature that contributes to CH_4 conversion and carbon formation, Figure 4.3. Hence, a lower r_d/r_p ratio compared to MW heating was observed. Non-isothermal conditions between the deposition surface and the fluid carbon source substantially increased the deposition rate compared to isothermal conditions reported in previous literature, aligning with the current findings [92]. D. Rovillain et al. deposited pyrolytic carbon using a reactor with an internal resistive heating element, achieving a 500 °C temperature difference between the deposition surface (1300 °C) and fluid carbon source (800 °C) [92]. This configuration resulted in deposition rates of two orders of magnitude higher than classical isothermal pyrolysis, due to localized acceleration of the deposition kinetic from the steep temperature gradient [92].

a)

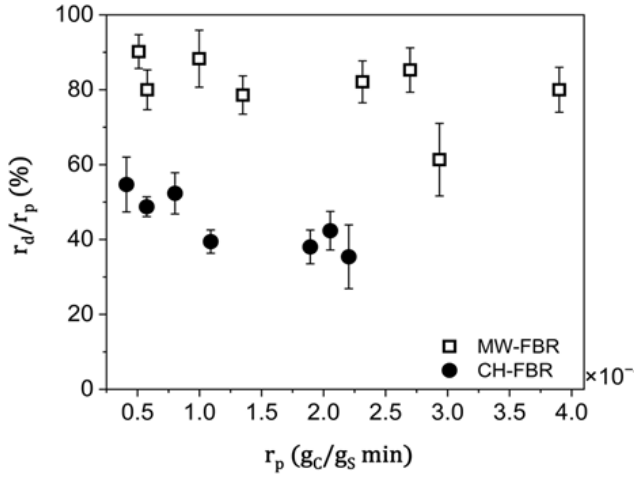

b)

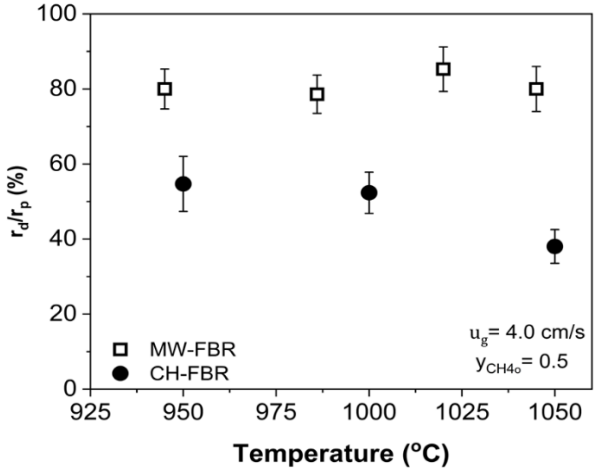

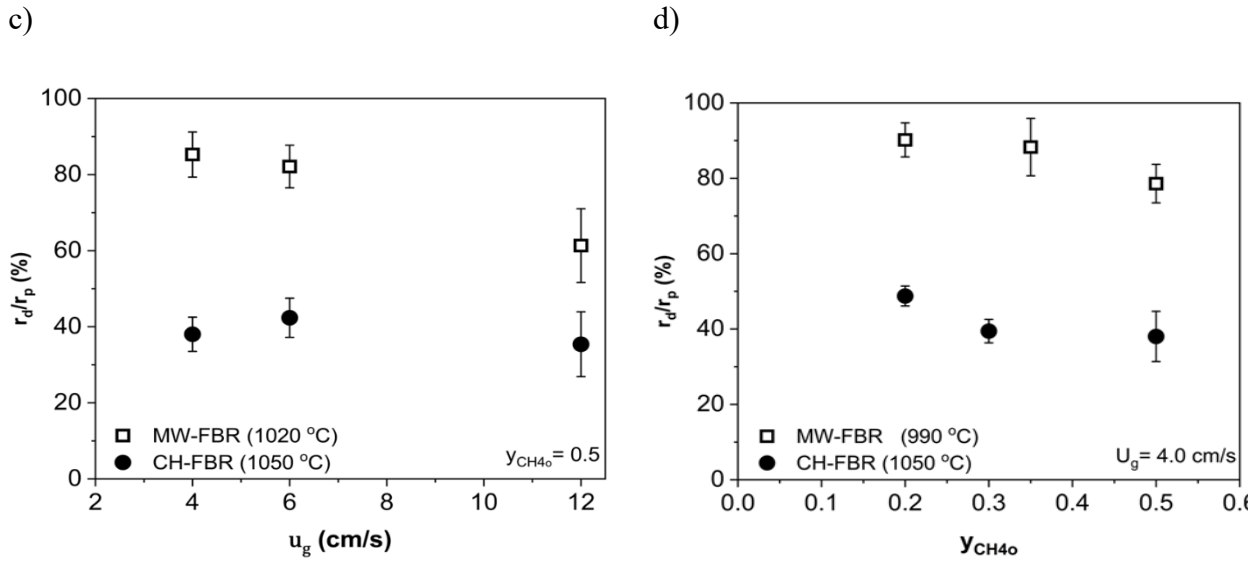

Figure 4.6 Variation of r_d/r_p in MW-FBR and CH-FBR with a) r_p , b) temperature, c) u_g, and d) $y_{CH_{4_o}}$.

Additionally, the temperature gradient between the particulate bed and reactor wall contributes to improved selective carbon deposition on the surface of the fluidized particles. In MW-FBR, the reactor wall temperature is approximately 250 °C lower than the particle temperature, Figure 4.2. Consequently, carbon deposition shifts to fluidized particles. In conventional systems, the reactor wall accumulates a high amount of carbon due to its higher temperature compared to the bed temperature. Figure 4.7 shows photos of the MW-FBR wall in intervals for 23 hr TOS. The carbon deposits on the wall were confined to the dense bed area, with no carbon deposits observed in the freeboard zone. Limited carbon accumulation on the reactor wall also contributes to high carbon capture by the hot fluidized particles in MW-FBR. It was shown in the study by Yu et al. [93] that the carbon deposition rate increased by 400% on hot deposition substrate in cold wall reactors as compared to hot wall reactors, attributed to the steep temperature and concentration gradients enhancing carbon flux and localized pyrolysis, leading to more efficient carbon deposition.

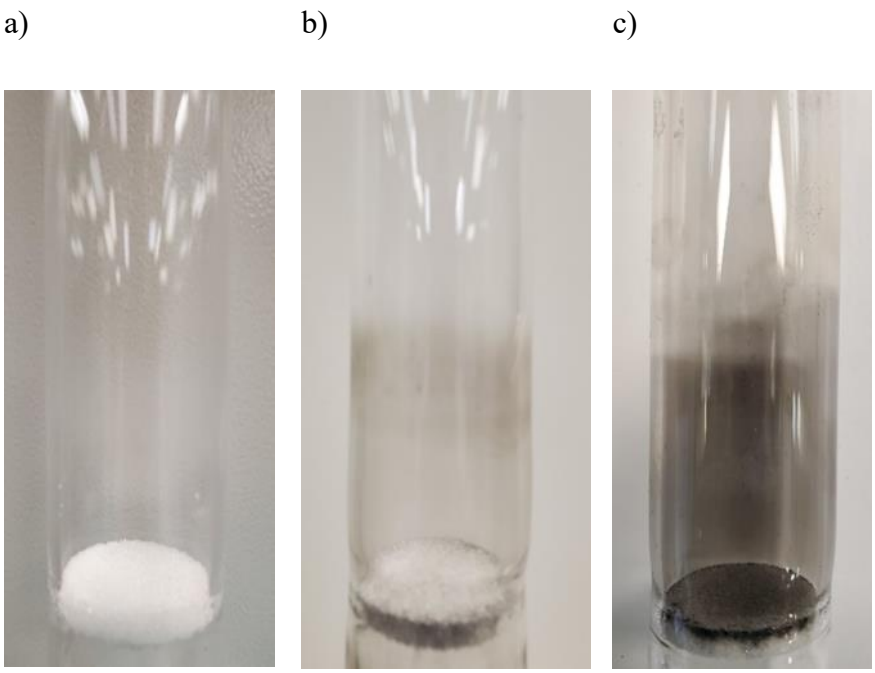

Figure 4.7 Visual observations of carbon accumulation on the reactor wall in the MW-FBR unit after TOS of a) 0 hours, b) 10 hours, and c) 23 hours.

Conversely, in CH-FBR, the reactor wall in the dense bed has the highest temperature, promoting carbon deposition on the wall. This results in less carbon deposition on solid particles and a lower r_d/r_p ratio compared to MW heating. Experimental observations on carbon deposits on the reactor wall in CH-FBR are provided in Section A.2 of the Appendix A.

Temperature variation (945–1045 °C) did not significantly affect r_d/r_p ratio for MW-FBR, which remained consistently within the range of 80–85%, as shown in Figure 4.6b. In contrast, for CH-FBR, r_d/r_p decreased from 55% to 38% when the temperature increased from 950 °C to 1050 °C, as illustrated in Figure 4.6b. In CH-FBR, the temperature difference between the reactor wall and the particulate bed increased with the set point bed temperature. For example, at set point dense bed temperatures of 950 °C and 1050 °C, the wall temperatures were 975 °C and 1095 °C, respectively. This increasing temperature difference likely explains the lower r_d/r_p ratio at higher bed temperatures in conventional heating. This trend was absent in MW-FBR, where the

temperature difference between the wall and particles remained relatively constant for all particle temperatures, as shown in Figure 4.2.

In MW-FBR, increasing u_g decreased r_d/r_p from 82% at 4.0 cm/s and 6.0 cm/s to 61% at 12 cm/s, Figure 4.6c. This reduction in r_d/r_p might be due to attrition and elutriation of carbon deposits on the fluidized particles at higher u_g. Conversely, this trend was not observed in CH-FBR, likely because of the lower amount of deposited carbon, Figure 4.6c. The attrition of carbon layers from the external particle surface is proportional to the amount of carbon content. The inlet molar fraction did not significantly affect the r_d/r_p ratio for both MW-FBR and CH-FBR, Figure 4.6d.

4.4.4 Carbon characterization

4.4.4.1 SEM-EDX

SEM images of SiC particles and C-SiC produced at 1050 ºC in MW-FBR (labeled MW-1050) and CH-FBR (labeled CH-1050) are shown in Figure 4.8. SiC surface was smooth and non-porous with sharp edges, Figure 4.8a. The surface contained some impurities attached to it. EDX results show that the surface mainly consisted of carbon (58 At.%) and silica (41 At.%). Oxygen (1–2 At.%) might have originated from oxidation of the surface at ambient conditions. Impurities attached to the surface originated from the same SiC material (SiC dust) in addition to Al and Fe at < 1.0 At.%.

The surface of the MW-1050 sample had an increased roughness compared to SiC and it is covered by curved planes of pyrolytic carbon with boundaries between the planes, which resembles a hemispherical cauliflower shape deposition, Figure 4.8b. Similar morphology was observed in pyrolytic carbon deposition over carbonaceous surfaces [94,95], SiC [96], and alumina [97,98] at processing temperatures in the range of 1000–1400 ºC in conventional heating systems.

The morphology of the pyrolytic carbon deposited on the surface did not distinctively change between the two applied heating methods, Figure 4.8b and c. However, the surface of MW-1050 has an increased roughness, and the grains are larger compared to CH-1050, which highlights the formation of thicker layers of deposition on the base solid particle due to a higher amount of deposited carbon. EDX of both samples showed that the solid surface contained carbon at 100 At.%.

a)

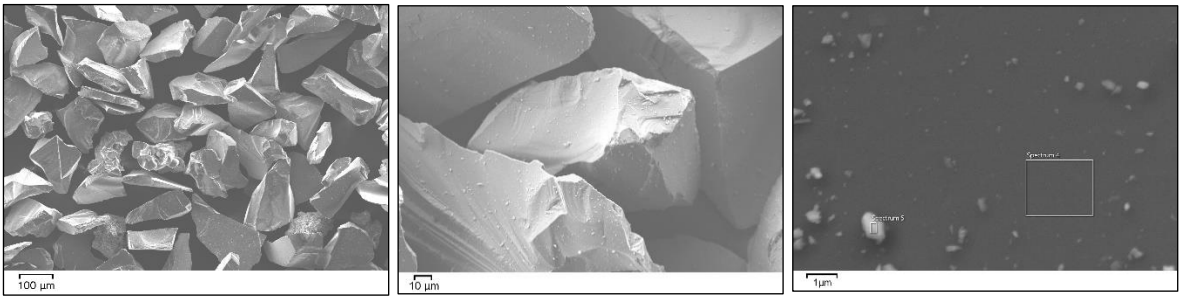

b)

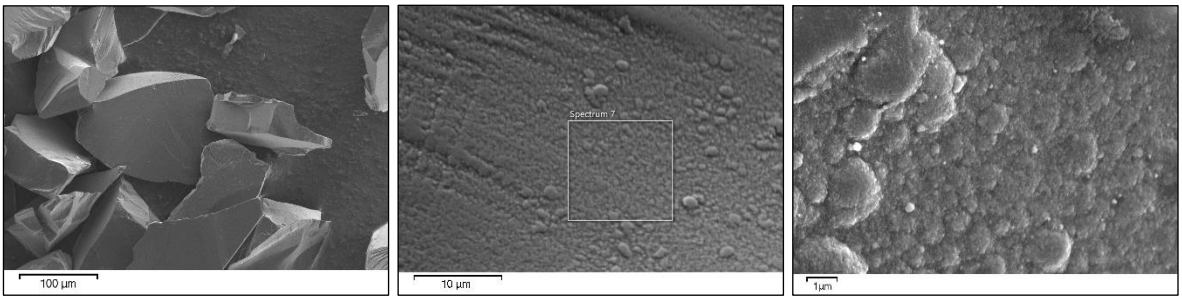

c)

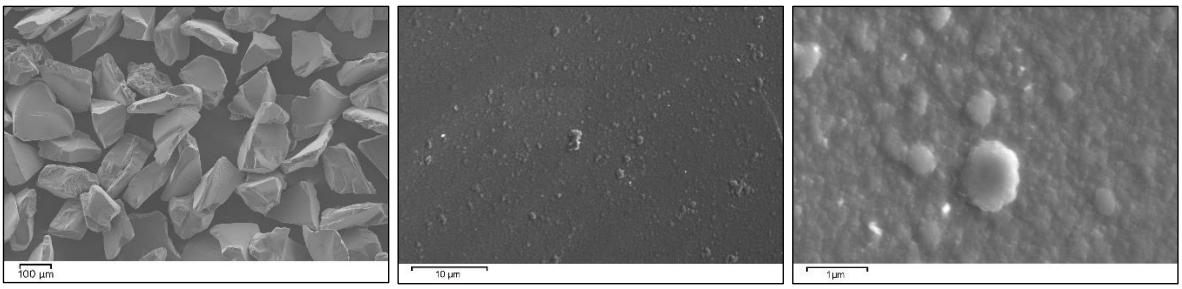

Figure 4.8 SEM images at different magnifications of a) SiC, b) MW-1050, and c) CH-1050.

4.4.4.2 Raman

To assess the quality of the pyrolytic carbon product and quality variation with the applied heating method and temperature, Raman spectra of SiC particles and C-SiC particles from MW-FBR and CH-FBR produced at 950 ºC and 1050 ºC were obtained and shown in Figure 4.9. Raman spectra

of the SiC particles peaked at 160 cm^{-1}, 765 cm^{-1}, 785 cm^{-1}, and 970 cm^{-1}, typical spectra of polytype 6H-SiC surface, Figure 4.9a. C-SiC spectra displayed major Raman peaks, the *G-band* at 1585 cm^{-1} and the *D-band* at 1350 cm^{-1}. The *G-band* arises from the vibrations of well-ordered, sp^2 hybridized carbon atoms within the crystalline regions of the carbon material. The *D-band* originates from structural defects and disorders in the carbon lattice and is associated with the breathing mode of sp^2 hybridized carbon atoms. Therefore, the results reveal that the collected pyrolytic carbon deposits from both heating methods had a graphitic nature with different degrees of distortion.

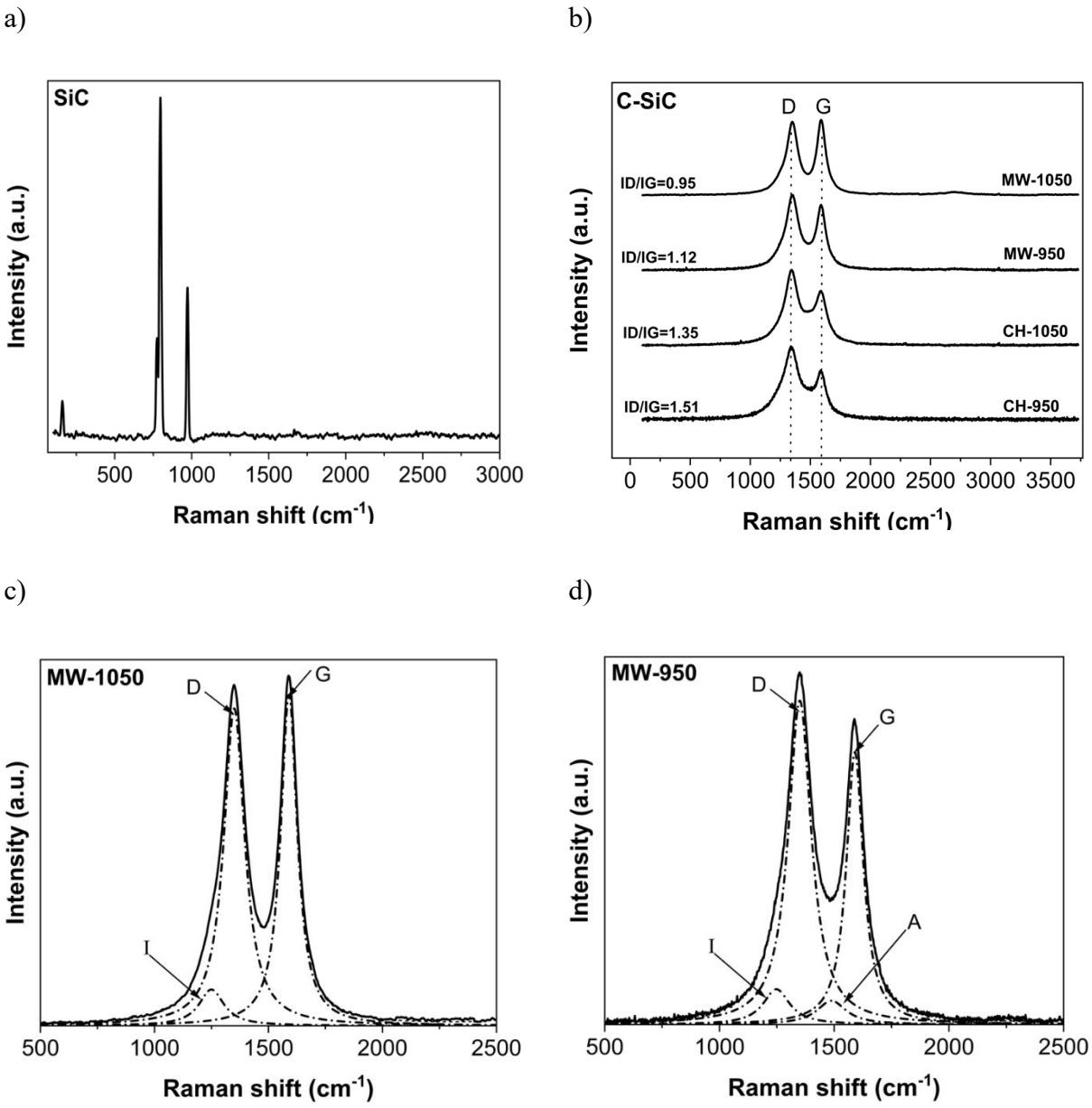

e) f)

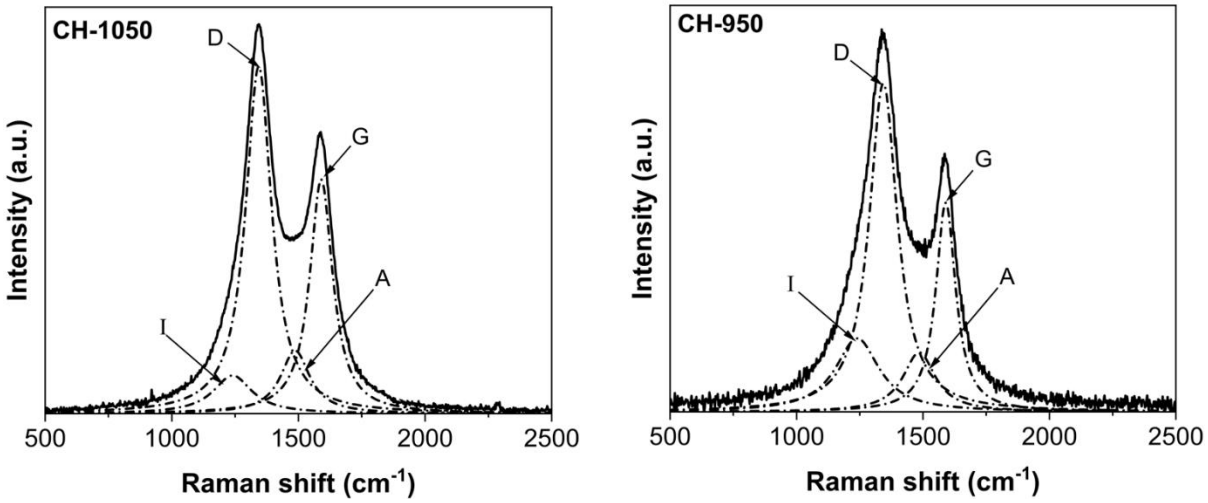

Figure 4.9 Raman spectra of a) SiC, b) C-SiC produced in MW-FBR and CH-FBR at different temperatures; and peak deconvolutions of c) MW-1050, d) MW-950, e) CH-1050, and f) CH-950.

The Raman spectra were further analyzed and deconvolved into sub-bands. Various peak analysis methods, including Gaussian, Lorentzian, and Gaussian-Lorentzian, were employed to enhance the precision in determining spectroscopic parameters, such as peak position, bandwidth, and line shape. The Lorentzian method provided better goodness-of-fit compared to Gaussian and Gaussian-Lorentzian methods in terms of the sum of residuals and the sum of squares. The results of the fitting procedure in terms of band shape and position are in close agreement with analysis in the literature performed on pyrolytic carbon [99].

Two additional sub-bands, the *I-band* at 1250 cm^{-1} and the *A-band* at 1490 cm^{-1}, were identified in the deconvoluted C-SiC Raman spectra (Figure 4.9e-f). These bands are commonly observed in studies involving disordered carbon materials. The *I-band* is associated with a disordered graphitic lattice in A_{1g} symmetry, while the *A-band* is attributed to amorphous sp^2 bonded carbon [100,101]. The *I-band* and the *A-band* are relatively broad compared to the *G-band* and the *D-band*, Figure 4.9d-f. Raman spectra had similar shapes in the analyzed samples with differences in the band

intensities. The *G-band*, *D-band,* and *I-band* were observed in all samples. The *A-band* was not observed in sample MW-1050, Figure 4.9c.

Structural information is derived from spectral parameters, including the band intensity ratio (I_D/I_G), integral intensity ratio (A_D/A_G) of the *D-band* and *G-band*, and the full width at half maximum of the *D-band* ($FWHM_D$). A lower I_D/I_G ratio indicates a higher degree of graphitization. The I_D/I_G ratio in the analyzed samples ranged between 0.95–1.51 and followed the order of MW-1050<MW-950<CH-1050<CH-950, Figure 4.9b and Table 4.3. Therefore, sample MW-1050 had the highest degree of graphitization, while CH-950 had the lowest degree of graphitization. Hence, MW heating produced better quality pyrolytic carbon as compared to conventional heating characterized by a higher degree of graphitization. In addition, increasing the temperature increased the carbon graphitization degree in both heating methods. This is similar to what was observed in the study by Feron et al. [102]. They noted that when employing CH_4 as a precursor gas for chemical vapor deposition in a conventional heating system, an increase in the temperature from 950 °C to 1100 °C resulted in a transformation of the deposited pyrolytic carbon structure. This transformation involved a shift from a low-textured to a high-textured configuration with a higher degree of graphitization. It was reported in the study by Zeng et al. that a change in the deposited carbon structure resulted from increasing the temperature conventionally from 1050 ^oC to 1150 ^oC, which yielded a decrease in I_D/I_G ratio from 0.99 to 0.85 [103].

A decrease in $FWHM_D$ correlates with a higher degree of graphitization [104]. $FWHM_D$ in the analyzed samples ranged between 111–135 cm^{-1} and followed the order of MW-1050<MW-950<CH-1050<CH-950, Table 4.3. It was observed in the study by Hareesh, et al. [105] that the $FWHM_D$ decreased from 36.9 cm^{-1} to 30.2 cm^{-1} upon increasing pyrolysis temperature from 1800 ^oC to 2200 ^oC in a conventional heating system.

In the thermal deposition of carbon from CH_4, the degree of graphitization is strongly influenced by the temperature. Graphitization is the process by which carbon atoms arrange themselves into a crystalline, hexagonal lattice structure, similar to graphene or graphite. At deposition temperatures below 800 ^oC, the graphitization of carbon materials is limited. The formed carbon structures tend to be amorphous and highly disordered. The lower thermal energy available at these temperatures results in weaker carbon-carbon (C-C) bond formation and less mobility of carbon atoms to arrange into well-ordered hexagonal structures. At high deposition temperatures, typically above 1400 °C,

the graphitization process is highly favored. Thermal energy is sufficient to promote strong C-C bond formation and carbon atom mobility, leading to more growth of well-ordered, crystalline graphitic structures. Hence, carbon deposited at high temperatures is more likely to exhibit a high degree of graphitization and a more graphitic or graphene-like structure.

In the intermediate temperature range (800–1400 °C), the degree of graphitization is increasingly sensitive to temperature. This temperature window offers a balance between thermal energy and mobility of carbon atoms, enabling the formation of a mixture of both graphitic (highly ordered) and amorphous (less ordered) structures. As the temperature within this range increases, several factors contribute to the higher degree of graphitization. The increased thermal energy facilitates the breaking and reforming of C-C bonds, allowing carbon atoms to rearrange into more ordered hexagonal structures akin to graphite. In addition, the enhanced mobility of carbon atoms enables them to find energetically favorable positions within the lattice, reducing defects and promoting crystalline growth. Consequently, carbon deposited at higher temperatures within this range tends to exhibit a greater degree of graphitization.

Carbon produced through MW heating exhibited a lower I_D/I_G ratio compared to carbon produced through conventional heating at the same measured temperature, 0.95 vs 1.35 at 1050 ºC and 1.12 vs 1.51 at 950 ºC, Figure 4.9. This suggests that carbon deposition in MW heating was at a higher effective temperature than what was measured by the pyrometer, and it reflects on the impact of the higher solid temperature and hotspots formation, contributing to a higher degree of graphitization and the observed relatively higher CH_4 conversion discussed in Section 4.4.2.

The I_D/I_G ratio was adopted to empirically calculate the in-plane crystallite size L_a by Eq. (4.8) proposed by Mallet-Ladeira et al. [106], which takes into account the variation of the spectral properties with the applied wavelength.

$$L_a = \frac{4.4}{(I_D/I_G)}\left(\frac{2.41}{E_L}\right)^4 \tag{4.8}$$

where E_L is the excitation energy of the laser, which for a wavelength of 532 nm equals 2.32 eV. The values of L_a are shown in Table 4.3. L_a increased from 4.4 nm to 5.3 nm upon increasing the pyrolysis temperature in MW heating from 950 °C to 1050 °C. L_a showed a less significant change and ranged from 3.5 nm to 3.7 nm when heating the bed conventionally. These results suggest that

the deposition temperature improved the crystallite size of the pyrolytic carbon in line with other findings reported in the literature [107].

The presence and intensity of the *A-band* at 1490 cm^{-1} and the *I-band* at 1200 cm^{-1} is proportional to the number of sp^3 carbon atoms present, which is relative to the amount of amorphous carbon. Carbon bonded to sp^3 exhibits vibrational features at wavelength below 1500 cm^{-1} [100]. Estimation of $sp^2/(sp^2 + sp^3)$ ratio is possible by the integrated bands' intensities *A-band, I-band, D-band,* and *G-band* [108]. Based on the area of these respective peaks, MW-1050, MW-950, CH-1050, and CH-950 contained 91, 88, 81, and 72% of sp^2 bonded carbon, respectively, Table 4.3.

Table 4.3 Raman spectra of C-SiC produced at different temperatures from MW-FBR and CH-FBR

	MW-1050	**MW-950**	**CH-1050**	**CH-950**
G-band (cm^{-1})	1584	1585	1585	1585
D-band (cm^{-1})	1350	1350	1343	1343
$FWHM_D$ (cm^{-1})	111	122	125	135
I_D/I_G	0.96	1.13	1.34	1.55
A_D/A_G	1.31	1.58	1.46	2.05
$sp^2/(sp^2+sp^3)$ (%)	91	88	81	72
La (nm)	5.3	4.4	3.7	3.5

4.4.4.3 XPS

We deconvoluted C1s XPS of SiC and MW-1050 to identify dominant surface bonds and to evaluate the degree of pyrolytic carbon graphitization. The C1s spectrum of SiC shows peaks of C-Si at 282.5 eV (carbon in silicon carbide), O-Si-C at 283.1 eV (carbon in silicon oxicarbide), C-

O at 286.7 eV, and C=O at 289.0 eV, Figure 4.10a. Oxygen incorporation can occur due to surface oxidation. In addition, C-C in sp^3 configuration at 285.0 eV from bulk SiC surface [109]. The full XPS results along with peak fitting parameters are provided in Table A.2 and Table A.3.

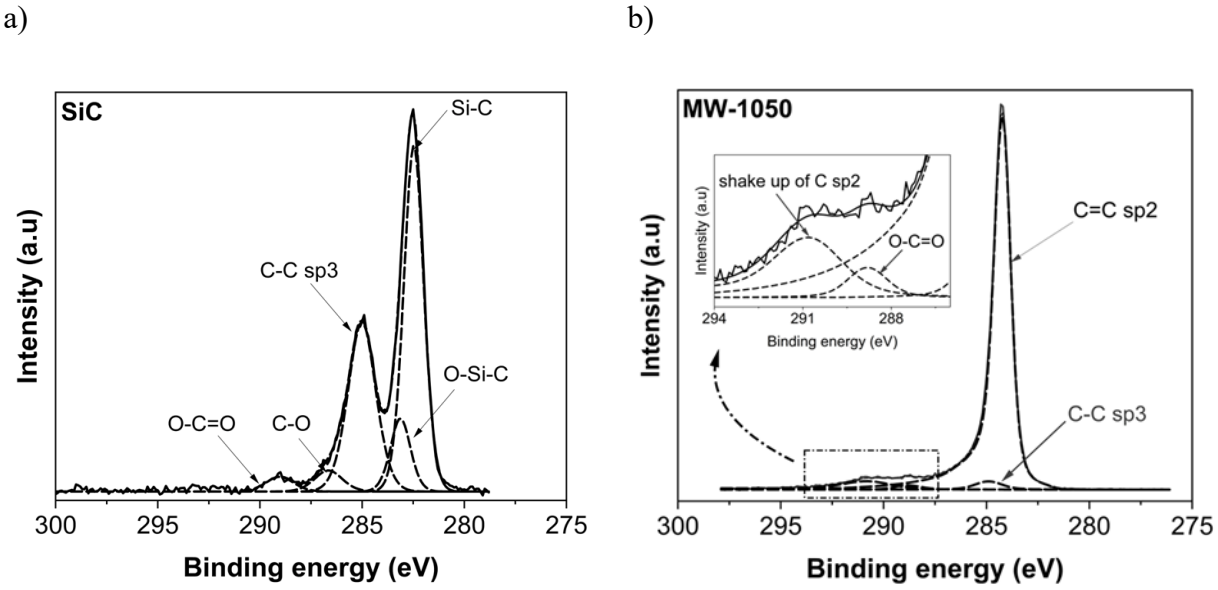

Figure 4.10 Deconvolution of C1s of XPS spectra for a) SiC and b) MW-1050.

Regarding MW-1050, the C1s spectrum is predominantly represented by an immerged peak at binding energy of 284.2 eV corresponding to C–C bonds in the sp^2 configuration, implying a graphitic phase deposition, Figure 4.10b. The absence of the C-Si peak at 282.5 eV in this sample indicates that the XPS spectrum is from the deposited carbon surface, with no contribution from the SiC surface. Carbon in the sp^3 configuration is detected at the binding energy of 285.0 eV with reduced intensity. In addition, a peak emerged at higher binding energy (290.4 eV) and is identified as a shake-up of the 284.2 eV peak. The shake-up peak is a signature of graphitic carbon, which shifts to higher bonding energy by ~6.5–7.0 eV of the main peak and has intensities of 5-10% of the main peak [110]. The corresponding $sp^2/(sp^2+sp^3)$ ratio is 97% and is close to the estimated value by Raman at 91%, Table 4.3.

4.4.5 Process transient behavior

Transient temperature and CH_4 conversion in MW-FBR over 18 hr and for three superficial gas velocities of 4, 6, and 12 cm/s, and an inlet CH_4 molar fraction of 20% are presented in Figure 4.11a. The amount of pyrolytic carbon deposited on the fluidized particles and the transient H_2 selectivity and its variation with transient solid temperature are shown in Figure 4.11b, c, and d. A synergetic behavior of increased solid temperature and CH_4 conversion exists due to increased carbon deposition over time. For instance, at 4 cm/s with an initial carbon content of 0.45 wt.%, CH_4 conversion was at 1% at a solid temperature of 855 °C. Carbon deposition increased slowly to 1.45 wt.% in the subsequent 9 hr accompanied by an increase in solid temperature to 980 °C and CH_4 conversion to 9.8%. Carbon deposition continued to increase to 4.2 wt.% at the end of the test, while the solid temperature did not increase further, and CH_4 conversion remained constant after 10 hr onward. The same trends were observed for superficial gas velocities of 6 and 12 cm/s. Higher superficial gas velocity yielded less CH_4 conversion due to less residence time as discussed in Section 4.4.2. The increase in solid temperature with increasing carbon deposition is attributed to enhanced dielectric properties of solid particles due to carbon accumulation. For instance, C-SiC with a carbon content of 4 wt.% exhibited a tan(δ) of 0.46 and an electrical conductivity of 1.85 S/cm, compared to SiC particles, which had a tan(δ) of 0.14 and an electrical conductivity of 0.02 S/cm. See the discussion in Section A.3 of the Appendix A.

a)

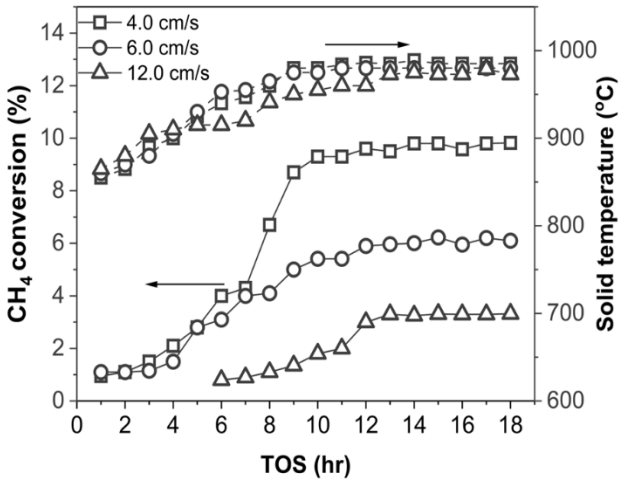

b)

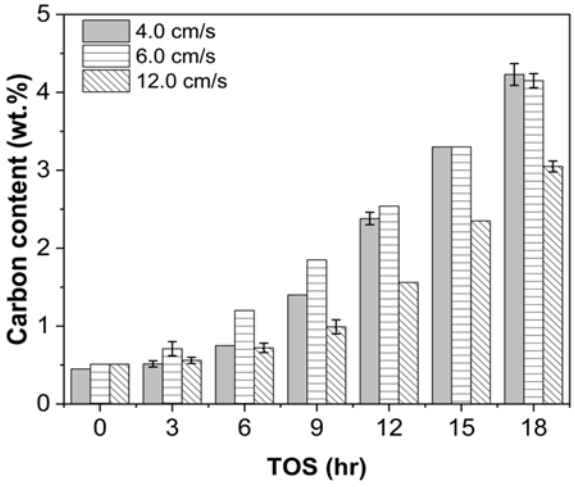

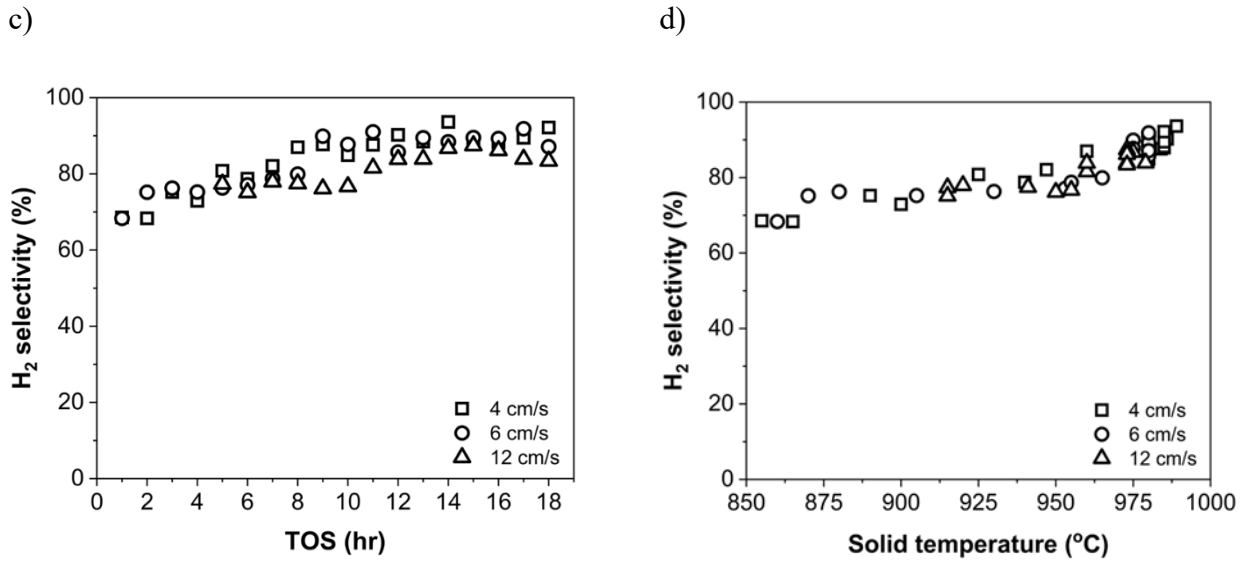

Figure 4.11 Transient performance in MW-FBR for 18 hr TOS showing a) variation of solid temperature and CH4 conversion with TOS, b) variation of carbon content with TOS, c) variation of H2 selectivity with TOS, and d) variation of H2 selectivity with the transient

H_2 selectivity increased with the increase in temperature and CH_4 conversion. H_2 selectivity was 70% at the start of the experiment and increased to 85–90% after 10–12 hr and remained stable until the end of the tests, Figure 4.11c and d.

The calculated amount of carbon produced, and the measured amount of carbon deposited on the particles are reported in Table 4.4. Carbon mass balance that includes the weight of the filter yielded over 100% for all superficial velocities. This is due to the attrition and elutriation of solid particles. Solid particles with the size of 1–3 μm were elutriated from the bed and accumulated in the gas filter, Figure A.5.

The transient behavior of MW-FBR in CH_4 thermal pyrolysis contrasts with the transient behavior of catalytic pathways, where CH_4 conversion inevitably declines over time due to catalyst deactivation. The enhanced performance of MW heating due to increased dielectric properties as a result of pyrolytic carbon deposition, enables the applicability of a broader range of cost-effective base materials, even those with insufficient dielectric properties for high-temperature processes. This flexibility can improve the economic feasibility of the process and facilitate the commercial

production of materials for high-end applications, such as energy storage systems, conductive composites, and structural materials.

Table 4.4 Carbon mass balance after 18 hr TOS

u_g (cm/s)	4.0	6.0	12.0
Carbon produced, g	1.6	1.5	1.3 [a]
Carbon deposited on particles, g	1.4	1.3	0.9
Net filter weight, g	0.5	0.7	1.2
Balance, %	118	133	162

[a] The amount of carbon produced was estimated after 6 hr TOS due to initial low CH_4 conversion.

4.5 Conclusions

In this work, we have demonstrated the efficacy of H_2 production and simultaneous carbon capture from CH_4 thermal pyrolysis in a MW-FBR of chemically inert dielectric particles. This process involved decomposing CH_4 into H_2 and pyrolytic carbon at elevated temperatures (900–1065 ^oC), achieved through MW heating, which offers efficient and selective energy transfer.

We observed that CH_4 conversion was enhanced by increasing the solid temperature and residence time with minimal effect of CH_4 dilution. We achieved the highest CH_4 conversion and H_2 selectivity of 23% and 98%, respectively. Carbon capture efficiency on fluidized particles was assessed by comparing the rate of carbon deposition on the particles to the rate of carbon production. Fluidized SiC particles captured up to 90% of the produced pyrolytic carbon. Raman studies on the produced pyrolytic carbon revealed that a higher temperature favors pyrolytic carbon graphitization. Pyrolytic carbon deposition on the base SiC particles increased electrical conductivity and dielectric properties, which favored the particles' heating efficiency under MW radiation and, hence, the process maintained stable CH_4 conversion and H_2 selectivity levels.

The MW-specific heating effects were investigated through a comparative analysis with conventional heating, which served as a baseline to reveal the contributions of MW heating. These effects include the distinct temperature distribution between the gas and solid phases and the formation of localized hotspots. The benefits of these MW-induced effects were evident in the improved process performance: MW heating increased CH_4 conversion by 150% and carbon capture efficiency by 60% compared to conventional heating. Additionally, the degree of pyrolytic carbon graphitization was 30% higher under MW heating.

This study advances the development of MW heating-assisted CH_4 thermal pyrolysis as a CO_2-free H_2 production technology. It provides insights into the specific effects of MW heating on process performance, which are valuable for maximizing H_2 production and optimizing carbon management. Further research will focus on investigating reaction kinetics and elaborating on the impact of MW heating on these kinetics. Understanding the reaction kinetics is critical for optimizing reactor design and simulating larger-scale reactors, which are key steps toward the successful commercialization of MW heating-assisted CH_4 thermal pyrolysis. In addition, a comprehensive techno-economic analysis is required to evaluate the energy efficiency and scalability of the MW heating-assisted process. Developing effective strategies for the separation of pyrolytic carbon from the fluidized bed material or utilizing carbon-coated particles as a final product will also be crucial for process optimization.

Nomenclature

Acronym

C-SiC	Carbon-coated silicon carbide particles
CH-1050	C-SiC produced in CH-FBR at 1050 ^{o}C
CH-950	C-SiC produced in CH-FBR at 950 ^{o}C
CH-FBR	Conventional heating-assisted fluidized bed reactor
$FWHM_D$	Full width at half maximum of the *D-band*

MFC	Mass flow controller
MW	MW
MW-1050	C-SiC produced in MW-FBR at 1050 ºC
MW-950	C-SiC produced in MW-FBR at 950 ºC
MW-FBR	MW heating-assisted fluidized bed reactor
TOS	Time-on-stream (min)

Symbols

A_t	Reactor cross-sectional area (m^2)
$C_{i,0}$	Inlet concentration of gas specie i (mol/m^3)
C_i	Concentration of gas specie i (mol/m^3)
C_p	Particle heat capacity (J/K)
d_p	Particle size (m)
E_L	Laser excitation energy in Raman spectroscopy (eV)
H	Dense bed height (m)
L_a	In-plane crystallite size (nm)
MW_c	Molecular weight of carbon (g/mol)
n_i	Outlet molar flow rate of gas specie i (mol/min)
$n_{i,o}$	Inlet molar flow rate of gas specie i (mol/min)
n_T	Total molar flow rate of the outlet gas stream (mol/min)

r_p	Rate of carbon production (g_C/g_S min)
r_d	Rate of carbon deposition (g_C/g_S min)
S_{H_2}	Hydrogen selectivity (%)
tan(δ)	Dielectric loss tangent (-)
u_{mf}	Minimum fluidization velocity (m/s)
u_g	Superficial gas velocity (m/s)
v_0	Inlet volumetric flow rate (m^3/s)
W_S	Solid particles loading (g)
x_{CH_4}	Methane conversion (%)
y_i	Molar fraction of gas specie i (-)

Greek letters

ε'	Dielectric constant (-)
ε''	Dielectric loss factor (-)
ε_v	Volumetric expansion factor (-)
ρ_p	Particle density (kg/m^3)
σ	Electrical conductivity (S/m)
τ	Mean residence time (s)

CRediT authorship contribution statement

Abdelrahman I. Hussain: Conceptualization, Methodology, Validation, Investigation, Data curation, Writing – original draft, Writing – review & editing. **Jaber Shabanian:** Conceptualization, Methodology, Writing - Review & Editing. **Mohammad Latifi:** Conceptualization, Methodology, Writing - Review & Editing. **Jamal Chaouki:** Conceptualization, Resources, Writing - Review & Editing, Supervision, Project administration, Funding acquisition.

Acknowledgments

The authors acknowledge TotalEnergies, the Natural Science and Engineering Research Council, Canada (NSERC), and OCP Group for their financial support of this study.

CHAPTER 5 ARTICLE 2 – KINETIC INVESTIGATION OF MICROWAVE HEATING-ASSISTED METHANE PYROLYSIS

[a] *Process Engineering Advanced Research Lab, Department of Chemical Engineering, Polytechnique Montreal, C.P. 6079, succ. Centre-Ville, Montreal, QC, Canada H3C 3A7*

[b] *University Mohamed VI Polytechnique, Benguerir, Morocco*

* Corresponding author: Tel.: +1-514-340-4711 X 4034; Fax: +1-514-340-4159.

E-mail addresses: hussain.abdelrahman@polymtl.ca (A.I. Hussain), mohammad.monzavi@polymtl.ca (M.Monzavi), jamal.chaouki@polymtl.ca (J. Chaouki)

(Submitted to Chemical Engineering Journal on July 18, 2025)

5.1 Abstract

MW (MW)-assisted methane (CH_4) pyrolysis is a novel method for hydrogen (H_2) production without direct CO_2 emissions. MW heating benefits from selective volumetric heating and rapid energy transfer. In this work, we investigated the kinetics of CH_4 thermal pyrolysis under MW heating in a fluidized bed reactor (MW-FBR), and we compared it to a conventional heating-assisted fluidized bed reactor (CH-FBR). We conducted experiments across a temperature range of 950–1065 °C and residence times of 0.5–8.0 s at atmospheric pressure. The reaction kinetics were described by a first-order global kinetic model and considered the non-isothermal conditions in MW-FBR between the solid phase and the gas phase. MW-FBR showed higher CH_4 conversion and lower apparent activation energy. These observations are attributed to localized microscale hotspots. We estimated an apparent activation energy of 288 kJ/mol for MW-FBR and 310 kJ/mol for CH-FBR. We estimated the thermal contribution of hotspots to the reaction by comparing the activation energies between MW-FBR and CH-FBR. We estimated that the effect of hotspots is approximated by 5% higher bed effective temperature than the measured solid temperature. Numerical simulation showed that particle contact causes hotspots due to higher MW power dissipation at contact points compared to isolated particles. The kinetic results predict that a complete CH_4 conversion requires an excess of 1050 °C and a residence time in the order of a few seconds.

Keywords: Methane pyrolysis, MW heating-assisted reactor, pyrolysis kinetic, MW thermal effect.

5.2 Introduction

Hydrogen (H_2) is widely recognized as a key energy carrier in the transition toward a low-carbon economy [4]. As a clean fuel, it plays a crucial role in decarbonizing sectors such as transportation, power generation, and industrial processes [63]. Its high energy density (120 MJ/kg) and ability to be produced from a variety of resources make it a versatile option for energy storage and utilization [51]. Unlike fossil fuels, H_2 combustion does not produce carbon dioxide (CO_2) emissions, making it an attractive alternative for mitigating climate change. Additionally, H_2 is a critical feedstock in ammonia synthesis, refining processes, and chemical manufacturing, further expanding its industrial relevance [6]. However, the sustainability of H_2 as an energy carrier depends largely on the method of production. Currently, the majority of H_2 is derived from fossil fuel-based processes, which contribute significantly to greenhouse gas emissions [111]. Transitioning to low-emission H_2 production methods is essential for realizing the full potential of H_2 as a clean energy source.

H_2 is primarily produced through processes such as steam methane (CH_4) reforming (SMR), coal gasification, electrolysis, and thermochemical decomposition [3,8,64]. Among these, SMR remains the dominant method due to its economic viability and large-scale production capability [3,64]. However, SMR and coal gasification are inherently carbon-intensive, requiring additional carbon capture and storage technologies to reduce emissions. Electrolysis, which splits water into H_2 and oxygen using electricity, offers a cleaner alternative when powered by renewable energy sources [64,65]. However, the widespread adoption of electrolysis is currently limited by its high energy consumption and infrastructure costs.

An alternative and promising route for H_2 production is CH_4 pyrolysis, in which CH_4 is thermally decomposed into H_2 and solid carbon without direct CO_2 emissions. CH_4 pyrolysis is an endothermic reaction (ΔH^o=75.6 kJ/mol CH_4) and requires high reaction temperature above 1000 ^oC [66]. This emerging process has attracted growing interest due to its potential to generate H_2 with a lower environmental impact while simultaneously producing valuable solid carbon materials. CH_4 pyrolysis can be conducted via various heating methods, including conventional thermal heating and non-conventional energy sources such as plasma or microwave (MW) irradiation [74–78,112].

MW heating has emerged as an innovative approach to CH_4 pyrolysis due to its unique energy transfer mechanism [80,113,114]. Unlike conventional heating, which relies on thermal conduction

and convection, MW heating directly interacts with MW-absorbing materials (e.g., silicon carbide or carbon) to generate localized heat. This volumetric heating mechanism leads to rapid and selective heating, potentially enhancing reaction rates and energy efficiency. Additionally, MW heating enables localized hotspots, which may influence reaction kinetics and product distribution in ways that differ from conventional heating.

Our previous study demonstrated the potential of CH_4 pyrolysis in MW heating-assisted fluidized bed reactor (MW-FBR) as an effective route for H_2 production [113]. Under MW heating, we observed CH_4 conversions that surpassed conventional heating methods, and excellent H_2 selectivity reaching up to 98%. We observed a temperature difference between the solid and gas phases within the MW-heated bed. Solid particles experienced higher temperatures compared to the surrounding gas, with temperature differences of ~200 ºC. Given the strong temperature sensitivity of CH_4 pyrolysis, MW thermal effects (temperature gradients and hotspots) have large effects on reaction progress. Consequently, conventional treatment of MW-FBR, assuming uniform bed temperature, fails to accurately capture the unique characteristics of MW-assisted pyrolysis. This highlights the necessity for a more detailed analysis that accounts for MW heating thermal effects, specifically in kinetic studies.

Building on these previous insights, this study aims to investigate a global kinetic model for CH_4 thermal pyrolysis in MW-FBR. We aim to address the need to understand MW thermal effects and the temperature distribution on reaction kinetics under MW heating. We employ different techniques to measure these temperature profiles in MW-FBR. To differentiate the unique thermal characteristics of MW-assisted pyrolysis, we conduct comparative experiments in a conventional heating-assisted fluidized bed reactor (CH-FBR) under similar experimental conditions. This comparison highlights the significance of accurately representing temperature gradients in kinetic modeling, as well as the distinctive thermal effects induced by MW heating. Additionally, we use numerical simulations to identify how microscale hotspots form, where they occur, and how they influence local heating within the bed.

5.3 Methods

5.3.1 Experimental

We conducted experiments on CH_4 thermal pyrolysis in an MW-FBR using dielectric silicon carbide (SiC) particles as the bed material. The experimental conditions are summarized in Table 5.1. CH_4 was diluted with nitrogen (N_2) to a concentration of 20%-50% and fed into the reactor, with the gas flow rate controlled by mass flow controllers and solenoid valves. We analyzed the product gas by GC. We measured the solid temperature (T_s) and the wall temperature (T_w) using pyrometers. We used a profile thermocouple to measure the bulk temperature (T_b) at different points in the dense bed and the gas temperature (T_g) at 1.0 cm above the dense bed.

In addition to MW-FBR, we conducted conventional heating CH_4 thermal pyrolysis in a conventional heating-assisted fluidized bed reactor (CH-FBR). A comprehensive discussion of the experimental setups of MW-FBR and CH-FBR can be found in [113].

Table 5.1 Experimental conditions for CH4 thermal pyrolysis in MW-FBR and CH-FBR

Property	**Value**
Temperature, (^{o}C)	950–1065
Total pressure, (atm)	1.0
Mean residence time τ, (s)	0.5–8.0
Inlet CH_4 concentration, (mol %)	20–50
Solid particles loading W_S, (g)	30–50
Dense bed height H, (m)	$(4.0–8.0)\times10^{-2}$
Superficial gas velocity u_g, (m/s)	$(4.0–12)\times10^{-2}$
u_g/u_{mf} (-)	2.0–6.0

We estimated CH_4 conversion (x_{CH_4}) using Eq. (5.1), accounting for the change in volumetric flow rate due to the increased number of moles produced per mole of CH_4 converted:

$$x_{CH_4} = \frac{C_{CH_{4,0}} - C_{CH_4}}{C_{CH_{4,0}} + \varepsilon_v \, C_{CH_4}} \tag{5.1}$$

To compute the molar flow rates of individual gases (n_i), we applied Eq. (5.2), and the total molar flow rate (n_T) was obtained by Eq. (5.3):

$$n_i = y_i \, n_T \tag{5.2}$$

$$n_T = \frac{n_{N_2}}{y_{N_2}} \tag{5.3}$$

We calculated the mean residence time (τ) using Eq. (5.4):

$$\tau = \frac{A_t \, H}{v_0 (\frac{T_g}{T_0})} \tag{5.4}$$

We estimated the gas temperature inside the bed via two correlations developed by Hamzehlouia et. al. [15], Eq. (5.5) and Eq. (5.6). They employed experimental data from MW-heating assisted fluidized bed reactor and performed energy balance modeling to identify temperature distribution between the gas and the solid. Two correlations were developed to estimate the temperature distribution according to the gas and particles physical properties and bed voidage:

$$T_b = T_s - 166 \, \tau^{-\frac{185}{T_s}} \tag{5.5}$$

$$T_b = 0.54 \, \frac{(1-\varepsilon)\rho_p \, C_{p_p}}{\varepsilon\rho_g \, C_{p_g} + (1-\varepsilon)\rho_p \, C_{p_p}} T_s + 834 \, \frac{\varepsilon\rho_g \, C_{p_g}}{\varepsilon\rho_g \, C_{p_g} + (1-\varepsilon)\rho_p \, C_{p_p}} T_g \tag{5.6}$$

5.3.2 Model formulation

5.3.2.1 Energy balance around single particle in MW-FBR

We conducted an energy balance around a single particle to define the temperature profile as shown in Figure 5.1 with the following assumptions:

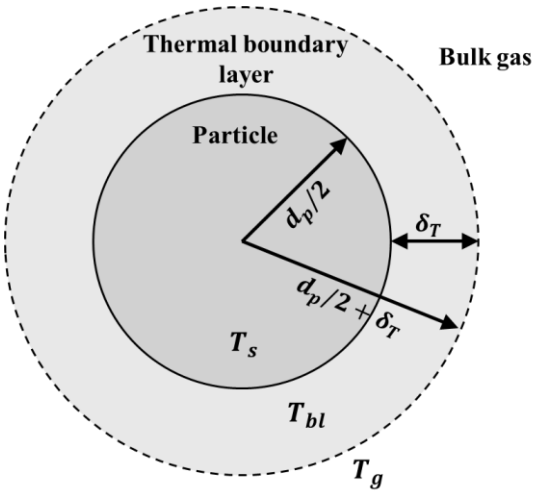

Figure 5.1 Temperature distribution around single particle in MW-FBR.

- Steady-state heat transfers from the hot particle to the cold gas.
- We neglected the internal heat generation inside the particle due to MW power absorption and directly implemented the steady-state particle surface temperature (T_s) that was measured experimentally.
- Heat flux is only in the radial direction (r) from the surface of the particle to the surrounding gas.
- The thermal boundary layer around the particle is stagnant, and the heat transfer is dominated by conduction, while convective heat transfer is negligible within the boundary layer.
- Heat consumption by the endothermic CH_4 pyrolysis was neglected.
- The gas physical properties in the boundary layer are constant and evaluated at an average boundary layer temperature ($T_{bl_{ave}}$).
- The gas physical properties are a function of the gas mixture composition. Therefore, the gas mixture properties do change with bed height.

Applying the stated assumptions above, the energy balance around a single fluidized particle is:

$$\frac{1}{r^2}\frac{d}{dr}\left(r^2 k_f \frac{dT}{dr}\right) = 0 \tag{5.7}$$

The differential equation is solved with boundary conditions that $T(r)= T_s$ at $r = \frac{d_p}{2}$, and $T(r) = T_g$ at $r = \frac{d_p}{2} + \delta_T$. Which leads to the following expression for the temperature profile in the boundary layer:

$$T_{bl}(r) = T_s + (T_g - T_s)\frac{\frac{1}{r} - \frac{1}{d_p/2}}{\frac{1}{d_p/2 + \delta_T} - \frac{1}{d_p/2}} \tag{5.8}$$

We evaluated the thermal boundary layer thickness (δ_T) around the particle by equating the conduction flux through the boundary layer to the convective heat flux into the bulk gas, as such:

$$-k_f \frac{dT}{dr}\Big|_{r=\frac{d_p}{2}} = h(T_s - T_g) \tag{5.9}$$

Which leads to

$$\delta_T = \frac{\frac{d_p}{2}\, k_f}{h\frac{d_p}{2} - k_f} \tag{5.10}$$

The heat transfer coefficient (h) is estimated by Ranz-Marshall correlation for a single sphere [85]:

$$Nu = \frac{h\, d_p}{k_g} = 2 + 0.6\, Re^{\frac{1}{2}}\, pr^{\frac{1}{3}} \tag{5.11}$$

5.3.2.2 Rate equation and mass balance

We assumed that the reactor operates under steady-state conditions, as temperature and gas species concentrations remained stable over time at the experimental conditions. We neglected radial gradients in gas concentration, temperature, and reaction rate. We treated the gas mixture as an ideal gas. The gaseous product distribution mainly consists of H_2 and unreacted CH_4; therefore, we modeled CH_4 decomposition as a single-step reaction according to:

$$CH_4 \rightarrow C + 2H_2 \tag{5.12}$$

Based on the local temperature distribution around hot particles in MW-FBR, we represented CH_4 pyrolysis to take place according to the temperature profile around the particle shown in Figure 5.1. Bulk gas reaction occurs at the bulk gas temperature T_g. Thermal boundary layer reaction occurs within the thermal boundary layer around the particles at $T_{bl}(r)$ Near-surface reaction occurs directly near the particle surface at T_s. The one-dimensional gradient conversion of CH_4 across the reactor length:

$$\frac{dx_{CH_4}}{dz} = \frac{1}{u_g}\left(\frac{1-x_{CH_4}}{1+\varepsilon_v x_{CH_4}}\right)\left[k_g\varepsilon_g + k_{bl}(1-\varepsilon)\frac{\left(\frac{d_p}{2}+\delta_T\right)^3 - (\frac{d_p}{2})^3}{(\frac{d_p}{2})^3} + k_s''\frac{6(1-\varepsilon)}{d_p}\right] \quad (5.13)$$

The derivation of the expression in Eq. (5.13) is provided in Section B1 of Appendix B. The reaction rate constant of CH_4 consumption in the gas bulk (k_g) and at the near-surface (k_s'') are defined by:

$$k_g = k_o Exp(\frac{-E_A}{R}\left(\frac{1}{T_g}-\frac{1}{T_{ref}}\right)) \quad (5.14)$$

$$k_s'' = k_o'' Exp(\frac{-E_A}{R}\left(\frac{1}{T_s}-\frac{1}{T_{ref}}\right)) \quad (5.15)$$

We represented the kinetic constant in the boundary layer by a volume-averaged expression integrated over the volume of the thermal boundary layer at the temperature, $T_{bl}(r)$, as such:

$$k_{bl} = \frac{\int_V k_{bl}(T(r))dV}{\int_V dV} = \frac{\int_{\frac{d_p}{2}}^{\frac{d_p}{2}+\delta_T} k_o Exp(\frac{-E_A}{R}(\frac{1}{T_{bl}(r)}-\frac{1}{T_{ref}})\, 4\pi r^2\, dr}{\frac{4}{3}\pi\left(\left(\frac{d_p}{2}+\delta_T\right)^3-\left(\frac{d_p}{2}\right)^3\right)} \quad (5.16)$$

We defined the reference temperature for an irreversible first-order reaction by [115]:

$$T_{ref} = \frac{\sum_{i=1}^{N}\left[\left(1-x_{CH_4,i}\right)\ln\left(1-x_{CH_4,i}\right)\right]^2}{\sum_{i=1}^{N}\left[\left(1-x_{CH_4,i}\right)\ln\left(1-x_{CH_4,i}\right)\right]^2 \Big/ T_i} \quad (5.17)$$

In CH-FBR, the gas phase and solid phase are at the same temperature. Hence, the one-dimensional CH_4 conversion over the length z:

$$\frac{dx_{CH_4}}{dz} = \frac{k\,\varepsilon}{u_g}\left(\frac{1 - x_{CH_4}}{1 + \varepsilon_v x_{CH_4}}\right) \tag{5.18}$$

Where k is the rate constant as defined in Eq. (5.14). In CH-FBR, the gas temperature in the freeboard is at a high temperature (>950 °C) enough for possible CH_4 conversion in the freeboard. Therefore, we treated the reactor as two zones: dense bed and freeboard. As such:

Dense bed:

$$T_g = constant$$

Freeboard:

$$T_{g(z)} = az^4 + bz^3 + cz^2 + dz + e$$
$$\varepsilon = 1 \tag{5.19}$$

The temperature dependency on the axial position, Eq. (5.19), is expressed by a 4th-order polynomial function and is employed as an input. Temperature measurement in CH-FBR and the fitting parameters of the temperature distribution of Eq. (5.19) are provided in Section B.2 of Appendix B.

Kinetic expressions for CH_4 conversion were combined and solved numerically. Nonlinear regression analysis (MATLAB, ODE 45-4th order Runge–Kutta method and least-square curve fitting ‘‘lsqcurvefit” routine) was used to evaluate the kinetic parameters. The regression algorithm constrained the estimated rate constants and activation energies to remain positive, consistent with physical principles. The optimization criteria minimized the sum of squared differences between the experimentally measured and calculated CH_4 conversion values.

5.4 Results

5.4.1 Experimental results

Figure 5.2 shows the temperature distribution in MW-FBR and the corresponding bulk temperature and gas temperature variation with the measured solid temperature. The thermocouple measurement inside the bed provided the average bulk temperature, reflecting contributions from

both the solid and gas phases. MW heating selectively heated the solid particles, while the gas was heated through contact with the solids, as it remained MW-transparent. On average, the solid temperature exceeded the gas temperature by ~200 °C, and the bulk temperature by ~100 °C. The estimated bulk temperature from Eq. (5.5) and Eq. (5.6) is close to the measured bulk temperature by the thermocouple inside the dense bed. The estimated gas temperature from Eq. (5.5) and Eq. (5.6) is less than the measured temperature above the bed. This is due to heat loss from the gas as it travels between the top of the bed and the thermocouple position. Measurement of the bulk temperature at two radial locations and three axial locations showed that MW-FBR operated in isothermal conditions, as the temperature fluctuation was less than 1% across the multiple measurement points.

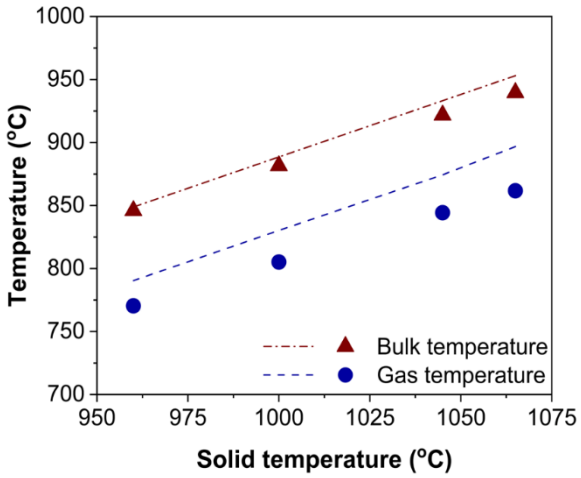

Figure 5.2 Experimental (symbols) and estimated (lines) gas temperature and bulk temperature versus measured solid temperature in MW-FBR

Figure 5.3 shows the impact of temperature and mean residence time on CH_4 conversion in MW-FBR and CH-FBR. CH_4 conversion increased steadily with temperature due to the endothermic nature of CH_4 pyrolysis. Increasing the solid temperature from 960 °C to 1065 °C resulted in an increase in CH_4 conversion from 21% to 74% at a mean residence time of 5 s (Figure 5.3a). Similarly, longer residence times, ranging from 0.5 to 5.0 s, led to higher CH_4 conversions (Figure 5.3b), indicating that the reaction conditions are far from equilibrium and that extended residence

time enhances reaction progression. A similar trend was observed in CH-FBR, where CH_4 conversion increased with both temperature and residence time, as shown in Figure 5.3c and d.

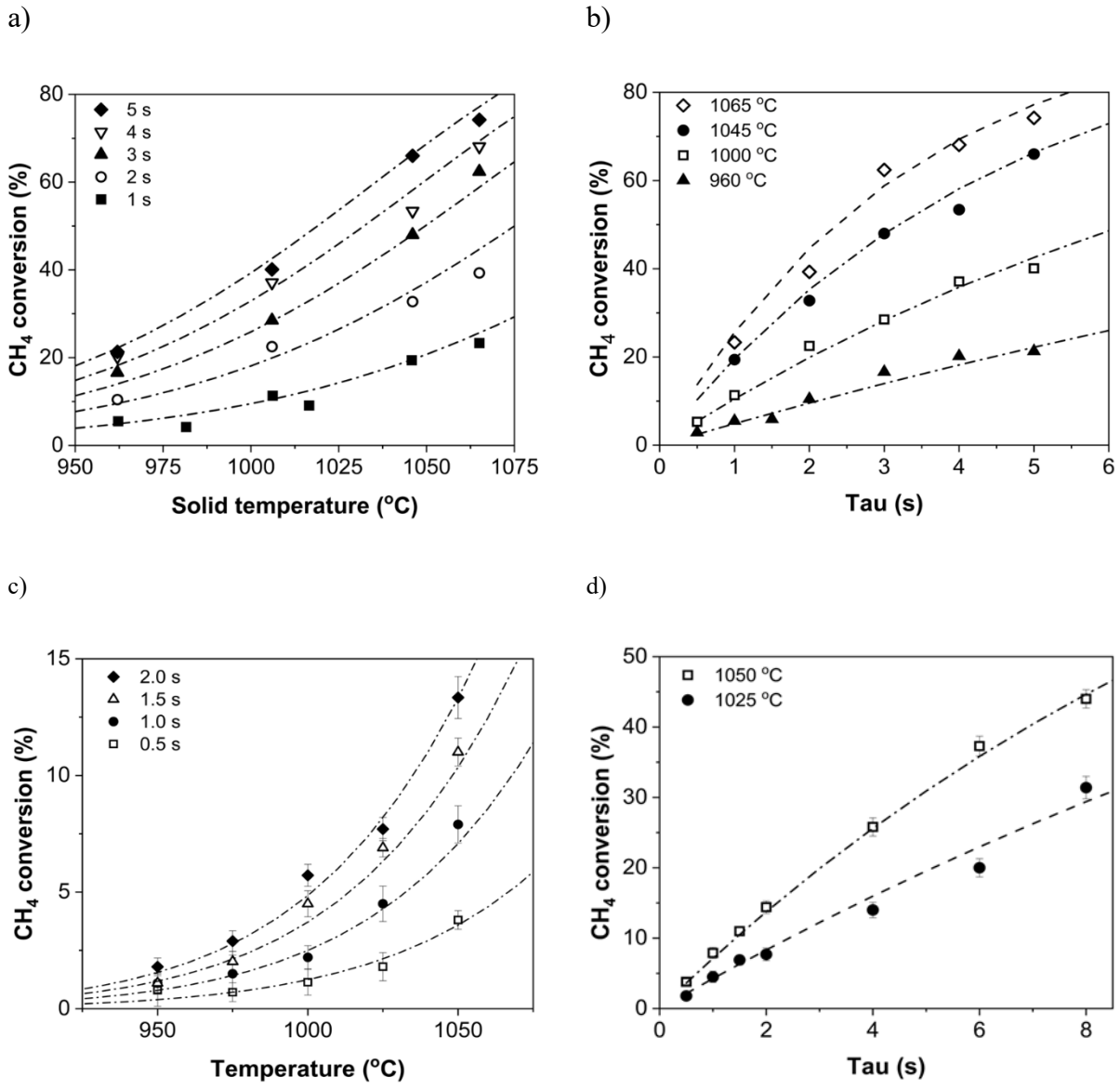

Figure 5.3 variation of CH4 conversion in MW-FBR with a) solid temperature and b) mean residence time; and in CH-FBR with c) temperature and d) mean residence time

5.4.2 Kinetic parameters estimation

We determined the reaction order of CH_4 pyrolysis by varying the inlet CH_4 concentration between 20% and 50% and analyzing the dependence of the reaction rate on the inlet concentration. The logarithmic plot of the reaction rate versus CH_4 concentration yielded a slope close to unity, Figure 5.4. Therefore, a first-order reaction for both MW-FBR and CH-FBR was confirmed, in agreement with previous studies on CH_4 decomposition in conventional heating systems [91,116–118].

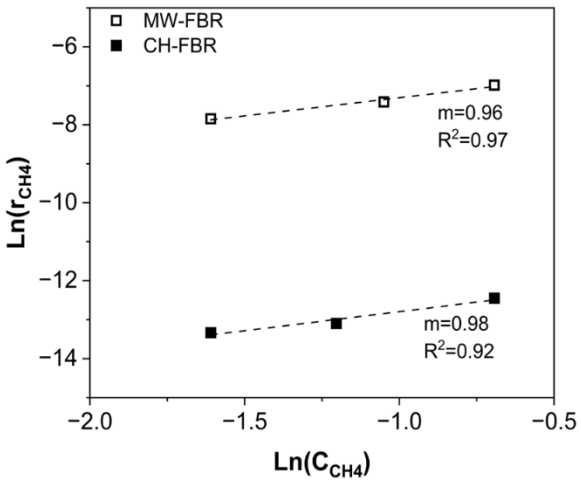

Figure 5.4 Variation of the rate of CH_4 pyrolysis in relation to the change in inlet CH_4 concentration

The estimated kinetic parameters for MW-FBR and CH-FBR are presented in

Table 5.2, with the corresponding parity plots for experimental and predicted CH_4 conversion shown in

a) b)

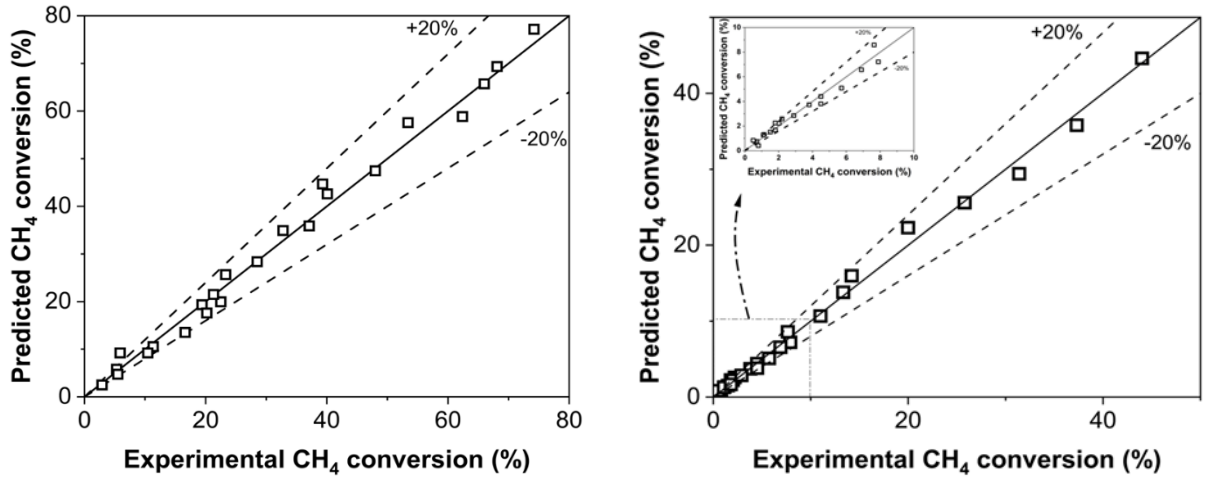

Figure 5.5. Most estimated values were predicted with a deviation of less than 20%, indicating good agreement between model predictions and experimental data. The activation energy for CH_4 pyrolysis in MW-FBR was estimated at 288 kJ/mol, while for CH-FBR, it was 310 kJ/mol.

For global CH4 thermal pyrolysis, the literature reports activation energy in the range of 230 kJ/mol-370 kJ/mol for reaction conducted in the temperature range 973 K- 1450 K [119–121]. Higher reaction temperature above 2000 K with rapid CH4 decomposition reports higher activation energy in the range of 356 kJ/mol–400 kJ/mol [122,123]. Therefore, the activation energy estimated in MW-FBR and CH-FBR falls within the range of activation energy reported in the literature across the relevant temperature range employed in our study. The lower activation energy in MW-FBR as compared to CH-FBR suggests a thermal enhancement effect from MW heating, which may be attributed to localized hotspots in the fluidized bed that locally increase the particle temperature, thereby accelerating reaction rates without a corresponding increase in overall measured temperature.

Table 5.2 Experimental conditions for CH4 thermal pyrolysis in MW-FBR and CH-FBR

Parameter	**MW-FBR**	**CH-FBR**
E_a(kJ/mol)	288 ± 8.6	310 ± 12
k_{ref} (1/s)	$(21.3 \pm 0.4) \times 10^{-2}$	$(6.27 \pm 0.1) \times 10^{-2}$
T_{ref} (°C)	1037	1028
R^2	0.96	0.98
Sum of squares	1.1×10^{-2}	3.3×10^{-4}
Correlation between parameters	2.3×10^{-2}	1.4×10^{-2}

a) b)

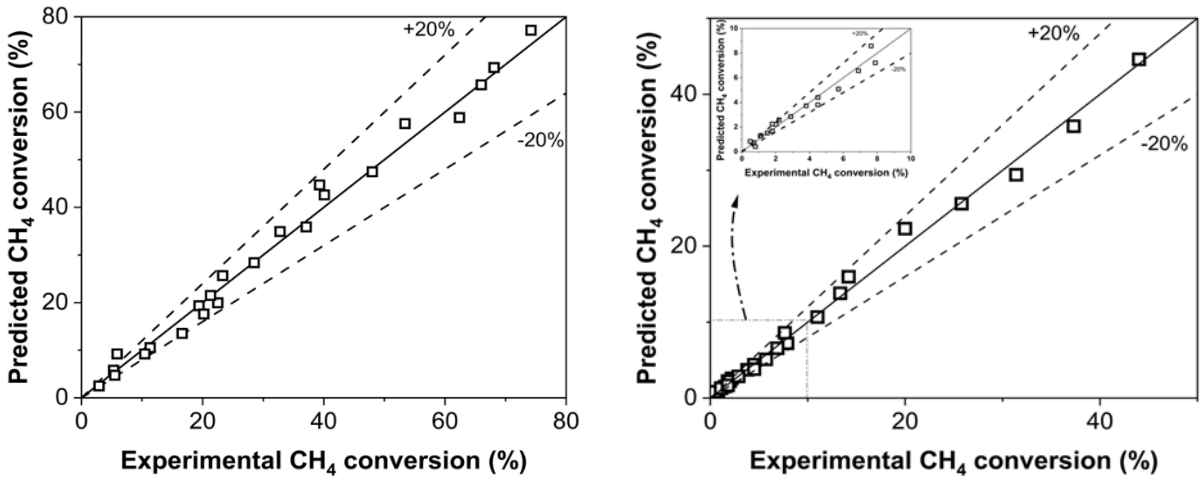

Figure 5.5 Parity plots for experimental and predicted CH_4 conversion in a) MW-FBR, and b) CH-FBR

In several kinetic studies involving MW heating, researchers commonly used the bulk temperature (T_b) to estimate reaction kinetics [124]. As a result, they frequently reported lower apparent activation energies for reactions under MW heating compared to conventional heating systems. These differences were often linked to assumed non-thermal effects of MW heating. However, in many cases, the possibility of underestimating the actual reaction temperature was not considered. Since temperature measurements, typically conducted by thermocouples, reflect T_b rather than the MW absorbent temperature (T_s), the resulting kinetic parameters may be inaccurate. Especially, if the chemical reaction takes place on the MW absorbent. This discrepancy is more significant in reactions with high activation energy, such as CH_4 pyrolysis, where a small temperature difference strongly influences the conversion and, accordingly, the estimated activation energy.

Figure 5.6 illustrates the variation in estimated activation energy based on different temperature representations in MW-FBR, comparing it to the base activation energy obtained from CH-FBR. The estimated activation energy based on bulk temperature T_b and Eq. (5.18) is only 205 kJ/mol, approximately 34% lower than the reference activation energy in CH-FBR at 310 kJ/mol. A better assessment was achieved by considering T_s. This approach resulted in an activation energy of 271 kJ/mol, reducing the difference between MW-FBR and CH-FBR to 13%. This indicates that the localized particles' temperature plays the dominant role in CH_4 conversion in MW-FBR. The

estimation of activation energy based on Eq. (5.18) does not account for the temperature gradient in the thermal boundary layer surrounding the particles, which is at a temperature high enough to advance CH_4 conversion.

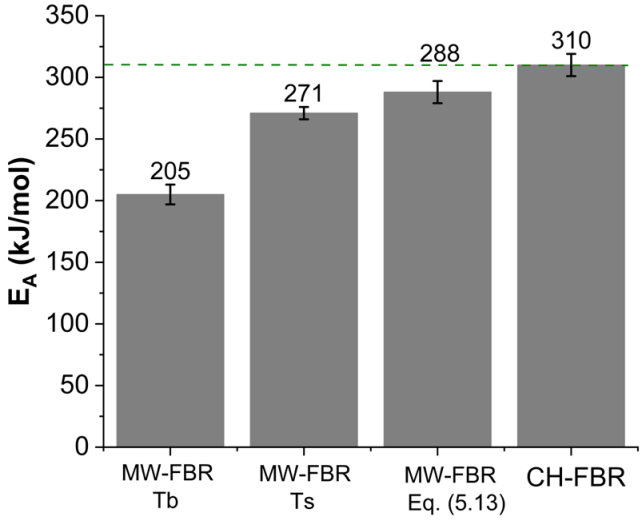

Figure 5.6 Effect of temperature on estimated activation energy in MW-FBR with reference CH-FBR

Incorporation of the thermal boundary layer, Eq. (5.13), in the reactor model accounts for the radial temperature distribution around the particles. The estimated activation energy was 288 kJ/mol, reducing the difference with base CH-FBR to 7%. Therefore, properly accounting for the reaction environment, including both the solid surface and the surrounding boundary layer, improves the accuracy of the activation energy estimation, with the difference between MW-FBR and reference CH-FBR is reduced as temperature representation becomes more detailed.

The difference in the estimated activation energy between MW-FBR (Eq. 13) and CH-FBR might be attributed to localized microscale hotspots, which cannot be directly measured with the experimental techniques employed in this study.

To estimate the influence of these unmeasured hotspots on CH_4 pyrolysis, we introduced a thermal correction factor (β) to adjust the measured solid temperature and approximate the effective temperature in MW-FBR. This approach takes advantage of the activation energy difference

observed between CH-FBR and MW-FBR by using it as a basis to quantify the thermal impact of the localized hotspots. We approximate the effective temperature (T_{eff}) in MW-FBR by Eq. (5.20):

$$T_{eff} = \beta T_s \tag{5.20}$$

In the MW-FBR reactor model (Section 5.3.2), we replaced all instances of the experimentally measured solid temperature T_s with the effective temperature T_{eff}. We employed in the model equations the kinetic parameters obtained from the reference CH-FBR,

Table 5.2. Then, we optimized β through nonlinear least-squares regression (MATLAB function lsqnonlin) by minimizing the residuals between the experimentally measured and model-predicted CH_4 conversion profiles obtained from MW-FBR, Figure 5.3a and b.

The optimized value of β was 1.05 ± 0.004, indicating that the effective solid temperature in MW-FBR is, on average, 5% higher than the pyrometer-measured temperature. Using this correction, the experimental CH_4 conversion in MW-FBR was predicted with the kinetic parameters obtained from CH-FBR at an R^2 value of 0.95. Therefore, our results suggest that, under the experimental conditions of this study, the effect of hotspots in MW-FBR is equivalent to an approximate 5% increase in the measured macroscale solid temperature.

5.4.3 Hotspots origin and thermal contribution in MW-FBR

Particle-particle interactions occur frequently within fluidized beds, leading to contact between particles [125,126]. At these particle contacts, the electromagnetic field intensifies, causing the electric current to concentrate locally [89,127,128]. Due to the small contact area between adjacent particles, current flow encounters high electrical resistance at these points, resulting in elevated current densities [89]. Consequently, these localized regions experience intense heating, forming microscale hotspots. The presence of these localized hotspots is expected to influence the reaction kinetics by locally increasing temperatures beyond those measured experimentally at the macroscale.

We studied the effect of hotspot formation and its plausible temperature range by means of numerical simulation via COMSOL Multiphysics. Simulation details, including assumptions, governing equations, simulated geometries, boundary conditions, and validation, are provided in Section B.3 of Appendix B.

We examined particle-level interactions by modeling a single particle and a pair of particles in contact to observe the effect of the particles' contact on MW power dissipation density and identify hotspots temperature relative to a single particle temperature. We assume that the particles in MW-FBR behave as a collection of independent MW absorbing particles so that MW absorption within a particle does not affect other neighboring particles and that the MW is dissipated uniformly inside the bed.

Figure 5.7 shows the effect of particle contact on power dissipation density. Figure 5.8 shows radial profiles of current density and power dissipation density in an isolated particle and a pair of particles in contact. The induced current of a single particle is linearly spread over the volume of the particle. The current density at the surface is 10^5 A/m^2 and drops by an order of magnitude to 10^4 A/m^2 at the center of the particles, Figure 5.8a. Similarly, the power dissipation density of a single particle is highest at the surface of the particle at 10^7 W/m^3 and drops by three orders of magnitude to 10^4 W/m^3 at the center of the particles, Figure 5.8b. Particles' contact influences electromagnetic interactions. At the point of contact between two particles (Figure 5.7a, Figure 5.8c and d), the induced current density increases by two orders of magnitude (10^7 A/m^2) compared to a single particle, Figure 5.8c. This concentrated current flow results from increased electrical resistance at the reduced contact area. Consequently, power dissipation density at the particle contact region is enhanced by two orders of magnitude (10^9 W/m^3) compared to an isolated particle, Figure 5.7a and Figure 5.8d. As a result of the concentrated power dissipation at the particle contact point, the temperature of contacting particles is approximately 180 ^{o}C higher than that of an isolated particle, as shown in Figure 5.7b. Despite the power dissipation being concentrated at the contact point, the temperature within each particle in contact is uniform, as the Biot number is small and less than 0.1, Figure 5.7b. Therefore, hotspots in MW-FBR are particles in contact rather than local hotspots on the particle's surface. For larger particles, the hotspot can be localized at the contact area. For instance, Figure 5.7c shows a pair of 2 mm particles in contact where a surface hotspot forms at the point of contact, with a temperature difference of approximately 220 °C relative to the surrounding surface. Larger particles are less effective in heat dissipation due to increased thermal diffusion path length. As a result, the concentrated power dissipation at the contact generates a hotspot which does not fully equilibrate thermally across the particle volume, and hence, a visible temperature gradient occurs at the surface near the contact region.

a)

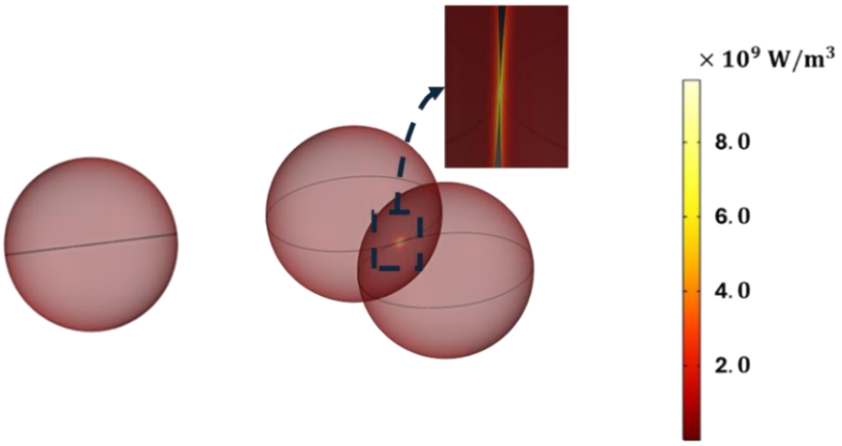

b)

c)

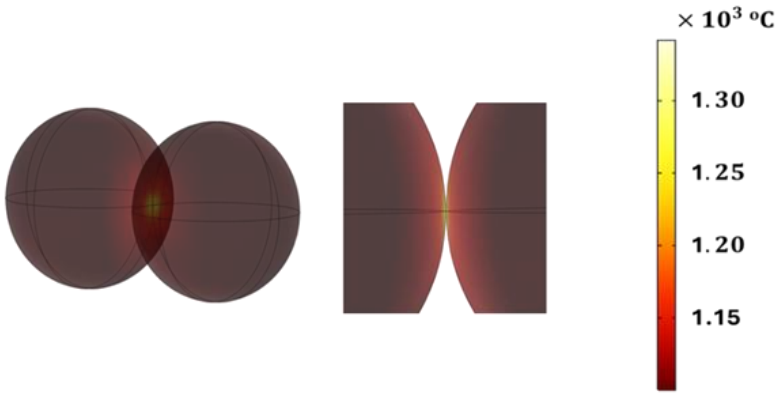

Figure 5.7 Effect of particle contact in MW-FBR on a) power dissipation, b) temperature; and c) surface hotspot formation at the contact of 2 mm particles.

a)

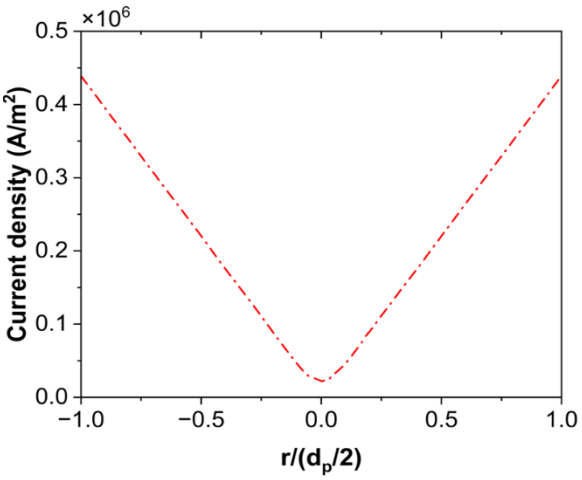

b)

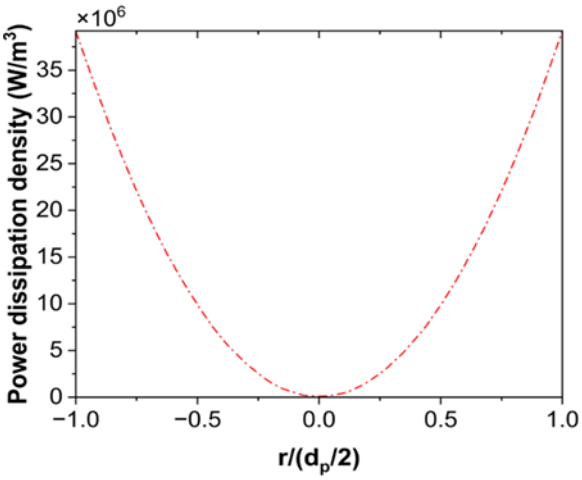

c)

d)

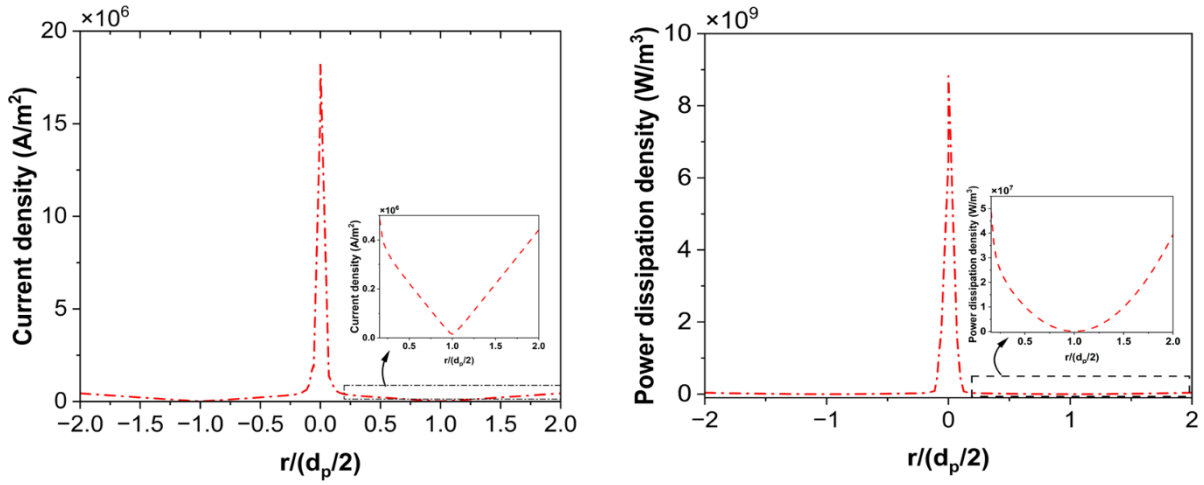

Figure 5.8 Radial profiles of a) current density distribution for two contacting particles, b) power dissipation density distribution for two contacting particles, c) current density distribution for a single particle, and d) power dissipation density distribution for a single particle.

The effective bed temperature is a function of the hotspot temperature and the surface area of the hotspots(fraction of particles in contact). We estimated the effective bed temperature (T_{eff}) by Eq. (5.21):

$$T_{eff} = \alpha_{hs} T_{hs} + (1 - \alpha_{hs}) T_s \tag{5.21}$$

Where T_{hs} is the temperature of contacting particles, representing the localized hotspot temperature. T_s refers to the temperature of an isolated single particle. α_{hs} is the surface fraction of particles at T_{hs}. To estimate α_{hs}, we adopted a coordination-number-based approach to represent the time-averaged interparticle contact within the fluidized bed [129]. The coordination number represents the average number of direct contacts or interactions that a typical particle has with its neighboring particles. We assumed individual particles in the bed either have a single contact or no contact with neighboring particles, and as such, α_{hs} = CN. We adopted the correlation proposed by Hou et al. to estimate the coordination number based on the solid volume fraction (ε_p) [130]:

$$CN = 4.87 \times 10^{-8} \frac{1 - \left(1 - \varepsilon_p\right)^{2.8}}{\left(1 - \varepsilon_p\right)^{11.6}} \tag{5.22}$$

To estimate ε_p in Eq. (5.22), we assumed the emulsion phase remains at a minimum fluidization state according to the simple two-phase model [131]. We estimated ε_{mf} experimentally as detailed in Section B.4 of Appendix B. We identified ε_p at minimum fluidization condition in the range of 0.53-0.51 based on repeated measurements. Accordingly, α_{hs} is 0.14-0.26.

Figure 5.9a shows the variations in T_{hs} for different T_s. It also shows estimated T_{eff} at the range of α_{hs} and, T_{eff} at β=1.05 obtained from comparing E_a from CH-FBR and MW-FBR. Figure 5.9b shows the variation in β at different α_{hs}. T_{hs} remains on average 180 °C higher than T_s. The results obtained from the numerical simulation estimate β between 1.02 and 1.06. Corresponding to the value from the activation energy comparison at 1.05. Therefore, the experimental findings and the numerical simulation show that hotspots contribute to about a 3%-6% increase in the measured temperature. Our study highlights the MW thermal effects of microscale hotspots in MW-FBR. While another form of hotspot can occur at the macroscale, caused by non-uniform electromagnetic field distribution and resulting in uneven power dissipation [132]. Macroscale hotspots are not relevant in our system. The solid phase exhibited nearly isothermal conditions due to the small reactor size, as confirmed by measurements at multiple locations (Section 5.4.1). Therefore, the MW thermal effect in this study is attributed solely to microscale hotspots. In larger MW reactors, both microscale and macroscale hotspots may contribute to reactor performance, signifying overall MW thermal effect.

a)

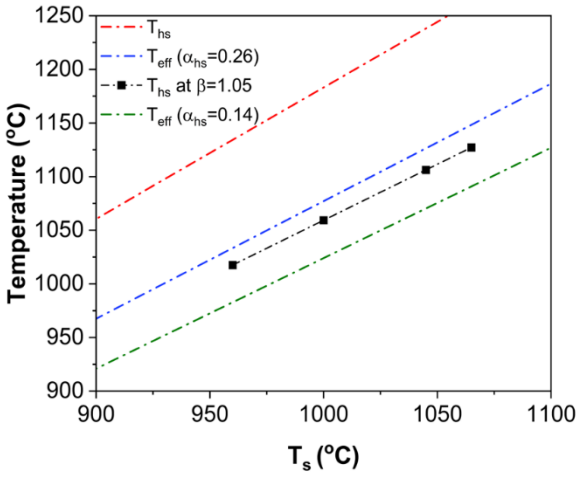

b)

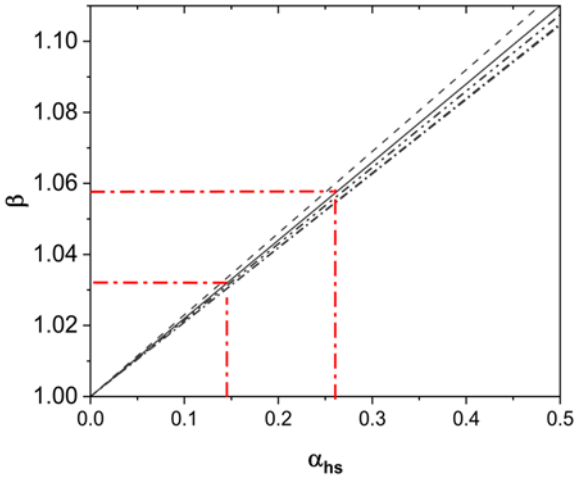

Figure 5.9 Temperature variation from numerical simulation of MW-FBR; a) variation of T_{hs} and T_{eff} at different T_s, b) variation of β at different α_{hs}

5.4.4 CH_4 pyrolysis in MW-FBR

Figure 5.10 shows the predicted CH_4 conversion in MW-FBR as a function of both solid temperature and bulk temperature for various residence times. Figure 5.10 is useful to establish the prediction of the temperature and residence time requirements for operating MW-FBR at a targeted CH_4 conversion. The figure suggests that a temperature above 1050 °C (solid-based) is required for complete conversion of CH_4. The results of MW-FBR are comparable to those reported for CH_4 catalytic pyrolysis in molten metals, where complete conversion of CH_4 is predicted at a minimum of 1080 °C [79].

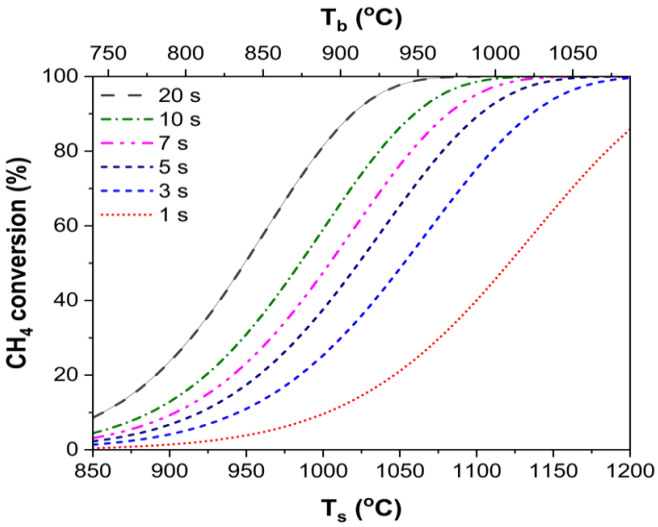

Figure 5.10 Predicted CH_4 conversion in MW-FBR as a function of temperature at different residence times from 1.0 s to 20 s

5.5 Conclusion

We investigated the kinetics of CH_4 pyrolysis in a MW heating-assisted fluidized bed reactor (MW-FBR) and a conventional heating-assisted fluidized bed reactor (CH-FBR). Experiments were

conducted at temperatures ranging from 950 °C to 1065 °C and residence times between 0.5 s and 8.0 s. We found experimentally that CH_4 conversion was significantly higher in MW-FBR compared to CH-FBR. We estimated the global activation energy under both heating conditions. The activation energy was determined as 288 kJ/mol for MW-FBR and 310 kJ/mol for CH-FBR. We demonstrated the importance of accurate temperature representation in MW-FBR, as the difference between the activation energy in MW-FBR and CH-FBR is reduced from 34% when only considering the bulk temperature to 7% when considering a more detailed model that accounts directly for the solid temperature and includes the temperature distribution around the hot particles. The observed increase in CH_4 conversion and lower activation energy in MW-FBR was attributed to MW thermal effect in the form of localized hotspots.

We investigated the formation and thermal impact of microscale hotspots in MW-FBR using both experimental and numerical approaches. Experimentally, we compared the activation energies between MW-FBR and base case CH-FBR, we quantified the thermal effect of these hotspots as equivalent to an approximately 5% increase in the effective bed temperature compared to pyrometer measurements. Numerically, we employed COMSOL Multiphysics simulations, which identified that microscale hotspots form due to particle-particle contact. At these contact points, the current density and power dissipation were substantially higher (by two orders of magnitude) compared to isolated particles which resulting in hotspot temperatures approximately 180 °C higher than isolated particles. We adopted a coordination-number-based approach to extend local hotspot temperatures to an overall effective bed temperature. We estimated that the bed temperature is approximately 3–6% higher than that of isolated particles, closely supporting our experimental findings.

Nomenclature

Acronym

CH-FBR	Conventional heating-assisted fluidized bed reactor
CN	Coordination number

SiC	Silicon carbide particles
MW	MW
MW-FBR	MW heating-assisted fluidized bed reactor

Symbols

A_t	Reactor cross-sectional area (m^2)
$C_{CH_{4,0}}$	Inlet concentration of CH_4 (mol/m^3)
C_{CH_4}	Concentration of gas specie i (mol/m^3)
C_{p_p}	Particle heat capacity (J/kg K)
C_{p_g}	Gas heat capacity (J/kg K)
d_p	Particle size (m)
E_a	Activation energy (J/kg K)
H	Dense bed height (m)
h	Gas heat transfer coefficient (W/m^2 K)
k	Rate constant for CH_4 decomposition (1/s)
k_{bl}	Rate constant for CH_4 decomposition in the thermal boundary layer (1/s)
k_g	Rate constant for CH_4 decomposition in the gas phase (1/s)
k_o	Pre-exponential factor for CH_4 decomposition (1/s)
k_{ref}	Rate constant for CH_4 decomposition at reference temperature (1/s)
k_s''	Rate constant for CH_4 decomposition near the solid surface (m/s)

k_f	Gas thermal conductivity (W/m K)
Nu	Nusselt number (-)
n_i	Outlet molar flow rate of gas specie i (mol/s)
$n_{i,o}$	Inlet molar flow rate of gas specie i (mol/s)
n_T	Total molar flow rate of the outlet gas stream (mol/s)
Pr	Prandtl number (-)
Re	Reynolds number (-)
r_{CH_4}	CH_4 reaction rate (mol/s)
T_o	Ambient temperature (K)
T_{eff}	Effective temperature (K)
T_g	Gas temperature (K)
T_{hs}	Hotspot temperature (K)
T_{ref}	Reference temperature (K)
T_s	Particle temperature (K)
T_w	Wall temperature (K)
u_{mf}	Minimum fluidization velocity (m/s)
u_g	Superficial gas velocity (m/s)
v_0	Inlet volumetric flow rate (m^3/s)
V_g	Gas volume (m^3)

V_{bl}	Thermal boundary layer volume (m^3)
x_{CH_4}	Methane conversion (%)
y_i	Molar fraction of gas specie i (-)

Greek letters

α_{hs}	Surface fraction of hotspot area (-)
β	Thermal correction factor (-)
δ_T	Thickness of thermal boundary layer (m)
ε	Bed average voidage (-)
ε_v	Volumetric expansion factor (-)
ε_g	Gas volume fraction (-)
ε_{bl}	Thermal boundary layer volume fraction (-)
ε_p	Solid volume fraction (-)
μ	Gas Viscosity (Pa.s)
ρ_p	Particle density (kg/m^3)
ρ_g	Gas density (kg/m^3)
τ	Mean residence time (s)

CRediT authorship contribution statement

Abdelrahman I. Hussain: Conceptualization, Methodology, Validation, Investigation, Data curation, Writing – original draft, Writing – review & editing. **Mohammad Monzavi:** Conceptualization, Methodology, Writing - Review & Editing. **Jamal Chaouki:**

Conceptualization, Resources, Writing - Review & Editing, Supervision, Project administration, Funding acquisition.

Acknowledgments

The authors acknowledge TotalEnergies, the Natural Science and Engineering Research Council, Canada (NSERC), and OCP Group for their financial support of this study.

CHAPTER 6 GENERAL DISCUSSION

The main objective of this work was to investigate CH_4 thermal pyrolysis in a MW heating-assisted fluidized bed reactor (MW-FBR) as a novel approach for CO_2-free H_2 production. This objective was motivated by the environmental drawbacks of conventional H_2 production methods, particularly their reliance on fossil fuels as a heat source and the associated high CO_2 emissions.

To achieve this objective, we combined experimental and modeling approaches. The experimental plan focused on evaluating the operational performance of a lab-scale MW-FBR under various operating conditions, including reaction temperature, CH_4 inlet concentration, and mean residence time. Key performance metrics included CH_4 conversion, H_2 selectivity, and pyrolytic carbon capture efficiency. We also identified heating behavior, temperature distribution, carbon characteristics, and operational stability. In addition, we determined kinetic parameters of CH_4 thermal pyrolysis and identified effects specific to MW heating on the process. Reference experiments were first conducted in a conventionally heated fluidized bed reactor (CH-FBR) to establish baseline behavior. The results from CH-FBR were compared with MW-FBR results to identify the effects of MW heating.

We designed and constructed a lab-scale MW-FBR experimental setup for this work. The main concerns in its development were MW leakage, gas leakage, arcing inside the cavity, and magnetron overheating. These issues were addressed through successive modifications informed by experimental observations during setup development. The MW cavity contained drilled openings for insertion of the quartz reactor and for temperature measurements. Each opening was equipped with hollow stainless-steel cylinders and removable stainless-steel caps, which were designed to act as chokes to prevent MW leakage. Sealing between the caps and the quartz reactor was applied to prevent gas leakage. Edges at the internal connections around the openings were smoothed to prevent charge accumulation and electrical breakdown, leading to arcing. As a result, the MW-FBR operated safely at the high temperatures required for CH_4 pyrolysis over extended periods.

Accurate temperature measurement was the primary challenge in our system. Thermocouples alone were found unsuitable in MW-FBR as they distort and interact with the electromagnetic field and create arcing risks. Moreover, a single-point measurement is inadequate to capture the temperature

gradients in MW-FBR, where gas, solid, and wall temperatures differ significantly. Therefore, we monitored the temperature using a combination of non-contact pyrometers and thermocouples. A profile thermocouple was adapted to capture bulk temperature in the dense bed and the gas in the freeboard. The thermocouple was grounded to prevent arcing. The adapted profile thermocouple had the sensing point 1.5 cm away from the tip to avoid false readings caused by field intensification. Comparative tests indicated that direct tip measurements overestimate the bulk temperature by 40-70 ^{o}C in our system. Two pyrometers were used to measure the surface temperatures of particles and walls. Based on quartz transmission properties, the 2.3 μm pyrometer measured solids through the quartz, while the 8–14 μm pyrometer measured the wall. Calibration for emissivity was carried out using thermocouples under non-fluidized conditions (without fluidizing gas) during cooling. This procedure ensured that the optical signals corresponded to true surface temperatures across the operating range (900-1070 ^{o}C). These adaptations, including thermocouple configuration, dual pyrometry, and calibration procedures, ensured reliable temperature measurement under MW heating. Therefore, despite the challenges in constructing the MW-FBR and measurements, the developed setup provided reliable and reproducible experimental data under varying operating conditions. This allowed a comprehensive evaluation of CH_4 thermal pyrolysis in MW-FBR and clarification of the distinct effects of MW heating.

The main contribution of this work is the demonstration of the viability of CH_4 thermal pyrolysis in MW-FBR as a novel approach for CO_2-free H_2 production. The methods applied and the results obtained highlight original contributions of this study:

First: A novel aspect of this work is the identification of a clear temperature gradient between the reactor wall and the fluidized bed in the MW-FBR. This identification was possible because of the detailed multi-point temperature measurements we implemented which distinguished between solid, gas, wall, and bulk conditions. These findings represent a successful demonstration of the cold-wall reactor concept using MW heating. Cold-wall reactors have been considered desirable in CH_4 thermal pyrolysis to mitigate carbon accumulation on the wall. Nevertheless, previous approaches such as feeding CH_4 through porous walls, embedded resistive heating rods inside the reactor, or falling-film configurations did not provide a practical solution [60–62,73,77]. They failed to prevent clogging or proved too complex to implement. In contrast, MW heating enables a condition where the wall remains colder than the fluidized particles. For instance, in this work, we

measured up to ~250 °C lower wall temperature compared to the fluidized hot particles. CH_4 thermal pyrolysis in MW-FBR benefits directly from this distribution. Carbon deposition preferentially occurs on the hot fluidized particles and limited carbon build-up on the wall. In this way, the temperature gradient between wall and bed emerges as both a distinctive feature of MW-FBR and a practical advantage for CH_4 thermal pyrolysis.

Second, a novel contribution of this work is the exploitation of the temperature gradient between solids and gas in a homogeneous reaction with inert particles. Previous studies demonstrated the benefit of such gradients in heterogeneous catalytic systems, where selective catalytic reactions on hot dielectric catalyst particles were enhanced while undesired secondary reactions in the cooler gas phase were suppressed [15,33,133,134]. Under these conditions, both conversion and selectivity can be improved. In this work, we showed that without a catalyst, the same principle applies in MW heating-assisted CH_4 thermal pyrolysis. Methane pyrolysis has high activation energy and small temperature differences strongly influence reaction rate. With the particles hotter than the surrounding gas, the reaction was concentrated near the solid surface, effectively within the thermal boundary layer. This shifted carbon formation and deposition toward the fluidized solids rather than carbon formation in the bulk gas, improving carbon capture and limiting carbon formation in the freeboard. The ability to utilize such gradients in a purely thermal process extends the significance of MW heating as it demonstrates that temperature distributions can be applied not only in catalytic systems but also in non-catalytic reactions to improve efficiency and product selectivity.

Third, in this work, we identified the origin and estimated the magnitude of hotspots in MW-FBR by combining multi-point temperature measurements, baseline experiments in CH-FBR, and numerical simulations. The analysis showed that particle–particle contacts, where electromagnetic fields and current densities intensify, raised local particle temperatures by hundreds of degrees compared to isolated particles. The integrated methodology provided a framework to quantify hotspot contributions and demonstrated that CH_4 thermal pyrolysis intrinsic kinetics remain unchanged by the heating method.

These original contributions extend beyond the present application in CH_4 pyrolysis and are transferable to the broader field of MW heating-assisted reactors. The identification of stable wall-bed temperature gradients, the demonstration of selective homogeneous reaction control through

solid-gas temperature differences, and the quantification of hotspot effects represent advances in understanding MW interactions that are not limited to CH_4 thermal pyrolysis. They provide insights into how MW heating can be utilized in other applications to control reaction environments and product distributions in gas-solid multiphase systems.

In the broader context of hydrogen production, MW heating-assisted CH_4 thermal pyrolysis represents an attractive pathway relative to established methods such as steam CH_4 reforming (SMR) and to emerging alternatives like solar pyrolysis, plasma pyrolysis, and electrolysis. To date, H_2 production is dominated by SMR, which releases ~9-12 kg of CO_2 per kg H_2 produced [3,7,65]. CH_4 pyrolysis directly splits CH_4 into H_2 and solid carbon with no CO_2 emissions. Unlike SMR, it avoids the water–gas shift and CO_2 separation steps, producing carbon byproduct that can be stored or utilized. When powered with renewable electricity, MW heating-assisted CH_4 pyrolysis eliminates direct emissions. It can also achieve carbon-negative H_2 when biogas is used as the feed. In this manner, biogenic carbon is removed from the atmosphere in solid form. Moreover, CH_4 thermal pyrolysis does not require water as a feedstock, unlike electrolysis, which consumes about 9-10 liters of water per kilogram H_2 [139]. The avoidance of water use is crucial given that many regions with high renewable energy potential face water scarcity. These attributes make MW heating-assisted CH_4 thermal pyrolysis relevant with high potential in the future H_2 economy.

MW delivers energy directly into the reactor volume, heating the solid particles volumetrically rather than through surface conduction, convection, and radiation as in conventional reactors. This contactless mode of heating enables high heating rates and easy on-off control of energy input. In this work, we measured heating rates up to 9.0 °C/s and reached solid temperature above 1050 °C in two minutes. Therefore, in practical terms, MW heating-assisted reactors can be throttled quickly to match intermittent renewable power supply. Plasma systems can also deliver fast response and high CH_4 conversions, but they do so at the expense of high energy consumption, arc instability, and electrode degradation. In contrast, MW achieves rapid heating and high conversion without these limitations. Our results demonstrated that “thermal” CH_4 conversion in the MW-FBR, based on bulk temperature (average bed temperature), matches conversion rates reported in catalytic pyrolysis in molten metals and in catalytic pyrolysis using carbonaceous catalysts. This high conversion under non-catalytic conditions, attributed to MW thermal effects (localized hotspots)

enhances reaction rates beyond what is achievable under uniform heating in conventional systems. In this way, MW heating provides both efficient energy transfer and the benefit of thermal effect to enable fast kinetics at relatively moderate bed temperature.

Additionally, MW heating-assisted CH_4 thermal pyrolysis has an advantage in the broader H_2 market because it bridges the gap between current fossil-based H_2 and future clean H_2. It leverages abundant natural gas resources and existing infrastructure while delivering CO_2-free H_2 at the point of use. Any location with a natural gas pipeline can theoretically host MW heating-assisted CH_4 pyrolysis unit for on-site H_2 generation. This approach avoids the costly transport and storage challenges associated with centralized H_2 supply. This is a compelling proposition for scaling up H_2 use in the near term through clean emerging technologies. For instance, solar pyrolysis is constrained by the need for large heliostat fields and daylight operation which limits distributed H_2 production. Centralized H_2 supply requires transportation by new pipelines, cryogenic trucking, or chemical carriers such as ammonia. Transportation can add ~$3-5/kg H_2 to delivery costs in low-demand cases[135]. MW heating-assisted CH_4 pyrolysis therefore represents a pathway for modular, decentralized H_2 production. Small units can meet local demand through the existing gas and electricity networks. In the broader picture, this approach expands H_2 availability (e.g., fueling stations, industry) without large investments in new infrastructure. In this manner, MW heating-assisted CH_4 pyrolysis repurposes the current energy system, natural gas pipelines, and the electricity grid to deliver CO_2-free H_2.

Overall, MW heating-assisted CH_4 thermal pyrolysis stands out in the H_2 landscape because it combines several unique advantages; eliminates CO_2 emissions without requiring CCS, is effective in delivering energy to the reaction zone and obtains high conversion at relatively moderate bed temperature and can be integrated with existing gas infrastructure for on-site production, while offering flexibility to scale H_2 supply as demand grows. These features make MW heating-assisted CH_4 pyrolysis a strong contender in the clean H_2 market, directly addressing barriers of scalability, infrastructure, and reliability.

Nevertheless, cost reduction remains essential for the commercialization of CH_4 thermal pyrolysis. Technoeconomic studies of electrified CH_4 thermal pyrolysis identify natural gas prices, electricity prices, and the value of carbon as the dominant variables affecting production cost and revenue [136,137]. For MW heating-assisted CH_4 pyrolysis, two areas of research and development are

particularly important: improving energy efficiency and advancing carbon co-product utilization. This requires effective management of carbon formation, control of its quality, and alignment with suitable applications and markets.

A key advantage of CH_4 thermal pyrolysis is its favorable energy economics compared to other emerging H_2 production pathways, i.e., water electrolysis and plasma pyrolysis. Breaking CH_4 into H_2 and solid C requires less energy than splitting H_2O into H_2 and O_2. CH_4 pyrolysis requires only ~ 5.2 kWh/kg H_2 (37.7 kJ/mol H_2), about an order of magnitude less than water electrolysis at ~ 40 kWh/kg H_2 (285.8 kJ/mol H_2) [8,138]. Natural Research Council Canada (NRC) estimates total energy requirements in an electrolysis plant at 55-66 kWh/kg H_2 [139]. Plasma pyrolysis consumes less electricity than electrolysis but remains about an order of magnitude above the thermodynamic minimum for CH_4 thermal pyrolysis. Monolith, a company that uses plasma arcs for CH_4 thermal pyrolysis, reports an energy intensity of 25 kWh/kg H_2 [140]. Plasma arcs heat the bulk gas to extremely high temperatures (up to ~10,000 K), creating large sensible heat loads that must be quenched. In addition to energy loss through radiation and excitation of nonreactive species, which keeps energy consumption well above the theoretical minimum despite high CH_4 conversion [141]. In contrast, MW heating-assisted pyrolysis delivers energy volumetrically into the MW-absorbing solid rather than heating the bulk gas to extreme temperatures. As measured in our study, the temperature difference between the gas phase and the solid phase in MW-FBR is up to 200 ºC. This selective energy coupling enables lower specific electricity consumption than plasma pyrolysis, making MW heating more promising from an efficiency standpoint.

In MW heating-assisted reactor, energy efficiency depends on both the electrical efficiency of the MW generator (conversion of electricity to MW power) and the coupling efficiency (fraction of MW power absorbed by the fluidized bed). Magnetron and solid-state generators are best suited for chemical applications due to their suitable operating frequency and cost margins. Magnetrons are the dominant choice in industry as they benefit from decades of development and optimization. They reach ~80% electrical efficiency, are inexpensive, and deliver up to 100 kW (single magnetron). Solid-state generators operate at ~60% electrical efficiency but offer tunable frequency, precise control, and higher reliability, making them attractive for future use. The precise control of solid-state generators is more suited for optimization of coupling efficiency. Current developments seek to enhance their electrical efficiency to match magnetrons' efficiency. The

coupling efficiency depends on optimizing cavity design and impedance matching. It was demonstrated in the literature that coupling efficiency above 90% is feasible [142]. Considering 80 % electrical efficiency, 90% coupling efficiency and minimized heat losses, MW assisted CH_4 thermal pyrolysis can produce H_2 at 7–8 kWh/kg H_2 at the reactor level. This is about 32% and 14% of the energy requirements of plasma pyrolysis and electrolysis, respectively. This efficiency advantage is a primary lever for reducing the production cost of H_2 in MW heating-assisted CH_4 pyrolysis. Continued progress in high-efficiency solid-state MW generators, cavity design, and thermal loss minimization can therefore unlock efficiencies that surpass other methods. This position MW heating as one of the most promising energy-efficient routes for H_2 production.

Another important economic variable of CH_4 thermal pyrolysis is the pyrolytic carbon byproduct which can be sold as a valuable product. CH_4 thermal pyrolysis co-produces solid carbon at ~3:1 mass to H_2. H_2 cost is therefore sensitive to how much carbon is recovered and sold. When pyrolytic carbon is separated and sold, the associated revenue can offset H_2 production costs. Successful MW heating-assisted CH_4 thermal pyrolysis ought to be dual-market technology for H_2 and pyrolytic carbon for economic competitiveness with SMR and other emerging technologies.

Pyrolytic carbon must be efficiently removed from the reaction zone and separated as a final product. In this work, we have demonstrated that combining fluidization and MW heating is an effective technique for carbon collection in the reaction zone by selectively depositing the carbon on the hot fluidized particles. We measured carbon capture efficiency on the solid fluidized particles of up to 90%. This provides flexibility for carbon management in the process. The recovery of carbon in a MW-FBR can occur through different mechanisms. Pyrolytic carbon deposits can gradually detach from the surface of the fluidized particles via attrition, releasing carbon that becomes entrained in the gas stream. This mechanism was observed in our experiments by SEM-EDX analysis of the downstream gas filter. Particles with a size of 1-3 μm were elutriated from the bed and accumulated in the gas filter. In this case, the elutriated pyrolytic carbon can be separated by gas-solid separation methods (e.g., cyclones, filters) combined with staged solid separation [143]. Alternatively, changes in the physical properties of carbon-covered particles such as size and density alter their fluidization behavior and may lead to segregation within the bed. Therefore, carbon recovery is not a limiting factor in MW-FBR but rather an aspect that can be engineered to maintain stable long-term operation.

The quality of the co-produced carbon is central to the economic potential of CH_4 thermal pyrolysis. Established outlets exist for carbon. The market opportunities for different forms of carbon vary in scale and price. For example, carbon black represents the largest market in size, with an annual demand of ~12 million tons and a price range of USD 0.4–2/kg in 2022 [136]. Graphite, valued at USD10-20/kg but has a smaller market (~80,000 tons/year) [136]. Carbon products have diverse applications. Carbon black is used in tires, pigments, and plastics, while graphite is essential in energy storage and metallurgy, with growing demand from lithium-ion battery electrodes. Matching the properties of pyrolytic carbon to these markets allows MW heating-assisted CH_4 pyrolysis to align its co-product with value-driven opportunities and strengthen the overall economics of H_2 production. Moreover, the ability to supply such quality carbon products from a clean H_2 process can displace conventional routes for carbon production such as furnace black production, petroleum-coke graphitization which are all energy and emission intensive.

The type and properties of pyrolytic carbon are governed primarily by processing temperature, with other influencing factors including pressure, reactor surface-to-volume ratio, processing time, and depositing surface properties [144,145]. In this work, we showed that MW heating-assisted pyrolysis produces semi-graphitic carbon. Raman and XPS analysis showed that increasing temperature improves carbon quality by enhancing graphitization. Thus, operating temperature provides a direct handle to alter carbon structure and quality. Further experimental and theoretical studies are needed to control carbon formation in CH_4 thermal pyrolysis under scalable conditions.

A main benefit of MW heating-assisted CH_4 pyrolysis is that pyrolytic carbon deposition enhances the dielectric properties of the bed particles, which in turn broadens the choice of base particles for high-temperature operation. This means MW heating-assisted CH_4 pyrolysis does not necessarily require high-loss materials such as SiC. Cheap, low-loss dielectrics particles like silica sand can become effective MW absorbers once coated with pyrolytic carbon, which progressively enhances their dielectric response and makes them suitable for high-temperature applications.

The same principle points to the possibility of synthesizing core–shell composites, where pyrolytic carbon acts as the conductive shell around a functional core material. Such composites can exhibit enhanced electrical or thermal properties compared to the raw core and will be suitable for applications in batteries, electrodes, catalytic supports, and other advanced functional materials.

For instance, such applications were demonstrated in the literature for carbon-coated $LiFePO_4$, where the conductive carbon shell enabled its use as a high-performance cathode material in lithium-ion batteries [88]. In this manner, MW heating-assisted CH_4 pyrolysis can be directed toward producing not only bulk carbon but an engineered carbon-based composite. This can widen the spectrum of valuable outputs and create additional revenue streams that enhance economic viability and lower the net cost of H_2 production. Further studies should aim to tailor carbon structures for specific end uses and translate these advances into commercial processes.

Overall, MW CH_4 thermal pyrolysis has the potential to play a significant role in the H_2 production landscape as the global efforts aim to decarbonize H_2 production and expand H_2 use. In the near term, it offers a practical bridge by enabling continued use of natural gas resources without the associated CO_2 emissions. This transitional role is important because completely phasing out fossil fuels will take time, and MW heating-assisted CH_4 pyrolysis provides CO_2-free H_2 at potential competitive costs while H_2 markets and infrastructure are still developing.

In the medium term, MW heating-assisted CH_4 pyrolysis may complement electrolysis as a primary clean H_2 pathway. The high demand for H_2 projected in net-zero scenarios suggests that no single technology will dominate; instead, a mix of production routes will be required, with the choice depending on regional resource availability, infrastructure, energy prices, and policy frameworks. Regions rich in renewable power and freshwater resources may favor electrolysis, while areas with abundant natural gas or biogas can deploy MW heating-assisted CH_4 pyrolysis as a cost-effective solution. MW heating-assisted CH_4 pyrolysis is modular and flexible, and small units can meet distributed demand. Larger production volumes can be achieved by operating multiple units in parallel, which enhances system resilience and reduces dependence on centralized plants.

In the long term, the role of MW heating-assisted CH_4 pyrolysis can develop alongside changes in the energy system. Renewable CH_4 feeds such as biogas or synthetic CH_4 would enable carbon-neutral or carbon-negative operation. The solid carbon by-product also represents an opportunity as deployment scales up, new industries for carbon utilization in steel, cement, batteries, and composites can absorb the output, making carbon a valuable resource rather than a liability. Integrating H_2 and carbon materials production can transform MW heating-assisted CH_4 pyrolysis into a multi-product industry that combines clean energy with advanced material supply.

Therefore, MW CH_4 thermal pyrolysis has the potential to become a key pillar of the H_2 economy. It provides a credible transitional solution in the short term, complements electrolysis in the medium term, and can remain relevant in a fully renewable system by coupling to renewable CH_4 and carbon markets. With continued progress in efficiency, reactor scale-up, and carbon management, MW heating-assisted CH_4 pyrolysis would establish a significant role in future clean H_2 production.

CHAPTER 7 CONCLUSION AND RECOMMENDATIONS

This thesis contributed to the domain of climate change mitigation by introducing a novel method for the continuous production of H_2 via CH_4 pyrolysis. This supports the H_2 economy as a carbon-free energy carrier alongside electricity. Specifically, it introduced MW (MW)-assisted CH_4 thermal pyrolysis, a promising low-emission pathway for H_2 production. MW energy, when generated from renewable electricity, eliminates the CO_2 emissions associated with conventional fossil-fuel-based heating methods and, therefore, a CO_2-free pathway for H_2 production is possible.

The work combined MW heating with a fluidized bed reactor (MW-FBR) configuration to enable continuous operation and address reactor clogging challenges. In addition, inert dielectric particles were utilized to perform thermal pyrolysis, thus avoiding catalyst deactivation typically encountered in catalytic pyrolysis. Extensive experiments confirmed the feasibility and effectiveness of MW-assisted CH_4 pyrolysis for H_2 production.

Experiments conducted in an in-house constructed lab-scale MW-FBR demonstrated that MW heating effectively creates high-temperature conditions (>1050 ^oC) favorable for CH_4 decomposition into H_2 and solid carbon. CH_4 conversion levels of 70 % were attainable within the applied experimental conditions. A high-purity H_2 stream exceeding 95% was produced. Additionally, tracking of pyrolytic carbon product indicated that up to 90% of the pyrolytic carbon was captured by the fluidized particles. Raman spectroscopy and XPS analysis showed that the pyrolytic carbon produced possesses a semi-graphitic structure, with higher reaction temperatures promoting a greater degree of graphitization.

The transient performance of the MW-FBR over 18 hours of time-on-stream showed an increase in CH_4 conversion, contrasting with catalytic pyrolysis systems where conversion typically declines due to catalyst deactivation. We measured the dielectric properties and electrical conductivity of the carbon-coated particles and found that the accumulation of pyrolytic carbon on the particles enhanced MW absorption. This improvement in heating efficiency led to an increase in solid temperature over time and, consequently, higher CH_4 conversion.

Despite thorough measurements to assess the temperature distribution in MW-FBR by a combination of thermocouples and pyrometers, the thermal effects induced by MW heating remain

complex. Therefore, to effectively quantify and distinguish the specific contributions of MW heating on CH_4 pyrolysis, we established a baseline comparison. Our study employed a conventional heating-assisted fluidized bed reactor (CH-FBR) as a reference for direct comparison with MW-FBR. The comparative analysis against a CH-FBR clarified the advantages provided by MW-specific thermal effects. These thermal effects included distinctive temperature gradients between gas and solid phases, as well as the formation of localized hotspots. MW-specific phenomena enhanced reactor performance, yielding a ~150% increase in CH_4 conversion and a ~60% improvement in carbon capture efficiency compared to conventional heating. Additionally, MW heating improved the graphitization degree of pyrolytic carbon by approximately 30%.

Kinetic studies determined apparent activation energies of 288 kJ/mol for MW-FBR and 310 kJ/mol for CH-FBR. The lower activation energy observed under MW heating was attributed primarily to the presence of microscale hotspots, generated through particle contact. Numerical simulation identified the hotspots' temperature to be approximately 180 °C higher for contacting particles than the bulk particles' temperatures under the studied conditions.

This research demonstrated that MW-assisted CH_4 pyrolysis is an effective and sustainable method for continuous CO_2-free H_2 production. It offers high CH_4 conversion rates, produces high-purity H_2, and provides a viable approach for efficient carbon management.

Considering the demonstrated potential in this study, the following recommendations are proposed to further enhance and expand the viability of MW-assisted CH_4 pyrolysis:

- Conducting a comprehensive investigation on the control of the properties of the produced pyrolytic carbon. The quality, morphology, and structural properties of pyrolytic carbon influence its commercial value and the viability of the CH_4 pyrolysis process. Various parameters, including reaction temperature, residence time, and deposition surface, impact the structure, purity, and physical characteristics of the pyrolytic carbon and hence, its quality. This is particularly important, given that the economic viability of CH_4 pyrolysis is highly sensitive to the market value of the pyrolytic carbon.
- Performing a comprehensive techno-economic analysis (TEA) of the MW-assisted CH_4 pyrolysis process. One of the primary barriers to the deployment of clean H_2 technologies is the low production cost of H_2 via steam CH_4 reforming (SMR), which remains the industrial benchmark. In this context, TEA is essential to assess the economic viability of

CH_4 pyrolysis in MW-FBR relative to SMR. It allows for the quantification of capital and operational costs, sensitivity to electricity pricing, and potential revenue from carbon byproducts. Moreover, TEA can identify cost-limiting factors, guide research priorities, and support the development of realistic scale-up and implementation strategies for MW pyrolysis technologies.

- Conducting a life cycle assessment (LCA) of the MW heating-assisted CH_4 pyrolysis process. Although H_2 production from CH_4 pyrolysis in an MW-FBR is CO_2-free at the point of generation, a full environmental evaluation must consider upstream emissions associated with natural gas extraction and transport, renewable electricity infrastructure, and equipment fabrication. Additionally, the handling, processing, and potential utilization of the solid carbon byproduct should be assessed. LCA gives a comprehensive framework to quantify the net climate impact and ensure the process delivers meaningful reductions in life cycle emissions consistent with long-term decarbonization goals.
- Investigating the pyrolysis of natural gas, rather than pure CH_4, is recommended to better reflect potential industrial implementation. While CH_4 is commonly used in laboratory-scale studies, commercial H_2 production relies on natural gas, which contains a mixture of components such as CO_2, H_2O, higher hydrocarbons, and sulfur compounds. These additional constituents can influence reaction selectivity, product distribution, and carbon morphology, and may introduce new side reactions. Therefore, extending the current study to natural gas will provide a more realistic assessment of process viability, gas purification needs, and system robustness under industrial conditions.
- Investigate frequency-tunable MW heating to improve energy efficiency in CH_4 thermal pyrolysis. Tuning the MW frequency to match the dielectric properties of both the bed material can significantly enhance energy absorption and conversion efficiency. Improved efficiency would directly reduce the specific electricity demand of the process and has the potential to lower the overall cost of H_2 production.

REFERENCES

[1] International Energy Agency, World Energy Outlook, 2021.

[2] International Energy Outlook Executive Summary, 2017.

[3] IEA, Global Hydrogen Review 2023, OCED Publishing, Paris, 2023. https://doi.org/10.1787/cb2635f6-en.

[4] J. Whitehead, P. Newman, J. Whitehead, K.L. Lim, Striking the right balance: understanding the strategic applications of hydrogen in transitioning to a net zero emissions economy, Sustain. Earth Rev. 6 (2023) 1–10. https://doi.org/10.1186/s42055-022-00049-w.

[5] FCHEA, Hydrogen end uses, (2025). https://fchea.org/learning-center/hydrogen-in-industrial-application/ (accessed March 10, 2025).

[6] A.L. Moghaddam, S. Hejazi, M. Fattahi, M.G. Kibria, M.J. Thomson, R. AlEisa, M.A. Khan, Methane pyrolysis for hydrogen production: navigating the path to a net zero future, Energy Environ. Sci. 18 (2025) 2747–2790. https://doi.org/10.1039/d4ee06191h.

[7] F. Frieden, J. Leker, Future costs of hydrogen: a quantitative review, Sustain. Energy Fuels 8 (2024) 1806–1822. https://doi.org/10.1039/d4se00137k.

[8] S.F. Ahmed, M. Mofijur, S. Nuzhat, N. Rafa, A. Musharrat, S.S. Lam, A. Boretti, Sustainable hydrogen production: Technological advancements and economic analysis, Int. J. Hydrogen Energy 47 (2022) 37227–37255. https://doi.org/10.1016/j.ijhydene.2021.12.029.

[9] G.H. Patel, J. Havukainen, M. Horttanainen, R. Soukka, M. Tuomaala, Climate change performance of hydrogen production based on life cycle assessment, Green Chem. 26 (2024) 992–1006. https://doi.org/10.1039/d3gc02410e.

[10] D.S. Mallapragada, Y. Dvorkin, M.A. Modestino, D. V. Esposito, W.A. Smith, B.M. Hodge, M.P. Harold, V.M. Donnelly, A. Nuz, C. Bloomquist, K. Baker, L.C. Grabow, Y. Yan, N.N. Rajput, R.L. Hartman, E.J. Biddinger, E.S. Aydil, A.D. Taylor, Decarbonization of the chemical industry through electrification: Barriers and opportunities, Joule 7 (2023) 23–41. https://doi.org/10.1016/j.joule.2022.12.008.

[11] I. Eryazici, N. Ramesh, C. Villa, Electrification of the chemical industry—materials

innovations for a lower carbon future, MRS Bull. 46 (2021) 1197–1204. https://doi.org/10.1557/s43577-021-00243-9.

[12] J.L. Barton, Electrification of the chemical industry, Science (80-.). 368 (2020) 1–8. https://doi.org/10.1007/978-3-030-02006-4_301-1.

[13] D.A. Jones, T.P. Lelyveld, S.D. Mavrofidis, S.W. Kingman, N.J. Miles, Microwave heating applications in environmental engineering - A review, Resour. Conserv. Recycl. 34 (2002) 75–90. https://doi.org/10.1016/S0921-3449(01)00088-X.

[14] NASA, The electromagnetic spectrum overview, (2025). https://science.nasa.gov/ems/ (accessed March 12, 2025).

[15] S. Hamzehlouia, J. Shabanian, M. Latifi, J. Chaouki, Effect of microwave heating on the performance of catalytic oxidation of n-butane in a gas-solid fluidized bed reactor, Chem. Eng. Sci. 192 (2018) 1177–1188. https://doi.org/10.1016/j.ces.2018.08.054.

[16] M. Gupta, W.W.L. Eugene, Microwaves and Metals, 2011. https://doi.org/10.1002/9780470822746.

[17] J. Sun, W. Wang, Q. Yue, Review on microwave-matter interaction fundamentals and efficient microwave-associated heating strategies, Materials (Basel). 9 (2016). https://doi.org/10.3390/ma9040231.

[18] A. Amini, M. Latifi, J. Chaouki, Electrification of materials processing via microwave irradiation: A review of mechanism and applications, Appl. Therm. Eng. 193 (2021) 117003.

[19] S.P.A. Anggraini, S. Suprapto, S.R. Juliastuti, M. Mahfud, Optimization of pyrolytic oil production from coconut shells by microwave-assisted pyrolysis using activated carbon as a microwave absorber, Int. J. Renew. Energy Dev. 13 (2024) 145–157. https://doi.org/10.14710/ijred.2024.56287.

[20] M. Samet, A. Kallel, A. Serghei, Maxwell-Wagner-Sillars interfacial polarization in dielectric spectra of composite materials: Scaling laws and applications, J. Compos. Mater. 56 (2022) 3197–3217. https://doi.org/10.1177/00219983221090629.

[21] M. Sakr, S. Liu, A comprehensive review on applications of ohmic heating (OH), Renew. Sustain. Energy Rev. 39 (2014) 262–269. https://doi.org/10.1016/j.rser.2014.07.061.

[22] N. Kaur, A.K. Singh, Ohmic Heating: Concept and Applications—A Review, Crit. Rev. Food Sci. Nutr. 56 (2016) 2338–2351. https://doi.org/10.1080/10408398.2013.835303.

[23] S. Farag, J. Chaouki, A modified microwave thermo-gravimetric-analyzer for kinetic purposes, Appl. Therm. Eng. 75 (2015) 65–72. https://doi.org/10.1016/j.applthermaleng.2014.09.038.

[24] M. Monzavi, Z. Chen, A. Hussain, J. Chaouki, High quality products from microwave catalytic pyrolysis of heavy oil and polyethylene, Appl. Therm. Eng. 230 (2023) 120722. https://doi.org/10.1016/j.applthermaleng.2023.120722.

[25] M. Oghbaei, O. Mirzaee, Microwave versus conventional sintering: A review of fundamentals, advantages and applications, J. Alloys Compd. 494 (2010) 175–189. https://doi.org/10.1016/j.jallcom.2010.01.068.

[26] M. Monzavi, Z. Chen, A. Solouki, J. Chaouki, Microwave-assisted catalytic pyrolysis of paraffin wax, Fuel 320 (2022) 123886. https://doi.org/10.1016/j.fuel.2022.123886.

[27] H. Li, Z. Zhao, C. Xiouras, G.D. Stefanidis, X. Li, X. Gao, Fundamentals and applications of microwave heating to chemicals separation processes, Renew. Sustain. Energy Rev. 114 (2019) 109316. https://doi.org/10.1016/j.rser.2019.109316.

[28] T.M. Alslaibi, I. Abustan, M.A. Ahmad, A.A. Foul, A review: Production of activated carbon from agricultural byproducts via conventional and microwave heating, J. Chem. Technol. Biotechnol. 88 (2013) 1183–1190. https://doi.org/10.1002/jctb.4028.

[29] X. Zhang, C.S.-M. Lee, D.M.P. Mingos, D.O. Hayward, Carbon dioxide reforming of methane with Pt catalysts using microwave dielectric heating, Catal. Letters 88 (2003) 129–139. https://doi.org/10.1023/A:1024049403422.

[30] Y. Ferna, B. Fidalgo, J.J. Pis, J.A. Mene, Biogas to Syngas by Microwave-Assisted Dry Reforming in the Presence of Char, Energy & Fuels (2007) 2066–2071. https://doi.org/10.1021/ef070101j.

[31] L.M. Kustov, A.L. Tarasov, O.P. Tkachenko, G.I. Kapustin, Nickel-Alumina Catalysts in the Reaction of Carbon Dioxide Re-Forming of Methane under Thermal and Microwave Heating, Ind. Eng. Chem. Res. 56 (2017) 13034–13039. https://doi.org/10.1021/acs.iecr.7b01254.

[32] L. Li, H. Wang, X. Jiang, Z. Song, X. Zhao, C. Ma, Microwave-enhanced methane combined reforming by CO2 and H2O into syngas production on biomass-derived char, Fuel 185 (2016) 692–700. https://doi.org/10.1016/j.fuel.2016.07.098.

[33] S. Hamzehlouia, S.A. Jaffer, J. Chaouki, Microwave Heating-Assisted Catalytic Dry Reforming of Methane to Syngas, Sci. Rep. 8 (2018) 1–7. https://doi.org/10.1038/s41598-018-27381-6.

[34] S. Sharifvaghefi, B. Shirani, M. Eic, Y. Zheng, Application of microwave in hydrogen production from methane dry reforming: Comparison between the conventional and microwave-assisted catalytic reforming on improving the energy efficiency, Catalysts 9 (2019) 1–13. https://doi.org/10.3390/catal9070618.

[35] I. Julian, H. Ramirez, J.L. Hueso, R. Mallada, J. Santamaria, Non-oxidative methane conversion in microwave-assisted structured reactors, Chem. Eng. J. (2018). https://doi.org/10.1016/j.cej.2018.08.150.

[36] G. Roussy, E. Marchal, J.M. Thiebaut, A. Kiennemann, G. Maire, C2+selectivity enhancement in oxidative coupling of methane over microwave-irradiated catalysts, Fuel Process. Technol. 50 (1997) 261–274. https://doi.org/10.1016/S0378-3820(96)01070-3.

[37] S. Horikoshi, A. Osawa, S. Sakamoto, N. Serpone, General Control of microwave-generated hot spots . Part V . Mechanisms of hot-spot generation and aggregation of catalyst in a microwave-assisted reaction in toluene catalyzed by Pd-loaded AC particulates, "Applied Catal. A, Gen. 460–461 (2013) 52–60. https://doi.org/10.1016/j.apcata.2013.04.022.

[38] J.A. Menéndez, E.J. Juárez-Pérez, E. Ruisánchez, J.M. Bermúdez, A. Arenillas, Ball lightning plasma and plasma arc formation during the microwave heating of carbons, Carbon N. Y. 49 (2011) 346–349. https://doi.org/10.1016/j.carbon.2010.09.010.

[39] B. Fidalgo, A. Arenillas, J.A. Menéndez, Mixtures of carbon and Ni/Al2O3 as catalysts for the microwave-assisted CO2 reforming of CH4, Fuel Process. Technol. 92 (2011) 1531–1536. https://doi.org/10.1016/j.fuproc.2011.03.015.

[40] J. Hunt, A. Ferrari, A. Lita, M. Crosswhite, B. Ashley, A.E. Stiegman, Microwave-Specific Enhancement of the Carbon − Carbon Dioxide (Boudouard) Reaction, J. Phys. Chem. 117 (2013) 26871−26880. https://doi.org/10.1021/jp4076965.

[41] R. Li, W. Xu, J. Deng, J. Zhou, Coke-Resistant Ni-Co/ZrO2-CaO-Based Microwave Catalyst for Highly Effective Dry Reforming of Methane by Microwave Catalysis, Ind. Eng. Chem. Res. 60 (2021) 17458–17468. https://doi.org/10.1021/acs.iecr.1c03164.

[42] K. Sun, D.M. Ginosar, T. He, Y. Zhang, M. Fan, R. Chen, Progress in Nonoxidative Dehydroaromatization of Methane in the Last 6 Years, Ind. Eng. Chem. Res. 57 (2018) 1768–1789. https://doi.org/10.1021/acs.iecr.7b04707.

[43] Y. Gu, P. Chen, X. Wang, Y. Lyu, W. Liu, X. Liu, Z. Yan, Active Sites and Induction Period of Fe/ZSM-5 Catalyst in Methane Dehydroaromatization, ACS Catal. 11 (2021) 6771–6786. https://doi.org/10.1021/acscatal.1c01467.

[44] D. Kiani, S. Sourav, Y. Tang, J. Baltrusaitis, I.E. Wachs, Methane activation by ZSM-5-supported transition metal centers, Chem. Soc. Rev. 50 (2021) 1251–1268. https://doi.org/10.1039/d0cs01016b.

[45] Y. Deng, X. Bai, V. Abdelsayed, D. Shekhawat, P.D. Muley, S. Karpe, C. Mevawala, D. Bhattacharyya, B. Robinson, A. Caiola, J.B. Powell, A.P. Van Bavel, J. Hu, Microwave-assisted conversion of methane over H- (Fe) -ZSM-5 : Evidence for formation of hot metal sites, Chem. Eng. J. 420 (2021). https://doi.org/10.1016/j.cej.2021.129670.

[46] L.D. Conde, C. Mar, S.L. Suib, Z. Fathi, Frequency Effects in the Catalytic Oligomerization of Methane via Microwave Heating, J. Catal. 332 (2001) 324–332. https://doi.org/10.1006/jcat.2001.3412.

[47] C. Marú, L. Daniel Conde, S.L. Suib, Catalytic Oligomerization of Methane via Microwave Heating, (1999) 4332–4340. https://doi.org/10.1021/jp984671j.

[48] L.D. Conde, C. Marún, S.L. Suib, Oligomerization of methane via microwave heating using Raney nickel catalyst, J. Catal. 218 (2003) 201–208. https://doi.org/10.1016/S0021-9517(03)00083-6.

[49] L.D. Conde, S.L. Suib, Catalyst nature and frequency effects on the oligomerization of methane via microwave heating, J. Phys. Chem. B 107 (2003) 3663–3670. https://doi.org/10.1021/jp022523u.

[50] I.R. Hamdani, A. Ahmad, H.M. Chulliyil, C. Srinivasakannan, A.A. Shoaibi, M.M. Hossain, Thermocatalytic Decomposition of Methane: A Review on Carbon-Based Catalysts, ACS

Omega 8 (2023) 28945–28967. https://doi.org/10.1021/acsomega.3c01936.

[51] N. Sánchez-Bastardo, R. Schlögl, H. Ruland, Methane Pyrolysis for Zero-Emission Hydrogen Production: A Potential Bridge Technology from Fossil Fuels to a Renewable and Sustainable Hydrogen Economy, Ind. Eng. Chem. Res. 60 (2021) 11855–11881. https://doi.org/10.1021/acs.iecr.1c01679.

[52] M.H. Back, Mechanism of the Thermal Decomposition of Methane, ACS Symp. Ser. (1976). https://doi.org/10.1021/bk-1976-0032.ch001.

[53] M.R. Kholghy, A. Veshkini, M.J. Thomson, The core-shell internal nanostructure of soot - A criterion to model soot maturity, Carbon N. Y. 100 (2016) 508–536. https://doi.org/10.1016/j.carbon.2016.01.022.

[54] M. Gautier, V. Rohani, L. Fulcheri, Direct decarbonization of methane by thermal plasma for the production of hydrogen and high value-added carbon black, Int. J. Hydrogen Energy 42 (2017) 28140–28156. https://doi.org/10.1016/j.ijhydene.2017.09.021.

[55] P. Delhaes, Chemical vapor deposition and infiltration processes of carbon materials, Carbon N. Y. 40 (2002) 641–657.

[56] M. Abuseada, C. Wei, R.M. Spearrin, T.S. Fisher, Solar-Thermal Production of Graphitic Carbon and Hydrogen via Methane Decomposition, Energy and Fuels 36 (2022) 3920–3928. https://doi.org/10.1021/acs.energyfuels.1c04405.

[57] Y. Ji, C. Palmer, E.E. Foley, R. Giovine, E. Yoshida, E. Sebti, A.R. Patterson, E. McFarland, R.J. Clément, Valorizing the carbon byproduct of methane pyrolysis in batteries, Carbon N. Y. 204 (2023) 26–35. https://doi.org/10.1016/j.carbon.2022.12.044.

[58] T. Becker, M. Richter, D.W. Agar, Methane pyrolysis: Kinetic studies and mechanical removal of carbon deposits in reactors of different materials, Int. J. Hydrogen Energy 48 (2023) 2112–2129. https://doi.org/10.1016/j.ijhydene.2022.10.069.

[59] J. Prabowo, L. Lai, B. Chivers, D. Burke, A.H. Dinh, L. Ye, Y. Wang, Y. Wang, L. Wei, Y. Chen, Solid carbon co-products from hydrogen production by methane pyrolysis: Current understandings and recent progress, Carbon N. Y. 216 (2024). https://doi.org/10.1016/j.carbon.2023.118507.

[60] B.P. Ennis, Electric reaction technology for fuels processing, US 7563525 B2, 2009.

[61] N. Nesterenko, I.C. Medeiros-Costa, E.B. Clatworthy, H. Cruchade, S. V. Konnov, J.P. Dath, J.P. Gilson, S. Mintova, Methane-to-chemicals: A pathway to decarbonization, Natl. Sci. Rev. 10 (2023) 1–16. https://doi.org/10.1093/nsr/nwad116.

[62] J. Prabowo, L. Lai, B. Chivers, D. Burke, A.H. Dinh, L. Ye, Y. Wang, Y. Wang, L. Wei, Y. Chen, Solid carbon co-products from hydrogen production by methane pyrolysis: Current understandings and recent progress, Carbon N. Y. 216 (2024) 118507. https://doi.org/10.1016/j.carbon.2023.118507.

[63] IEA, The Future of Hydrogen: Seizing today's opportunities, OECD Publishing, Paris, 2019. https://doi.org/10.1787/1e0514c4-en.

[64] S.R. Patlolla, K. Katsu, A. Sharafian, K. Wei, O.E. Herrera, W. Mérida, A review of methane pyrolysis technologies for hydrogen production, Renew. Sustain. Energy Rev. 181 (2023). https://doi.org/10.1016/j.rser.2023.113323.

[65] I.J. Okeke, B.A. Saville, H.L. MacLean, Low carbon hydrogen production in Canada via natural gas pyrolysis, Int. J. Hydrogen Energy 48 (2023) 12581–12599. https://doi.org/10.1016/j.ijhydene.2022.12.169.

[66] C. Gueret, M. Daroux, F. Billaud, Methane pyrolysis: Thermodynamics, Chem. Eng. Sci. 52 (1997) 815–827. https://doi.org/Doi 10.1016/S0009-2509(96)00444-7.

[67] M. Yousefi, S. Donne, Technical challenges for developing thermal methane cracking in small or medium scales to produce pure hydrogen - A review, Int. J. Hydrogen Energy 47 (2022) 699–727. https://doi.org/10.1016/j.ijhydene.2021.10.100.

[68] Z. Dong, B. Li, C. Cui, W. Qian, Y. Jin, F. Wei, Catalytic methane technology for carbon nanotubes and graphene, React. Chem. Eng. 5 (2020) 991–1004. https://doi.org/10.1039/d0re00060d.

[69] H.Y. Wang, A.C. Lua, Deactivation and kinetic studies of unsupported Ni and Ni-Co-Cu alloy catalysts used for hydrogen production by methane decomposition, Chem. Eng. J. 243 (2014) 79–91. https://doi.org/10.1016/j.cej.2013.12.100.

[70] D.P. Serrano, J.Á. Botas, P. Pizarro, G. Gómez, Kinetic and autocatalytic effects during the

hydrogen production by methane decomposition over carbonaceous catalysts, Int. J. Hydrogen Energy 38 (2013) 5671–5683. https://doi.org/10.1016/j.ijhydene.2013.02.112.

[71] M. Nasir Uddin, W.M.A. Wan Daud, H.F. Abbas, Kinetics and deactivation mechanisms of the thermal decomposition of methane in hydrogen and carbon nanofiber Co-production over Ni-supported y zeolite-based catalysts, Energy Convers. Manag. 87 (2014) 796–809. https://doi.org/10.1016/j.enconman.2014.07.072.

[72] T.I. Korányi, M. Németh, A. Beck, A. Horváth, Recent Advances in Methane Pyrolysis: Turquoise Hydrogen with Solid Carbon Production, Energies 15 (2022). https://doi.org/10.3390/en15176342.

[73] E. Ruiz, E.M. Ferruelo, F. Herna, J.A. Rubio, C. Lo, R. Gavela, G. Barrera, C. Rubbia, Experimental analysis of direct thermal methane cracking, Int. J. Hydrogen Energy 6 (2011) 12877–12886. https://doi.org/10.1016/j.ijhydene.2011.07.081.

[74] T. Geißler, A. Abánades, A. Heinzel, K. Mehravaran, G. Müller, R.K. Rathnam, C. Rubbia, Hydrogen production via methane pyrolysis in a liquid metal bubble column reactor with a packed bed, Chem. Eng. J. 299 (2016) 192–200. https://doi.org/10.1016/j.cej.2016.04.066.

[75] N. Rahimi, D. Kang, J. Gelinas, A. Menon, M.J. Gordon, H. Metiu, E.W. Mcfarland, Solid carbon production and recovery from high temperature methane pyrolysis in bubble columns containing molten metals and molten salts, Carbon N. Y. 151 (2019) 181–191. https://doi.org/10.1016/j.carbon.2019.05.041.

[76] M. Msheik, S. Rodat, S. Abanades, Methane cracking for hydrogen production: A review of catalytic and molten media pyrolysis, Energies 14 (2021) 3107. https://doi.org/10.3390/en14113107.

[77] T. Becker, D.W. Agar, Theoretical Studies on a Rotating Film Reactor for Hydrogen Production from Methane, Chem. Ing. Tech. 94 (2022) 1–10. https://doi.org/10.1002/cite.202100183.

[78] A.M. Dunker, S. Kumar, P.A. Mulawa, Production of hydrogen by thermal decomposition of methane in a fluidized-bed reactor - Effects of catalyst, temperature, and residence time, Int. J. Hydrogen Energy 31 (2006) 473–484. https://doi.org/10.1016/j.ijhydene.2005.04.023.

[79] D.C. Upham, V. Agarwal, A. Khechfe, Z.R. Snodgrass, M.J. Gordon, H. Metiu, E.W. McFarland, Catalytic molten metals for the direct conversion of methane to hydrogen and separable carbon, Science (80-.). 358 (2017) 917–921. https://doi.org/10.1126/science.aao5023.

[80] M. Dadsetan, M.F. Khan, M. Salakhi, E.R. Bobicki, M.J. Thomson, CO2-free hydrogen production via microwave-driven methane pyrolysis, Int. J. Hydrogen Energy 48 (2023) 14565–14576. https://doi.org/10.1016/j.ijhydene.2022.12.353.

[81] S. Schneider, S. Bajohr, F. Graf, T. Kolb, State of the Art of Hydrogen Production via Pyrolysis of Natural Gas, ChemBioEng Rev. 7 (2020) 150–158. https://doi.org/10.1002/cben.202000014.

[82] N. Sánchez-Bastardo, R. Schlögl, H. Ruland, Methane Pyrolysis for CO2-Free H2 Production: A Green Process to Overcome Renewable Energies Unsteadiness, Chemie-Ingenieur-Technik 92 (2020) 1596–1609. https://doi.org/10.1002/cite.202000029.

[83] L. Estel, M. Poux, N. Benamara, I. Polaert, Continuous flow-microwave reactor: Where are we?, Chem. Eng. Process. - Process Intensif. 113 (2017) 56–64. https://doi.org/10.1016/j.cep.2016.09.022.

[84] A. Domínguez, B. Fidalgo, Y. Fernández, J.J. Pis, J.A. Menéndez, Microwave-assisted catalytic decomposition of methane over activated carbon for CO2-free hydrogen production, Int. J. Hydrogen Energy 32 (2007) 4792–4799. https://doi.org/10.1016/j.ijhydene.2007.07.041.

[85] D. Kunii, O. Levenspiel, Fluidization Engineering, Second, Butterworth-Heinemann, Boston, 1991. https://doi.org/10.1016/0032-5910(69)80087-2.

[86] D. Geldart, Types of Gas Fhidization, Powder Technol. 7 (1973) 285–292.

[87] M. Latifi, J. Chaouki, A Novel Induction Heating Fluidized Bed Reactor: Its Design and Applications in High Temperature Screening Tests with Solid Feedstocks and Prediction of Defluidization State, AIChE J. 61 (2015) 1507–1523. https://doi.org/10.1002/aic.

[88] S. Aghaee Sarbarze, M. Latifi, M. Rasouli, S. Rousselot, M. Dollé, J. Chaouki, Pulse-assisted fluidization of nanoparticles: Case of lithium iron phosphate material, Can. J. Chem. Eng. 99 (2021) 1824–1835. https://doi.org/10.1002/cjce.24006.

[89] S. Horikoshi, A. Osawa, M. Abe, N. Serpone, On the Generation of Hot-Spots by Microwave Electric and Magnetic Fields and Their Impact on a Microwave-Assisted Heterogeneous Reaction in the Presence of Metallic Pd Nanoparticles on an Activated Carbon Support, J. Phys. Chem. C 115 (2011) 23030–23035. https://doi.org/10.1021/jp2076269.

[90] C. Palmer, M. Tarazkar, M.J. Gordon, H. Metiu, E.W. Mcfarland, Methane pyrolysis in low-cost, alkali-halide molten salts at high temperatures, Sustain. Energy Fuels 5 (2021) 6107–6123. https://doi.org/10.1039/d1se01408k.

[91] B. Parkinson, C.F. Patzschke, D. Nikolis, S. Raman, K. Hellgardt, Molten salt bubble columns for low-carbon hydrogen from CH4 pyrolysis: Mass transfer and carbon formation mechanisms, Chem. Eng. J. 417 (2021) 127407. https://doi.org/10.1016/j.cej.2020.127407.

[92] D. Rovillain, M. Trinquecoste, E. Bruneton, A. Derré, P. David, P. Delhaès, Film boiling chemical vapor infiltration: An experimental study on carbon/carbon composite materials, Carbon N. Y. 39 (2001) 1355–1365. https://doi.org/10.1016/S0008-6223(00)00255-4.

[93] K. Yu, C.C. Hayman, S. Manjunath, W. Fan, I.T. Martin, H.B. Martin, R.M. Sankaran, A combined CFD modeling and experimental study of pyrolytic carbon deposition, Diam. Relat. Mater. 70 (2016) 173–178. https://doi.org/10.1016/j.diamond.2016.10.010.

[94] S. Abanades, H. Kimura, H. Otsuka, Kinetic investigation of carbon-catalyzed methane decomposition in a thermogravimetric solar reactor, Int. J. Hydrogen Energy 40 (2015) 10744–10755. https://doi.org/10.1016/j.ijhydene.2015.07.023.

[95] Y.S. Han, J.Y. Lee, Improvement on the electrochemical characteristics of graphite anodes by coating of the pyrolytic carbon using tumbling chemical vapor deposition, Electrochim. Acta 48 (2003) 1073–1079. https://doi.org/10.1016/S0013-4686(02)00845-9.

[96] C. Wang, Y. Liu, Q. You, F. Ye, L. Cheng, Effect of the pyrolytic carbon (PyC) content on the dielectric and electromagnetic interference shielding properties of layered SiC/PyC porous ceramics, Ceram. Int. 45 (2019) 5637–5647. https://doi.org/10.1016/j.ceramint.2018.12.028.

[97] J.-F. Després, A. Oberlin, Microscopy Studies of Deposition of Pyrolytic Carbon on Polished Substrates, Tanso 1996 (1996) 2–12. https://doi.org/10.7209/tanso.1996.2.

[98] T. Kreuger, W.P.M. van Swaaij, A.N.R. Bos, S.R.A. Kersten, Methane decomposition

kinetics on unfunctionalized alumina surfaces, Chem. Eng. J. 427 (2022) 130412. https://doi.org/10.1016/j.cej.2021.130412.

[99] W. Albeiro, H. Sierra, Synthesis and characterization of graphene related nanomaterials by catalytic decomposition of methane using transition metal catalysts, (2019).

[100] T. Jawhari, A. Roid, J. Casado, Raman spectroscopic characterization of some commercially available carbon black materials, Carbon N. Y. 33 (1995) 1561–1565. https://doi.org/10.1016/0008-6223(95)00117-V.

[101] Y. Quan, Q. Liu, S. Zhang, S. Zhang, Comparison of the morphology, chemical composition and microstructure of cryptocrystalline graphite and carbon black, Appl. Surf. Sci. 445 (2018) 335–341. https://doi.org/10.1016/j.apsusc.2018.03.182.

[102] O. Feron, F. Langlais, R. Naslain, J. Thebault, On kinetic and microstructural transitions in the CVD of pyrocarbon from propane, Carbon N. Y. 37 (1999) 1343–1353. https://doi.org/10.1016/S0008-6223(98)00329-7.

[103] X. Zeng, D. Fu, H. Sheng, S. Xie, X. Li, Q. Hu, J. Zou, Growth and morphology of carbon nanostructures by microwave-assisted pyrolysis of methane, Phys. E Low-Dimensional Syst. Nanostructures 42 (2010) 2103–2108. https://doi.org/10.1016/j.physe.2010.04.002.

[104] P. Cuesta, A Dhamelincourt, J.M.D. Laureyns, J Martinez-Alonso, A and Tascon, RAMAN MICROPROBE STUDIES ON CARBON MATERIALS, Carbon N. Y. 32 (1994) 1523–1532.

[105] R. Hareesh, E. Vetrivendan, R. Sole, S. Ningshen, Surface characterization and influence of pyrolysis temperature on microstructure, phase and oxidation kinetics of CVD pyrolytic graphite coatings, Appl. Surf. Sci. 529 (2020) 147106. https://doi.org/10.1016/j.apsusc.2020.147106.

[106] P. Mallet-Ladeira, P. Puech, C. Toulouse, M. Cazayous, N. Ratel-Ramond, P. Weisbecker, G.L. Vignoles, M. Monthioux, A Raman study to obtain crystallite size of carbon materials: A better alternative to the Tuinstra-Koenig law, Carbon N. Y. 80 (2014) 629–639. https://doi.org/10.1016/j.carbon.2014.09.006.

[107] D.S. Zhang, K.Z. Li, H.J. Li, L.J. Guo, J.H. Lu, The influence of deposition temperature on the microstructure of isotropic pyrocarbon obtained by hot-wall chemical vapor deposition,

J. Mater. Sci. 46 (2011) 3632–3638. https://doi.org/10.1007/s10853-011-5279-0.

[108] P. Swain, M. Viji, P.S.V. Mocherla, C. Sudakar, Carbon coating on the current collector and LiFePO4 nanoparticles - Influence of sp2 and sp3-like disordered carbon on the electrochemical properties, J. Power Sources 293 (2015) 613–625. https://doi.org/10.1016/j.jpowsour.2015.05.110.

[109] Y. Peng, N. Pan, D. Wang, J. Yang, Z. Guo, W. Yuan, A Si–O–Si bridge assembled from 3-mercaptopropyltrimethoxysilane and silicon carbide for effective charge transfer in photocatalysis, J. Mater. Sci. 53 (2018) 12432–12440. https://doi.org/10.1007/s10853-018-2518-7.

[110] L.B. Biedermann, M.L. Bolen, M.A. Capano, D. Zemlyanov, R.G. Reifenberger, Insights into few-layer epitaxial graphene growth on 4H-SiC (000 1̄) substrates from STM studies, Phys. Rev. B - Condens. Matter Mater. Phys. 79 (2009) 1–10. https://doi.org/10.1103/PhysRevB.79.125411.

[111] A.O. Oni, K. Anaya, T. Giwa, G. Di Lullo, A. Kumar, Comparative assessment of blue hydrogen from steam methane reforming, autothermal reforming, and natural gas decomposition technologies for natural gas-producing regions, Energy Convers. Manag. 254 (2022) 115245. https://doi.org/10.1016/j.enconman.2022.115245.

[112] S.R. Patlolla, K. Katsu, A. Sharafian, K. Wei, O.E. Herrera, W. Mérida, A review of methane pyrolysis technologies for hydrogen production, Renew. Sustain. Energy Rev. 181 (2023). https://doi.org/10.1016/j.rser.2023.113323.

[113] A.I. Hussain, J. Shabanian, M. Latifi, J. Chaouki, Hydrogen Production from Methane Thermal Pyrolysis in a Microwave Heating-Assisted Fluidized Bed Reactor, Energy and Fuels 38 (2024) 21617–21632. https://doi.org/10.1021/acs.energyfuels.4c03428.

[114] V. L'hospital, L.G. de Araujo, E. Landrivon, A. Mello, M. Radoiu, V. Trillaud, J.F. Meunier, Y. Schuurman, N. Guilhaume, D. Farrusseng, Methane pyrolysis into hydrogen and solid carbon: A comparative analysis of conventional and microwave heating approaches, Catal. Today 459 (2025) 115430. https://doi.org/10.1016/j.cattod.2025.115430.

[115] M. Schwaab, J.C. Pinto, Optimum reference temperature for reparameterization of the Arrhenius equation. Part 1: Problems involving one kinetic constant, Chem. Eng. Sci. 62

(2007) 2750–2764. https://doi.org/10.1016/j.ces.2007.02.020.

[116] G. Patrianakos, M. Kostoglou, A. Konstandopoulos, One-dimensional model of solar thermal reactors for the co-production of hydrogen and carbon black from methane decomposition, Int. J. Hydrogen Energy 36 (2011) 189–202. https://doi.org/10.1016/j.ijhydene.2010.09.061.

[117] M. Wullenkord, Determination of Kinetic Parameters of the Thermal Dissociation of Methane, 2011.

[118] M. Mokashi, A. Bhimrao Shirsath, P. Lott, H. Müller, S. Tischer, L. Maier, O. Deutschmann, Understanding of gas-phase methane pyrolysis towards hydrogen and solid carbon with detailed kinetic simulations and experiments, Chem. Eng. J. 479 (2024) 147556. https://doi.org/10.1016/j.cej.2023.147556.

[119] J.K. Dahl, V.H. Barocas, D.E. Clough, A.W. Weimer, Intrinsic kinetics for rapid decomposition of methane in an aerosol flow reactor, Int. J. Hydrogen Energy 27 (2002) 377–386. https://doi.org/10.1016/S0360-3199(01)00140-9.

[120] T. Keipi, T. Li, T. Løvås, H. Tolvanen, J. Konttinen, Methane thermal decomposition in regenerative heat exchanger reactor: Experimental and modeling study, Energy 135 (2017) 823–832. https://doi.org/10.1016/j.energy.2017.06.176.

[121] L.J.J. Catalan, E. Rezaei, Coupled hydrodynamic and kinetic model of liquid metal bubble reactor for hydrogen production by noncatalytic thermal decomposition of methane, Int. J. Hydrogen Energy 45 (2020) 2486–2503. https://doi.org/10.1016/j.ijhydene.2019.11.143.

[122] S. Rodat, S. Abanades, J. Coulié, G. Flamant, Kinetic modelling of methane decomposition in a tubular solar reactor, Chem. Eng. J. 146 (2009) 120–127. https://doi.org/10.1016/j.cej.2008.09.008.

[123] D.H. Napier, N. Subrahmanyam, Pyrolysis of Methane in a Single Pulse Shock Tube, J. Appl. Chem. Biotechnol. 22 (1972) 303–317.

[124] X. Bai, S. Tiwari, B. Robinson, C. Killmer, L. Li, J. Hu, Microwave catalytic synthesis of ammonia from methane and nitrogen, Catal. Sci. Technol. 8 (2018) 6302–6305. https://doi.org/10.1039/c8cy01355a.

[125] M. Stein, Y.L. Ding, J.P.K. Seville, D.J. Parker, Solids motion in bubbling gas fluidized beds, Chem. Eng. Sci. 55 (2000) 5291–5300. https://doi.org/10.1016/S0009-2509(00)00177-9.

[126] J. Shabanian, J. Chaouki, Hydrodynamics of a gas-solid fluidized bed with thermally induced interparticle forces, Chem. Eng. J. 259 (2015) 135–152. https://doi.org/10.1016/j.cej.2014.07.117.

[127] A.G. Whittaker, D.M.P. Mingos, Synthetic reactions using metal powders under microwave irradiation, J. Chem. Soc. Dalt. Trans. (2002) 3967–3970. https://doi.org/10.1039/b206557f.

[128] N. Haneishi, S. Tsubaki, E. Abe, M.M. Maitani, E. ichi Suzuki, S. Fujii, J. Fukushima, H. Takizawa, Y. Wada, Enhancement of Fixed-bed Flow Reactions under Microwave Irradiation by Local Heating at the Vicinal Contact Points of Catalyst Particles, Sci. Rep. 9 (2019) 1–12. https://doi.org/10.1038/s41598-018-35988-y.

[129] Y. Badran, R. Ansart, J. Chaouki, O. Simonin, Macro-scale numerical investigation of the contribution of Van der Waals force to the pressure-drop overshoot in fine-particle fluidized beds, Powder Technol. 436 (2024) 119505. https://doi.org/10.1016/j.powtec.2024.119505.

[130] Q.F. Hou, Z.Y. Zhou, A.B. Yu, Micromechanical modeling and analysis of different flow regimes in gas fluidization, Chem. Eng. Sci. 84 (2012) 449–468. https://doi.org/10.1016/j.ces.2012.08.051.

[131] H. Cui, J. Chaouki, Ä.P. De Montre, A Comparison of Two- and Single-Phase Models for Fluidized-Bed Reactors, Ind. Eng. Chem. Res. 40 (2001) 5526–5532.

[132] K. Adavi, J. Shabanian, J. Chaouki, Temperature Distribution Assessment in Gas-Solid Reactive and Nonreactive Systems Heated by Microwaves, Ind. Eng. Chem. Res. 62 (2023) 9970–9982. https://doi.org/10.1021/acs.iecr.3c00575.

[133] K. Adavi, A.C. Garcia, J. Shabanian, M. Latifi, J. Chaouki, Kinetic study of microwave heating-assisted chemical looping ammonia synthesis over Mn-Fe-Ba-based nitrogen carrier, Fuel 401 (2025) 135874. https://doi.org/10.1016/j.fuel.2025.135874.

[134] M. Khodabandehloo, J. Shabanian, J.P. Harvey, J. Chaouki, Kinetic study of microwave heating-assisted chemical looping dry reforming of methane over magnetite, Int. J. Hydrogen Energy 96 (2024) 1079–1086. https://doi.org/10.1016/j.ijhydene.2024.11.358.

[135] A.L. Moghaddam, S. Hejazi, M. Fattahi, M.G. Kibria, M.J. Thomson, R. AlEisa, M.A. Khan, Methane pyrolysis for hydrogen production: navigating the path to a net zero future, Energy Environ. Sci. 18 (2025) 2747–2790. https://doi.org/10.1039/d4ee06191h.

[136] C. Jiang, I.W. Wang, X. Bai, S. Balyan, B. Robinson, J. Hu, W. Li, A. Deibel, X. Liu, F. Li, L.M. Neal, J. Dou, Y. Jiang, R. Dagle, J.A. Lopez-Ruiz, G. Skoptsov, Methane Catalytic Pyrolysis by Microwave and Thermal Heating over Carbon Nanotube-Supported Catalysts: Productivity, Kinetics, and Energy Efficiency, Ind. Eng. Chem. Res. 61 (2022) 5080–5092. https://doi.org/10.1021/acs.iecr.1c05082.

[137] M. Reza, G.J. Nathan, M. Jafarian, Process configurations to lower the temperature of methane pyrolysis in a molten metal bath for hydrogen production, Int. J. Hydrogen Energy 48 (2023) 39805–39822. https://doi.org/10.1016/j.ijhydene.2023.08.186.

[138] S.G. Nnabuife, C.K. Darko, P.C. Obiako, B. Kuang, X. Sun, K. Jenkins, A Comparative Analysis of Different Hydrogen Production Methods and Their Environmental Impact, Clean Technol. 5 (2023) 1344–1380. https://doi.org/10.3390/cleantechnol5040067.

[139] J. Yang, J. Shadbahr, C.D. Teguia, M. Akbari, M. Benali, LIFE CYCLE ASSESSMENT OF HYDROGEN PRODUCTION PATHWAYS IN CANADA, 2022.

[140] L. Fulcheri, E. Dames, V. Rohani, C. Pierre, R.C. Daunesse, S.A. Cedex, Plasma-based conversion of methane into hydrogen and carbon black, Curr. Opin. Green Sustain. Chem. 50 (2024) 100973. https://doi.org/10.1016/j.cogsc.2024.100973.

[141] P. Peng, P. Chen, C. Schiappacasse, N. Zhou, E. Anderson, D. Chen, J. Liu, Y. Cheng, R. Hatzenbeller, M. Addy, Y. Zhang, Y. Liu, R. Ruan, A review on the non-thermal plasma-assisted ammonia synthesis technologies, J. Clean. Prod. 177 (2018) 597–609. https://doi.org/10.1016/j.jclepro.2017.12.229.

[142] J. Wang, M. Wen, X. La, J. Ren, J. Jiang, D.C.W. Tsang, Resonance-driven microwave heating for improved methane conversion to hydrogen, Appl. Energy 375 (2024) 124100. https://doi.org/10.1016/j.apenergy.2024.124100.

[143] P.T. Luckie, Staged solid-solid separations revisited, Int. J. Miner. Process. 72 (2003) 455–462. https://doi.org/10.1016/S0301-7516(03)00119-4.

[144] Z.J. Hu, K.J. Hüttinger, Mechanisms of carbon deposition - A kinetic approach, Carbon N.

Y. 40 (2002) 624–628. https://doi.org/10.1016/S0008-6223(01)00316-5.

[145] C. Hu, H. Li, S. Zhang, W. Li, N. Li, Chemical vapor infiltration of pyrocarbon from methane pyrolysis: kinetic modeling with texture formation, Sci. China Mater. 62 (2019) 840–852. https://doi.org/10.1007/s40843-018-9379-7.

[146] M.S. Galtsov-Tsientsiala, A.O. Dudoladov, A. V. Grigorenko, M.S. Vlaskin, Study of Soot Deposits during Continuous Methane Pyrolysis in a Corundum Tube, Appl. Sci. 13 (2023). https://doi.org/10.3390/app131910817.

[147] T. Kim, J. Lee, K.H. Lee, Microwave heating of carbon-based solid materials, Carbon Lett. 15 (2014) 15–24. https://doi.org/10.5714/CL.2014.15.1.015.

[148] G. Zhong, S. Xu, C. Chen, D.J. Kline, M. Giroux, Y. Pei, M. Jiao, D. Liu, R. Mi, H. Xie, B. Yang, C. Wang, M.R. Zachariah, L. Hu, Synthesis of Metal Oxide Nanoparticles by Rapid, High-Temperature 3D Microwave Heating, Adv. Funct. Mater. 29 (2019) 1–9. https://doi.org/10.1002/adfm.201904282.

[149] S.W. Churchill, H.H.S. Chu, Correlating equations for laminar and turbulent free convection from a vertical plate, Int. J. Heat Mass Transf. 18 (1975) 1323–1329. https://doi.org/10.1016/0017-9310(75)90243-4.

[150] J.P. Holman, Heat transfer, 10th ed., McGraw-Hill, New York, 2010.

[151] F.P. Incropera, D.P. DeWitt, T.L. Bergman, A.S. Lavine, Fundamentals of Heat and Mass Transfer, 6th ed., Wiley, Hoboken, NJ, 2006. https://doi.org/10.1016/j.applthermaleng.2011.03.022.

[152] I. Soleimani, N. Elahipanah, J. Shabanian, J. Chaouki, In-situ quantification of the magnitude of interparticle forces and its temperature variation in a gas-solid fluidized bed, Chem. Eng. Sci. 232 (2021) 116349. https://doi.org/10.1016/j.ces.2020.116349.

APPENDIX A Supporting information to chapter 4

A.1 Supporting figures and tables

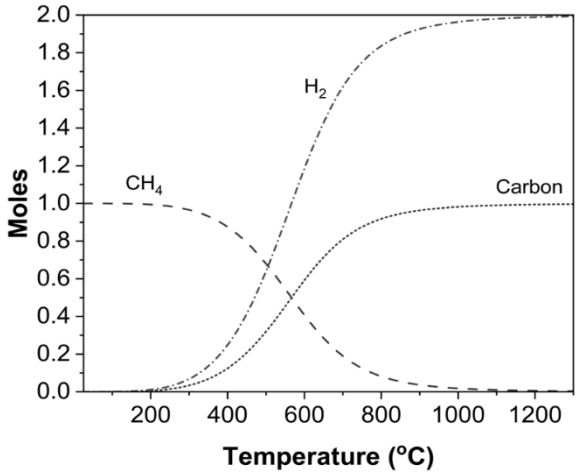

Figure A.1 Equilibrium diagram for 1 mole of CH4 calculated by Gibbs energy minimization module in FactSage 7.2 at a total pressure of 1 atm and the temperature range of 25–1300 °C showing CH_4, H_2, and solid carbon.

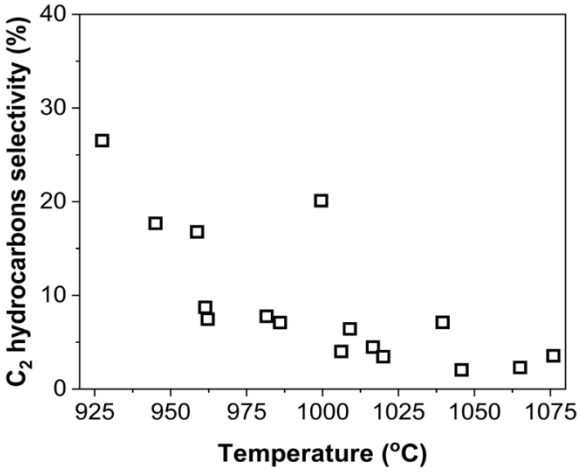

Figure A.2 Variation in C_2 hydrocarbons selectivity with temperatures in MW-FBR.

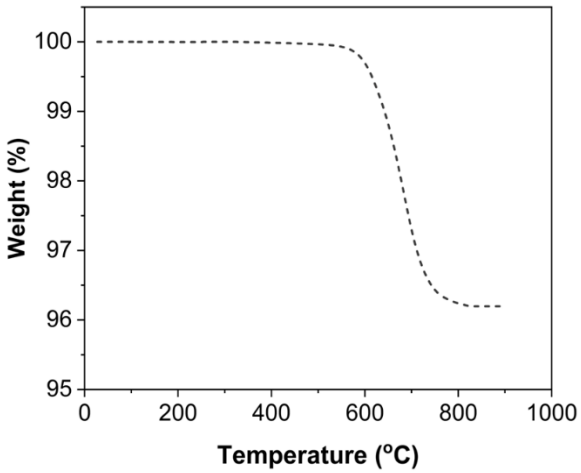

Figure A.3 Representative TGA analysis of C-SiC sample.

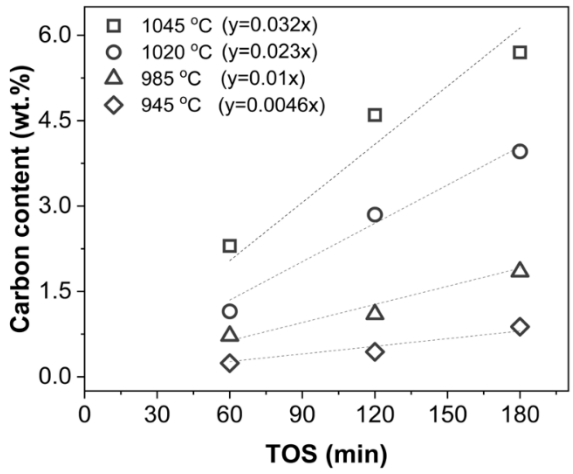

Figure A.4 Representative net carbon gain variation with TOS at different temperatures and 4 cm/s in MW-FBR.

Table A.1 Summary of carbon deposition experiments

Heating method	Temperature (°C)	Gas velocity (cm/s)	TOS (min)	CH_4 inlet molar fraction	Carbon acc. (wt. %)	$r_p(\times 10^{-4})$, (g_C/g_S min)	$r_d(\times 10^{-4})$, (g_C/g_S min)	r_d/r_p (%)	H-atom balance (%)
MW	945	4	180	0.50	0.9	0.6	0.5	80±5	100.3±0.4
	985	4	180	0.50	1.9	1.3	1.0	79±5	99.6±0.2
	1020	4	180	0.50	3.9	2.7	2.3	85±6	101.7±0.3
	1045	4	180	0.50	5.7	3.9	3.2	81±7	99.1±0.3
	1017	6	180	0.50	3.2	2.3	1.9	82±6	100.2±0.5
	1009	12	180	0.50	3.1	2.9	1.8	61±10	99.3±0.3
	985	4	180	0.35	1.5	1.0	0.9	88±8	100.1 ±0.4
	988	4	180	0.20	0.8	0.5	0.46	89±5	99.5±0.4
Conventional	950	4	270	0.50	0.5	0.3	0.2	55±7	97.7±0.4
	1000	4	180	0.50	0.7	0.8	0.4	52±6	98.8±0.3
	1050	4	180	0.50	1.4	1.9	0.7	38±7	98.7±0.4
	1050	6	180	0.50	1.6	2.1	0.9	42±5	98.3±0.4
	1050	12	180	0.50	1.3	2.2	0.8	35±9	98.3±0.5
	1050	4	180	0.30	0.8	1.1	0.4	39±3	99.0±0.4
	1050	4	270	0.20	0.7	0.6	0.3	48±3	99.5±0.6

$$H_{atom}\ balance = \frac{2n_{H_2} + \sum y \times n_{C_xH_y}}{4n_{CH_{4_o}}} \times 100 \qquad (A.1)$$

Where y and x are the number of H atoms and the number of carbon atoms, respectively, in a gas specie. Standard error of the mean (SEM) was estimated from 12 GC data points for each experiment:

$$SEM = \frac{\sqrt{\sum_{i=1}^{n}(x_i - \bar{x})^2 \,/_{n-1}}}{\sqrt{n}}$$

Overall, the individual H-atom mass balance ranged from 96% to 102%.

Table A.2 Elements identification and quantification from the XPS Survey scan

Name	B.E.	Atomic %	
		SiC	MW-1050
Si 2p	101.9	33.0	0.3
C 1S	284.4	42.2	97.0
O 1s	533.3	22.7	2.7

Table A.3 Elements identification, quantification and peak fitting parameters from a high-resolution XPS scan

Name	ID	B.E.	Atomic (%)		Area ratio		L/G mix (%)[a]		FWHM (eV)	
			SiC	MW-1050	SiC	MW-1050	SiC	MW-1050	SiC	MW-1050
Si 2p	Si-C	100.4	24.1	--	1	--	35	--	1.4	--
	O-Si-C	101.3	6.6	0.1	0.44	1	35	35	1.7	1.8
	SiO2	103.0	3.2	--	0.16		35		1.7	--
C1s	Si-C	282.5	21.4	--	1		38.4		1.2	--
	O-Si-C	283.1	4.5	--	0.21		38.4		1.2	--
	C sp2	284.2	--	87.5	--	1	--	29.9	--	0.9
	C-C sp3	285.0	14.6	2.6	0.68	0.03	38.4	29.9	1.6	1.6
	C-O	286.7	1.8	--	0.08		38.4		1.6	--
	O-C=O	289.0	1.3	1.3	0.06	0.02	38.4	29.9	1.6	1.6
	C1s shake-up of C sp2	290.4	--	5.7	--	0.07	--	29.9	--	2.9
O1s	Fe-O	531.0	2.4	0.2	0.16	0.2	70	55.2	1.7	1.8
	C=O	531.5	1.5	1.2	0.1	1	70	55.2	1.7	1.8
	Si-O	532.3	15.0	0.2	1	0.14	70	55.2	1.7	1.8
	C-O	533.1	3.6	1.2	0.24	1	70	55.2	1.7	1.8

[a] Lorentzian-Gaussian mix

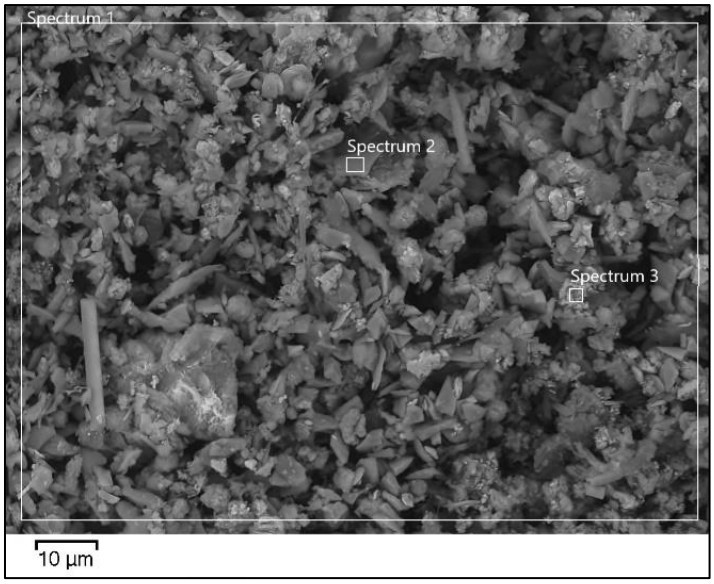

Figure A.5 Sample retrieved from the gas filter in MW-FBR.

Table A.4 Spectrum analysis of EDX data according to Figure A.5 acquisition

Composition (%)	Spectrum number		
	1	2	3
C	82.7	64.8	100.0
Si	17.3	35.2	0.0

A.2 Carbon Deposition on reactors walls

In conventional heating, carbon deposited on the reactor wall in the form of sheets, which were mechanically removed and collected for analysis, Figure A.6. Two types of carbon were distinguished based on the deposition location: the dense bed at high temperature (Figure A.6a-d) and the freeboard at a relatively lower temperature (Figure A.6e and f).

Carbon deposited on the wall in the dense bed is a result of a combination of heterogenous catalytic and non-catalytic reactions. Gas species underwent chemisorption on the inner surface of the reactor, leading to the formation of carbonaceous depositions via a catalytic heterogeneous mechanism. The reactor was constructed of Inconel, an alloy comprising Fe and Cr metals. Carbon atoms diffused and migrated within the metal lattice, inducing structural stress in the metal structure. This stress ultimately resulted in the extraction of metal crystallites from the surface. As carbon deposition progressed, a network of dense carbon filaments emerged. These carbon filaments were 2 μm in width, 0.6 μm in thickness, and tens of micrometers in length, Figure A.6c and d. Over time, the catalytic activity of the wall diminished, and the carbon filaments acted as the sites for carbon deposition via a heterogeneous non-catalytic mechanism which resulted in further filament growth. Figure A.6c and d show the side of the recovered carbon sheets facing the gas stream were carbon filaments. The EDX scan showed this structure is formed of pure carbon. On the other hand, the side of the recovered carbon sheets facing the inner wall showed the presence of Cr and Fe extracted from the reactor wall, Figure A.6b. TGA results of carbon deposited in the dense bed zone had a remaining of 16 wt.% after carbon oxidation, Figure A.7. The remaining weight corresponded to the extracted metals present in the sample.

In the freeboard, the carbon deposited in sheets that were easily removed, Figure A.6e and f. There was no difference between the two sides of the sheets (facing the wall or the gas stream). EDX showed that it consisted of carbon only and it was metal-free. Complete oxidation of this carbon was achieved in TGA, Figure A.7. This carbon formed from agglomerates of soot particles formed in the gas phase according to $CH_4 \rightarrow C_2 \rightarrow C_6 \rightarrow PAH \rightarrow soot$ [146].

Carbon deposition on the quartz reactor under MW heating was much less as compared visually to conventional heating. Figure A.8 shows a photo of MW-FBR reactor wall after 23 hrs time on stream and SEM-EDX analysis.

a)

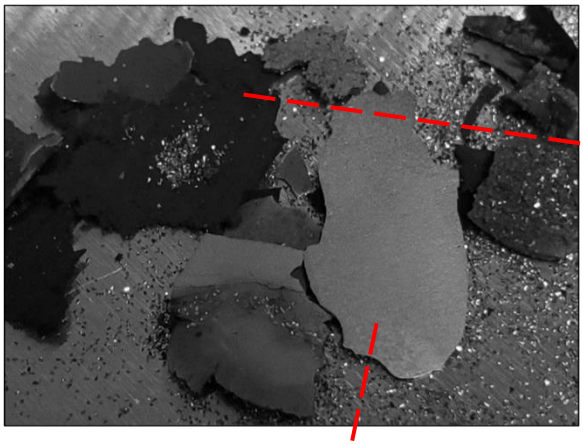

b)

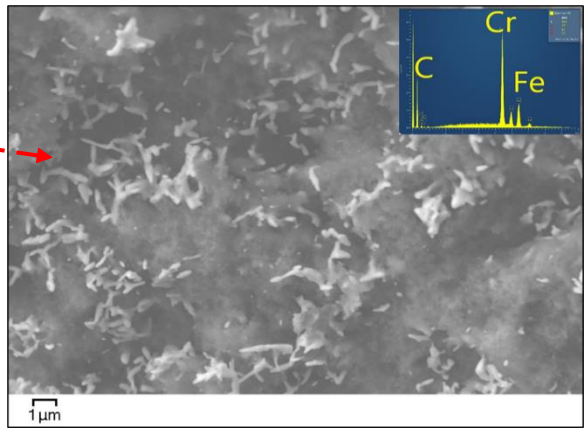

c)

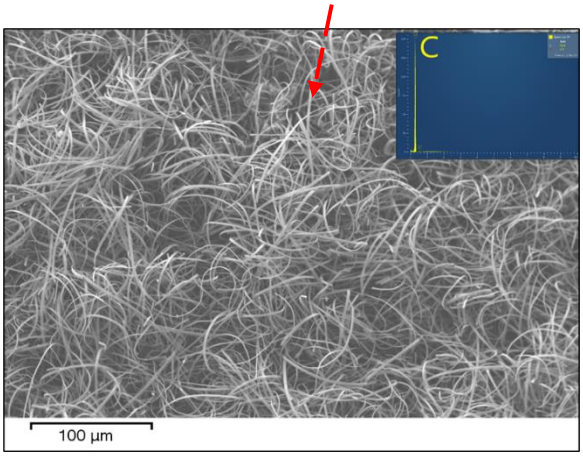

d)

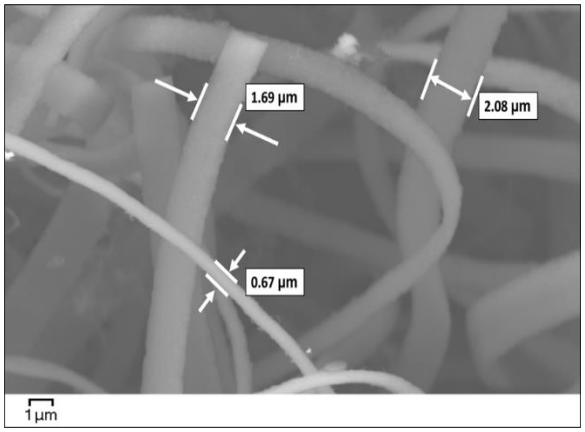

e)

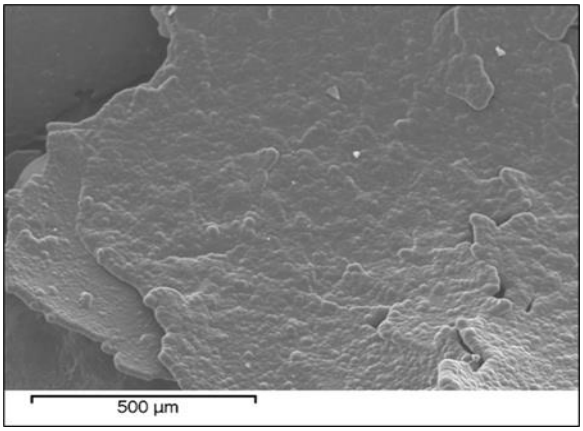

f)

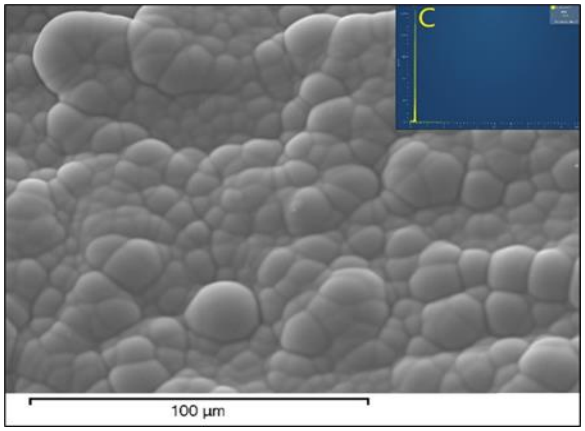

Figure A.6 Carbon restored from CH-FBR wall showing a) photo of carbon sheets from the dense bed; and SEM-EDX of b) carbon retrieved from the dense bed facing the wall; c) and d) carbon from dense bed facing the dense bed at different magnifications; e) and f) carbon from the freeboard wall at different magnifications.

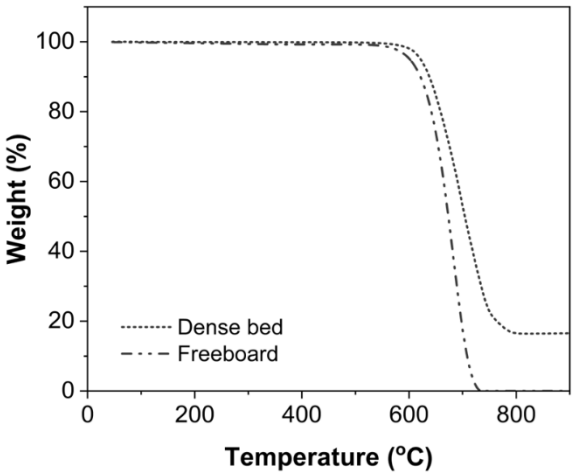

Figure A.7 TGA of carbon restored from CH-FBR wall.

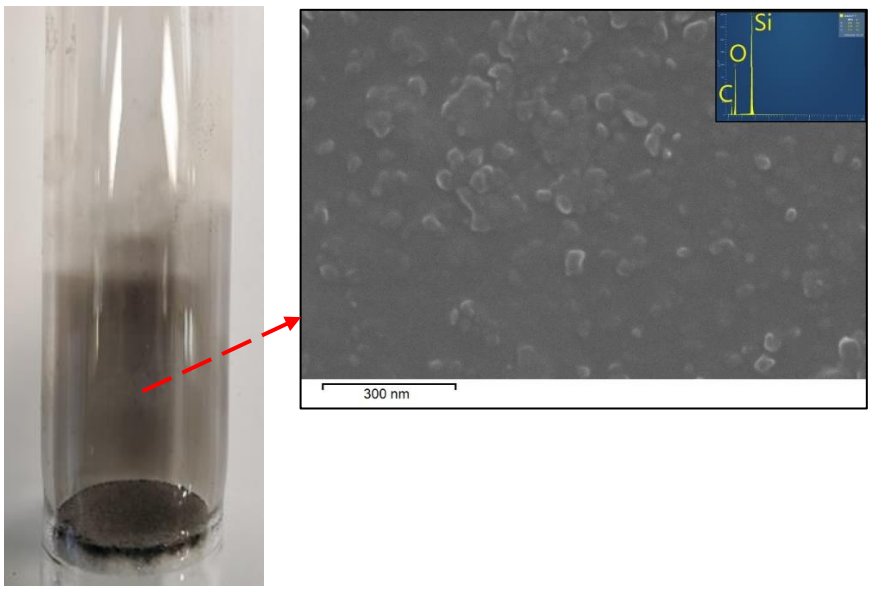

Figure A.8 SEM-EDX performed on a piece of the reactor wall from MW-FBR after 23 hr TOS. The carbon layer deposited on the wall was thin and could not be mechanically collected for analysis. Therefore, the SEM was performed on a piece of the reactor comprising the the inner wall of the reactor. EDX result shows the surface consists of Si at 42 At.%, O at 33 At.%, and C at 25 At.%. The signal from Si and O belongs to quartz observed due to the thin layer of carbon.

A.3 Dielectric properties and electrical conductivity measurement, and effect of carbon loading on temperature

The ability of a material to be heated by MW radiation is characterized by its electromagnetic properties. Dielectric constant (ε') indicates how much of the incident MW energy is absorbed by the material. Dielectric loss factor (ε'') determines how much of the absorbed MW energy dissipates in the form of thermal energy. The quality of a material to be heated by MW radiation is defined by its dielectric loss tangent ($\tan\delta=\varepsilon''/\varepsilon'$). Higher values for the dielectric loss tangent are desirable. The electrical conductivity (σ) of the material also plays a role in MW heating. The heating mechanisms for solids under MW radiation are described by interfacial polarization and Joule heating [147,148].

Figure A.9 and Table A.5 show the electrical conductivity and dielectric properties versus carbon loading. Dielectric constant and electrical conductivity increased with increasing carbon loading. Figure A.10 shows the effect of carbon deposition on the temperature. The increase in the electrical conductivity and the dielectric properties impacted the heating rate and the maximum temperature obtained from MW heating of the solid particles. The maximum temperature of SiC particles is 390 ºC. While for C-SiC with carbon content of 0.7 wt.% and 4.0 wt.%, the maximum temperature is 830 ºC and 1070 ºC, respectively.

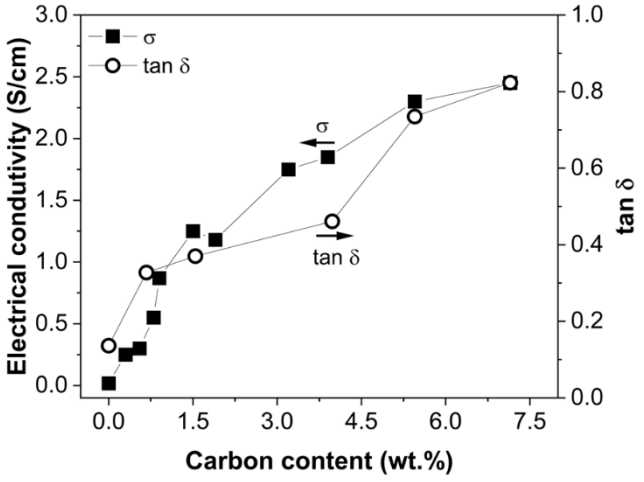

Figure A.9 Effect of carbon content on electrical conductivity (σ) and loss tangent (tan δ) (at 2.45 GHz and 20 ºC).

Table A.5 Dielectric properties of solid particles

Carbon content (wt.%)	ε'	ε''	tan δ	σ (S/cm)
0.0	8.4	1.1	0.14	0.02
0.7	22.7	7.4	0.33	0.6
1.5	46.4	17.2	0.37	1.25
3.9	67.1	30.9	0.46	1.85
5.4	75.7	55.6	0.73	2.3
7.1	80.1	65.9	0.82	2.45

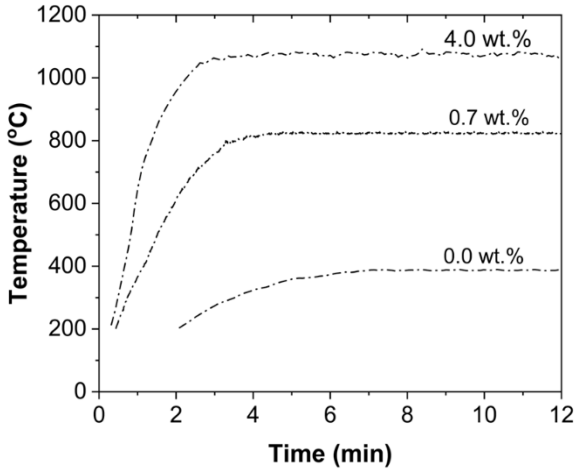

Figure A.10 Effect of carbon content on particles heating rate and maximum temperature for SiC (0.0 wt.%) and C-SiC with carbon content of 0.7 wt.% and 4.0 wt.%.

A.4 MW-FBR power consumption

The MW power consumed (dissipated within the solid particles) in MW-FBR was estimated by energy balance. At steady state, neglecting kinetic and potential energy with N_2 as the fluidizing gas, the overall energy balance on the reactor yields:

$$Q_{MW} + Q_{in} = Q_{out} + Q_{loss} \tag{A.2}$$

Substituting for the terms in Eq. (A.2):

$$Q_{mw} = \varepsilon_m \sigma_{SB} \, (2A_t + A_w) \, (T_s^4 - T_0^4) + \dot{m}_g C_{p_g} \left(T_{g_{in}} - T_g\right) + hA_w(T_w - T_0) \tag{A.3}$$

The convection heat transfer coefficient (h) was estimated by the correlation of Churchill and Chu [149,150]:

$$Nu = 0.68 + \frac{0.67 R_a^{\frac{1}{4}}}{\left[1 + \left(\frac{0.492}{pr}\right)^{\frac{9}{16}}\right]^{\frac{4}{9}}} \tag{A.4}$$

Where:

$$Ra = GrPr \tag{A.5}$$

$$Gr = \frac{g\beta(T_w - T_0)L^3}{\nu^2} \tag{A.6}$$

$$\beta = 1/T_f \tag{A.7}$$

$$T_f = \frac{T_w + T_0}{2} \tag{A.8}$$

$$h = \frac{Nu \, k_g}{L} \tag{A.9}$$

Properties in free convection heat transfer coefficient are evaluated for air at the film temperature from [151].

Nomenclature

Acronym

C-SiC	Carbon-coated silicon carbide
CH-FBR	Conventional heating-assisted fluidized bed reactor
MW	MW
MW-1050	C-SiC produced in MW-FBR at 1050 ºC
MW-FBR	MW heating-assisted fluidized bed reactor
Q_{in}	Heat coming to the reactor by gas convection (W)
Q_{loss}	Heat losses to the environment by radiation and natural free convection at reactor wall (W)
Q_{MW}	MW power consumed in the dense bed (W)
Q_{out}	Heat leaving the reactor by gas convection (W)

Symbols

A_t	Reactor cross sectional area (m^2)
A_w	Reactor wall area (m^2)
C_{p_g}	Specific heat capacity of the gas (J/kg K)
g	Gravitational acceleration (m/s^2)
Gr	Grashof number (-)
h	Convective heat transfer coefficient (W/m^2 K)

k_g	Gas thermal conductivity (W/m K)
L	Dense bed height (m)
$\dot{m}_g$	Gas inlet mass flow rate (kg/s)
Nu	Mean Nusselt number
n_i	Outlet molar flow rate of gas specie i (mol/min)
$n_{i,o}$	Inlet molar flow rate of gas specie i (mol/min)
n_T	Total molar flow rate of the outlet gas stream (mol/min)
Pr	Prandtl number (-)
Ra	Rayleigh number (-)
T_0	Ambient temperature (K)
T_f	Film temperature (K)
T_g	Gas temperature measured by thermocouple (K)
$T_{g_{in}}$	Inlet gas temperature (298.15 K)
T_w	Wall temperature (K)
tan(δ)	Dielectric loss tangent (-)

Greek letters

β	Thermal coefficient of expansion (1/K)
ε'	Dielectric constant (-)
ε''	Dielectric loss factor (-)

ε_m	Emissivity of solid particles = 0.84
ν	Kinematic viscosity (m^2/s)
σ_{SB}	Stefan-Boltzmann constant$= 5.67 \times 10^{-8}\ W/m^2K^4$

APPENDIX B Supporting information to chapter 5

B.1 Mole balance in MW-FBR and CH-FBR

Based on the local temperature distribution around hot particles in MW-FBR, we represented CH_4 conversion as occurring in three zones: the bulk gas at T_g, the thermal boundary layer at $T_{bl}(r)$, and the near-surface region at T_s. For a single-step decomposition of CH_4, the one-dimensional mole balance on the CH_4 yields:

$$n_{CH_4}\big|_z - n_{CH_4}\big|_{z+\Delta z} - \left(r_{CH_4,g}\Delta V_g + r_{CH_4,bl}\Delta V_{bl} + r''_{CH_4,s}\Delta A_s\right) = 0 \qquad (B.1)$$

We modeled the reaction occurring at the near particle surface based on the surface area of particles per unit reactor volume given by:

$$\Delta A_s = \frac{6A_t(1-\varepsilon)}{d_p}\Delta z \qquad (B.2)$$

The thermal boundary layer was approximated as a thin shell surrounding each particle. The differential volume occupied by the thermal boundary layer:

$$\Delta V_{bl} = \frac{A_t(1-\varepsilon)\Delta z}{\frac{1}{6}\pi d_p^3}\left[\frac{4}{3}\pi\left(\left(\frac{d_p}{2}+\delta_T\right)^3 - (\frac{d_p}{2})^3\right)\right] \qquad (B.3)$$

The differential volume occupied by the bulk gas is given by:

$$\Delta V_g = A_t\ \varepsilon_g\ \Delta z \qquad (B.4)$$

ε is the total volume fraction of the gas in the fluidized bed and we estimated the voidage of the bulk gas (ε_g) by:

$$\varepsilon_g = \varepsilon - \varepsilon_{bl} \qquad (B.5)$$

Where:

$$\varepsilon_{bl} = (1-\varepsilon)\frac{\left(\frac{d_p}{2}+\delta_T\right)^3 - (\frac{d_p}{2})^3}{(\frac{d_p}{2})^3} \qquad (B.6)$$

Substituting the expressions of ΔA_s, ΔV_{bl}, ΔV_g, and ε_{bl} in Eq. (B.1) and dividing by $A_t\Delta z$ and taking the limit of $\Delta z \to 0$, the gradient conversion of CH_4 across the reactor length:

$$\frac{dx_{CH_4}}{dz} = \frac{1}{u_g}\left(\frac{1-x_{CH_4}}{1+\varepsilon_v x_{CH_4}}\right)\left[k_g\varepsilon_g + k_{bl}(1-\varepsilon)\frac{\left(\frac{d_p}{2}+\delta_T\right)^3 - (\frac{d_p}{2})^3}{(\frac{d_p}{2})^3} + k_s''\frac{6(1-\varepsilon)}{d_p}\right] \quad (B.7)$$

For CH-FBR where the gas and solid are at equal temperature, Eq. (B.1) is reduced to:

$$n_{CH_4}\big|_z - n_{CH_4}\big|_{z+\Delta z} - \left(r_{CH_4}\Delta V\right) = 0 \quad (B.8)$$

Which yields:

$$\frac{dx_{CH_4}}{dz} = \frac{k\,\varepsilon}{u_{\mathrm{g}}}\left(\frac{1-x_{CH_4}}{1+\varepsilon_v x_{CH_4}}\right) \quad (B.9)$$

B.2 Temperature measurement in CH-FBR

The axial temperature profile in CH-FBR is shown in Figure B.1, and was fitted using a 4th-order polynomial. The corresponding fitting parameters for each processing temperature are listed in Table B.1. The temperature in the axial position is measured at six different points, three points in the dense bed and three points in the freeboard.

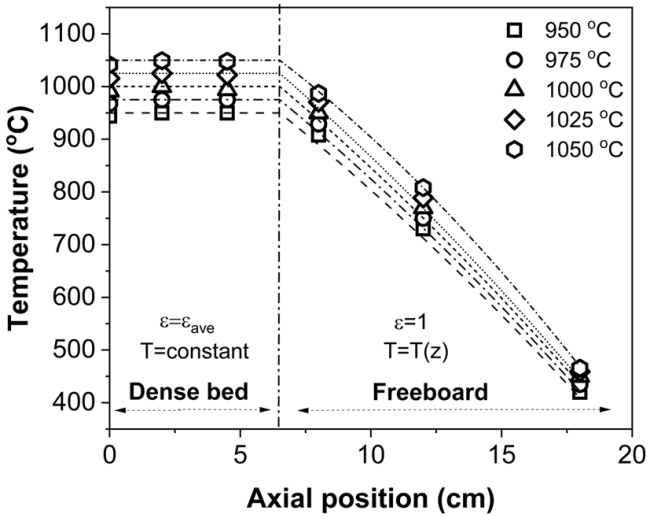

Figure B.1 Temperature measurement in the dense bed and the freeboard in CH-FBR

Table B.1 Fitting parameters for axial temperature distribution in CH-FBR in Eq. (5.19)

Temperature (°C)	Fitting parameter				
	a	b	c	d	e
950	0.02	-0.76	4.95	-8.42	946
975	0.02	-0.71	4.42	-6.86	970
1000	0.02	-0.66	3.90	-5.30	993
1025	0.02	-0.62	3.36	-3.65	1017
1050	0.02	-0.57	2.82	-1.99	1041

B.3 Numerical simulation

We employed COMSOL Multiphysics (6.3) software to numerically investigate microscale hotspots MW-FBR, which are challenging to measure experimentally. The computational domain consisted of a multimode MW cavity (386×351×249 mm) connected to a rectangular waveguide measuring 78×50×18 mm, Figure B.2a. We modeled geometries representing an isolated single particle and a pair of particles in contact, each 100 μm in diameter, Figure B.2b. Additionally, to validate the cavity solution, we simulated a packed bed (0.06 m height, 0.025 m diameter) with a bed voidage equivalent to the average voidage in MW-FBR, Figure B.2c. Modeling MW-heated fluidized beds involves complexities due to simultaneous electromagnetic interactions, particle dynamics, and fluid flow. We employed a simplified modeling approach based on a packed bed with voidage equivalent to the average voidage of MW-FBR. This approach enabled the estimation of the temperature profile within the MW-heated fluidized bed operating across various regimes, including bubbling, turbulent, and fast fluidization. This approach enabled estimation of the temperature profile within the MW-heated fluidized bed operating across various regimes, including bubbling, turbulent, and fast fluidization. Adavi et. al. demonstrated that simulating MW-heated fluidized beds as packed beds with equivalent voidage effectively represents different fluidization regimes [132]. They have shown that this approach captures MW penetration depth, power dissipation distribution, and bed-scale temperature profiles in MW-heated fluidized beds [132]. However, this approach does not resolve microscale temperature gradients at the individual particle level, but it is suitable for predicting average bed temperature. The properties of the MW absorbent particles (SiC) employed in the simulation are listed in Table B.2. In developing the simulation model, we assumed that the properties of SiC particles, including permeability, permittivity, heat capacity, thermal conductivity, and density, were temperature independent. Additionally, we neglected magnetic losses within the SiC particles.

a)

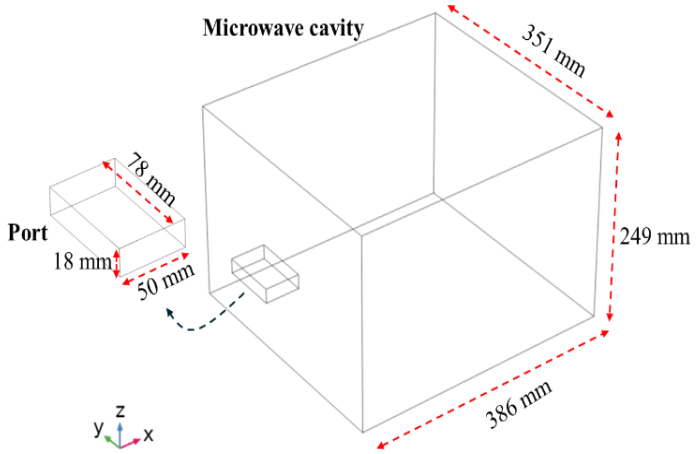

b)

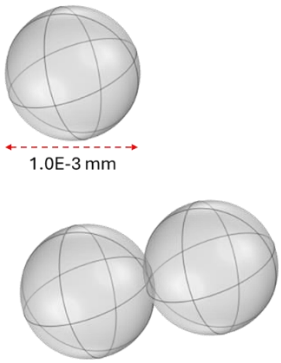

c)

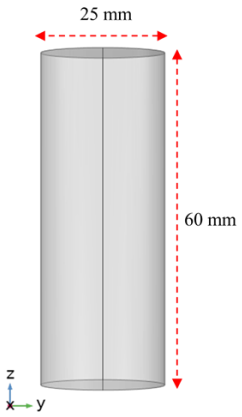

Figure B.2 Temperature measurement in the dense bed and the freeboard in CH-FBR

Table B.2 Properties of SiC particles in MW heating numerical simulation

Property	**Value**
SiC permittivity $\varepsilon_{r,s}$	80-66j
SiC permeability $\mu_{r,s}$	1
SiC electrical conductivity σ, (S/cm)	24.5
Density ρ_p, (g/cm^3)	3.2
Heat capacity C_p, (J/kg K)	690
Thermal conductivity k, (W/m K)	40

B.3.1 Governing equations

We initially solved Maxwell's equations to determine the electromagnetic field distribution within the MW cavity. Subsequently, we solved energy balance equations to calculate the temperature profiles of the particles and the packed bed.

B.3.1.1 Electromagnetic field distribution (Maxwell's Equations)

We solved Maxwell's equation in the following form

$$\nabla \times \mu_r^{-1}(\nabla \times E) - \left(\frac{c}{\omega}\right)^2 \left(\varepsilon_{r,eff} - \frac{j\sigma_{eff}}{\omega\varepsilon_o}\right) E = 0 \qquad (B.10)$$

Here, effective parameters $\varepsilon_{r,eff}$ and σ_{eff} represent the properties of the gas-solid bed, and we expressed them as follows:

$$\sigma_{eff} = \varepsilon\sigma_{N_2} + (1-\varepsilon)\sigma_s \qquad (B.11)$$

$$\varepsilon_{r,eff} = \varepsilon\varepsilon_{r,N_2} + (1-\varepsilon)\varepsilon_{r,S} \qquad (B.12)$$

We calculated MW power dissipation (Q_{mw}) according to Eq.(S.13) below:

$$Q_{mw} = 0.5\sigma_{eff}|E|^2 + \pi f \varepsilon_o \varepsilon''_{r,eff}|E|^2 \quad (B.13)$$

B.3.1.2 Energy Conservation

We solved the energy conservation equation coupled with Maxwell's equations to determine the local distribution within the particles. The energy equation for particles is expressed as follows:

$$\rho C_p \frac{\partial T}{\partial t} + \nabla.(-k_p \nabla T) = Q_{mw} \quad (B.14)$$

For the packed bed system, we considered an additional volumetric heat loss term (Q_g) due to gas-solid heat exchange:

$$\rho C_p \frac{\partial T}{\partial t} + \nabla.(-k_p \nabla T) = Q_{mw} - Q_g \quad (B.15)$$

We treated the fluidized bed as a porous medium, where gas flows uniformly through the bed, absorbing heat from the particles, thus cooling the bed. Consequently, we quantified Q_g using the Eq. (B.16) below:

$$Q_g = \dot{m}_g C_{p_g}(T_{out} - T_{in})/V \quad (B.16)$$

We applied impedance boundary conditions at the MW cavity boundaries to represent electromagnetic interactions at the metal surface. We included heat losses to the environment via radiation and natural convection from the outer reactor wall.

B.3.2. Grid analysis

We conducted a grid independence analysis by testing different numbers of mesh elements to ensure a mesh-independent solution. The MW cavity was meshed with at least ten elements per wavelength (approximately 0.12 m), whereas the simulated geometries were meshed with a minimum element size of 10^{-9} m. We employed free tetrahedral elements for meshing all domains. To evaluate mesh sensitivity, we calculated the average volumetric power absorption density for various mesh sizes, as illustrated in Figure B.3. A mesh consisting of 225,767 cells with an average element quality of 0.6577 was sufficient to achieve a mesh-independent solution.

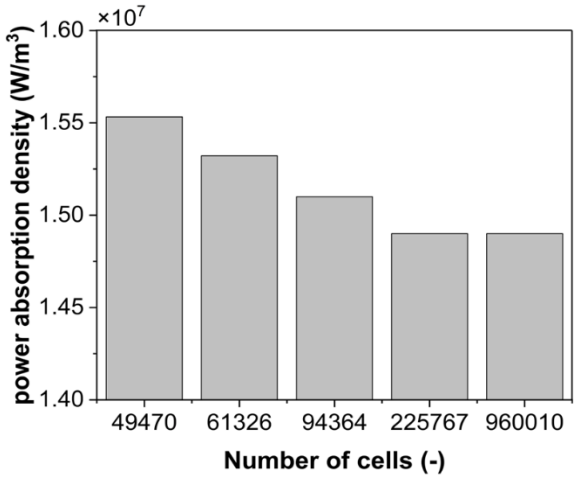

Figure B.3 Mesh independence evaluation

B.3.3 Model validation

We validated the cavity solution of our numerical model using experimental results from the MW-FBR system. Figure B.4 compares experimentally measured temperatures with predicted surface-average temperature and volume-average temperature from the model. The simulation prediction closely matches the experimental readings, with the initial heating rate being 11.2 °C/s in the simulation compared to 10.5 °C/s measured experimentally. The experimentally measured steady state surface temperature was 1065 °C, which falls between the simulated surface-average temperature of 1053 °C and the volume-average temperature of 1100 °C, Figure B.4.

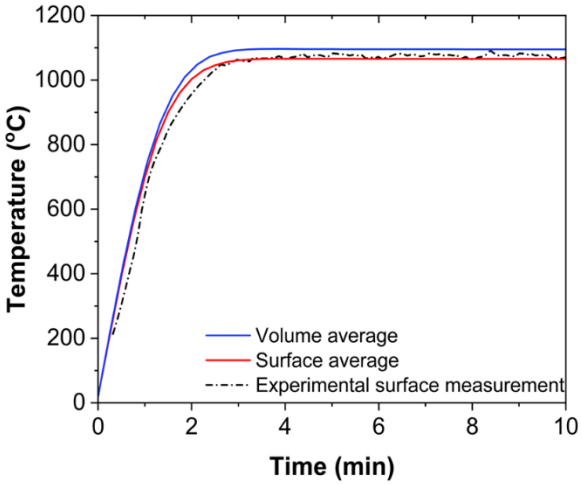

Figure B.4 Comparison of experimental and simulated temperature profiles for model validation

B.4 Measurement of minimum fluidization voidage

We measured the minimum fluidization voidage in a 0.0525 m internal diameter stainless steel fluidized bed. The unit is equipped with calibrated flow controllers and two differential pressure transducers for measurement of the total bed pressure drop and partial in-bed pressure drop. More details about the setup can be found in [152]. We used Nitrogen as a fluidizing gas. We estimated the minimum fluidization velocity (u_{mf}) based on the total pressure drop in the decreasing velocity pass. We identified u_{mf} as the superficial gas velocity (u_g) at which the pressure drop curve for the fixed bed region intersects with the nearly constant pressure drop of the fully fluidized regime. We calculated the bed voidage by Eq. (B.17):

$$\varepsilon = 1 - \frac{m_s/\rho_p}{\frac{\pi}{4} D_t^2 H} \qquad (B.17)$$

We plotted ε profile against u_g and considered ε_{mf} as the bed voidage at u_{mf} in the decreasing velocity pass. Figure B.5 shows the variation in bed pressure drop and bed voidage at various u_g and the estimation of u_{mf} and ε_{mf} for three runs. The runs yielded a u_{mf} of 3.82 cm/s, 4.03 cm/s, and 4.13 cm/s, and an ε_{mf} of 0.473, 0.484, and 0.491 for an average value of 0.48 ± 0.008.

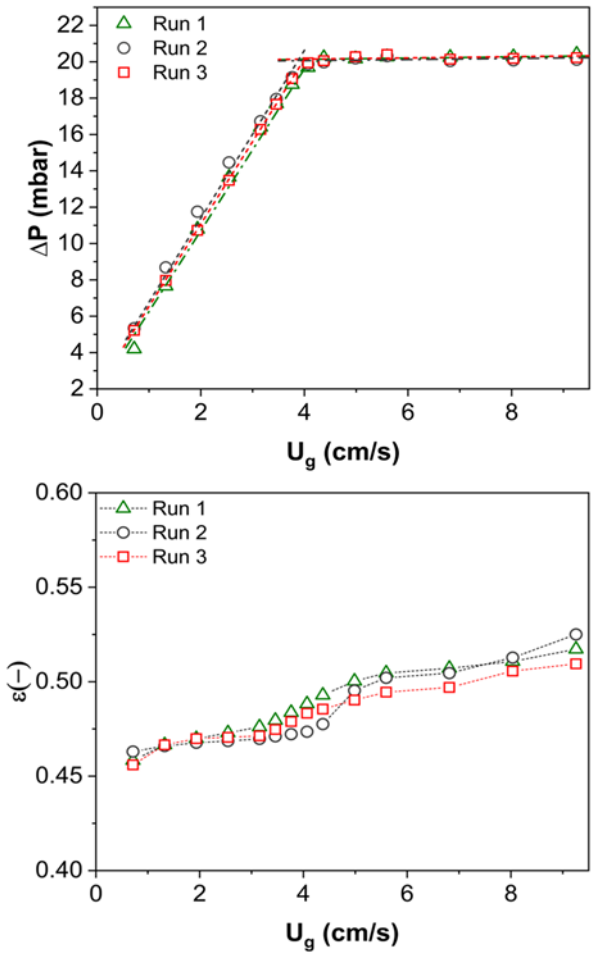

Figure B.5 Bed pressure drop and voidage profiles at different superficial gas velocities

Nomenclature

Acronym

CH-FBR	Conventional heating-assisted fluidized bed reactor
MW	MW
MW-FBR	MW heating-assisted fluidized bed reactor

Symbols

A_t	Reactor cross-sectional area (m^2)

A_s	Reactor cross-sectional area (m^2)
C_{p_p}	Particle heat capacity (J/kg K)
C_{p_g}	Gas heat capacity (J/kg K)
d_p	Particle size (m)
E	Electrical field (V/m)
H	Dense bed height (m)
h	Gas heat transfer coefficient (W/m^2 K)
k	Rate constant for CH_4 decomposition (1/s)
k_{bl}	Rate constant for CH_4 decomposition in the thermal boundary layer (1/s)
k_g	Rate constant for CH_4 decomposition in the gas phase (1/s)
k_o	Pre-exponential factor for CH_4 decomposition (1/s)
k_p	Thermal conductivity of particles (W/m K)
k_s''	Rate constant for CH_4 decomposition near the solid surface (m/s)
k_f	Gas thermal conductivity (W/m K)
Nu	Nusselt number (-)
n_i	Outlet molar flow rate of gas specie i (mol/s)
$n_{i,o}$	Inlet molar flow rate of gas specie i (mol/s)
m_s	Mass of solid particles (kg)
Q_{mw}	MW power dissipation (W/m^3)

r_{CH_4}	CH_4 reaction rate (mol/s)
u_{mf}	Minimum fluidization velocity (m/s)
u_g	Superficial gas velocity (m/s)
v_0	Inlet volumetric flow rate (m^3/s)
V_g	Gas volume (m^3)
V_{bl}	Thermal boundary layer volume (m^3)
x_{CH_4}	Methane conversion (%)

Greek letters

α_{hs}	Surface fraction of hotspot area (-)
β	Thermal correction factor (-)
δ_T	Thickness of thermal boundary layer (m)
ε	Bed average voidage (-)
ε_v	Volumetric expansion factor (-)
ε_g	Gas volume fraction (-)
ε_{mf}	Minimum fluidization voidage (-)
ε_{bl}	Thermal boundary layer volume fraction (-)
ε_r	Relative permittivity (-)
ε_o	Permittivity in vacuum
ε''	Dielectric loss factor (-)

μ	Gas Viscosity (Pa.s)
μ_r	Relative permeability (-)
ρ_p	Particle density (kg/m^3)
ρ_g	Gas density (kg/m^3)
σ	Electrical conductivity (S/cm)